Ultimate Strength of Wind Turbine Blades under Multiaxial Loading

Haselbach, Philipp Ulrich

Publication date:
2015

Document Version
Publisher's PDF, also known as Version of record

Ultimate Strength of Wind Turbine Blades under Multiaxial Loading

Philipp Ulrich Haselbach

PhD Thesis

DTU Wind Energy
Technical University of Denmark
November 2015

DTU Wind Energy
Department of Wind Energy

Title: Ultimate Strength of Wind Turbine Blades under Multiaxial Loading
Author: Philipp Ulrich Haselbach
Department: DTU Wind Energy

The thesis was submitted to the Technical University of Denmark in partial fulfilment of the requirements for the PhD degree from the PhD School DTU Wind Energy.

The PhD project was carried out in the years 2012-2015 at the Wind Turbine Structures section of DTU Wind Energy, the Department of Wind Energy. The dissertation was submitted on the 30th of November 2015 and successfully defended on the 16th of February 2016.

Main Supervisor:
Kim Branner
Co-supervisor:
Robert David Bitsche
Christian Berggreen

Examiners:
Lars Pilgaard Mikkelsen, DTU Wind Energy
Esben Lindgaard, Aalborg University
Rogier P.L. Nijssen, Knowledge Centre WMC

DTU Wind Energy PhD-0064 (EN)
ISBN: 978-87-93278-92-9
November 2015

Project Period:
2012-2015

Degree:
PhD

Sponsorship: Danish Centre for Composite Structures and Materials for Wind Turbines (DCCSM), grant no. 09-067212 from the Danish Strategic Research Council. The financial support is greatly appreciated.

Technical University of Denmark
Department of Wind Energy
Frederiksborgvej 399
Building 118
4000 Roskilde
Denmark
Telephone: +45 50156403
Email: phih@dtu.dk
www.vindenergi.dtu.dk

Abstract

Modern wind turbine rotor blades are sophisticated lightweight structures, optimised towards achieving the best compromise between aerodynamic and structural design as well as cost efficient manufacturing. They are usually designed for a lifetime of minimum 20 years, where they must endure a variety of weather conditions including uncontrollable, extreme winds without developing damage and fracture.

The trend in the development of wind turbines is towards larger, more efficient wind turbines, placed offshore, where access is difficult and repairs costly. In consequence, failures in the rotor blade usually lead to long downtimes. Therefore, it is of great importance that the turbines operate reliably and that robust methods are available to predict damage initiation and growth under multiaxial loading conditions.

The purpose of this PhD project is the investigation of multiaxial loading effects and its influence on the ultimate strength of typical wind turbine rotor blade structures and to develop methods to perform reliable prediction of failure. For this purpose, origin and consequence of some of the typically occurring failure types in wind turbine rotor blades are investigated. The research aims on predicting more accurately when and how blades fail under complex loading. The main contribution from this PhD study towards more reliable and robust operating wind turbine systems can be divided into two fields. One part covers numerical modelling approaches and the other part deals with failure origin and effects.

The research, covering the numerical part, is done with the purpose to investigate the limitation of state-of-the-art numerical prediction methods and to improve existing simulation methods by combining different existing techniques, capable to predict the ultimate strength of wind turbine rotor blades under multiaxial loadings. Failure origin and effects are studied numerically and ex-

perimentally with the purpose to investigate root causes of blade failure and to find generalities for their origin.

The main contributions from this PhD study covering the numerical part are the demonstration of a subset simulation approach for large scale delamination in the cap of a wind turbine rotor blade, making it possible to determine more precisely critical delamination sizes and load levels for delamination growth onset and propagation in dependency of the through thickness location. Another modelling approach shows a modelling strategy, where shell and solid elements were combined with the purpose to estimate the strain energy release rate of transversely orientated crack in the trailing edge for different loading conditions. Furthermore, state-of-the-art failure criteria are studied and their limitations demonstrated by comparing numerical and experimental results of a full scale blade loaded to ultimate failure.

The main contributions from this PhD thesis dealing with failure origin and effects are the determination of generalities of failure. For buckling driven delaminations, delamination onset and propagation could be determined. For trailing-edge failure, a characterisation of effects of geometrical non-linear cross section deformation and trailing-edge wave formation on the energy release rate was shown. Furthermore, a sequence of trailing edge buckling leading to sandwich failure and finally causing ultimate blade failure were demonstrated.

Resumé

Nutidens vindmøllevinger er avancerede letvægtskonstruktioner, som er optimeret ift. aerodynamik og strukturelt design såvel som omkostningseffektiv produktion. Levetiden for vindmøllevinger er minimum 20 år, hvor de skal kunne modstå forskelligartet vejr, herunder ekstreme vindforhold, uden at blive beskadiget.

Trenden inden for udviklingen af vindmøller fokuserer på større og mere effektive vindmøller, som placeres off-shore. Her vil de ikke være lettilgængelige, hvorfor reparationer vil være særligt omkostningsfulde. Hvis der opstår problemer med vingerne på vindmøllerne vil det som konsekvens af at vindmøllerne ikke er lettilgængelige betyde at disse vil være ude af drift i længere tid. Derfor er det specielt vigtigt for disse vindmøller at driften er stabil og uden indgreb og at der findes pålidelige metoder til at forudsige begyndende beskadigelse samt forværring af eksisterende skader ved høj belastning.

Formålet med dette PhD-projekt er at undersøge effekten af multiaksial belastning og dennes indflydelse på den samlede styrke for de mest almindelige konstruktioner af vindmøllevinger samt at udvikle metoder til at forudsige hvornår en skade opstår. Som baggrund for dette er der foretaget en undersøgelse af årsagerne og konsekvenserne af nogle af de mest typiske skader set ifm. vindmøllevinger. Det er målet med forskningen foretaget i dette projekt, at forbedre mulighederne for at forudsige mere præcist hvornår og hvordan der sker beskadigelse af vindmøllevinger ved høj belastning. Dette projekt bidrager ift. ovenstående inden for to områder; Anvendelse af numerisk modellering samt undersøgelse af årsagerne til beskadigelse samt effekter afledt af dette.

Forskningen omhandlende den numeriske modellering er udført med det formål at undersøge begrænsningen af de typisk anvendte metoder til at forudsige beskadigelse og for at udvikle forbedrede simuleringsmetoder, som kan forudsige den maksimale belastning af vindmøllevinger. Hvor skaderne opstår samt de

afledte effekter deraf er undersøgt numerisk og eksperimentelt med det formål at finde frem til de grundlæggende årsager til beskadigelse af vindmøllevinger samt for at forsøge at danne et billede af hvornår de opstår.

Dette PhD-projekt bidrager med ny viden i form af at vise at det er muligt at anvende en simuleringstilgang for at undersøge effekten af delamineringer i den bærende del af vindmølle vinger. Dermed bliver det muligt at bestemme den kritiske størrelse af delamineringer og belastningsniveauet hvorved delamineringer begynder at vokse afhængig af dens position i tykkelsen. En anden metode anvendt til modellering viser en strategi, hvor skal og solid elementer kombineres med det formål at estimere frigivelseshastigheden af tøjningsenergi for tværgående revner i bagkanten ved forskellige belastningssituationer. Derudover er de typisk anvendte svigtkriterier undersøgt og deres begrænsninger påvist ved at sammenligne numeriske beregninger og eksperimentelle resultater fra en vinge testet til svigt.

PhD-projektet bedrager derudover også med ny viden om hvorfor skader opstår og metoder til at bestemme effekten af disse. For bulingsdrevet delaminering kunne delamineringens start og vækst bestemmes. For bagkants svigt er effekten af geometriske ikke-lineære tværsnits deformationer og bølgedannelse i bagkanten bestemt for frigivelseshastigheden af tøjningsenergi. Endelig er det demonstreret hvordan bagkants buling førte til sandwich panel svigt og ultimativt til vingesvigt.

Preface

The thesis was submitted to the Technical University of Denmark in partial fulfilment of the requirements for obtaining the PhD degree at the Technical University of Denmark. The PhD project was carried out from May 2012 till November 2015 at the Wind Turbine Structures section of the Department of Wind Energy.

The PhD project has been supervised by Kim Branner, Robert David Bitsche and Christian Berggreen. The PhD project was founded by the Danish Centre for Composite Structures and Materials for Wind Turbines (DCCSM), grant no. 09-067212 from the Danish Strategic Research Council. The financial support is greatly appreciated.

The dissertation is organised as a collection of papers. The first part of the thesis gives an overview of the necessary background information. The second part contains a collection of four articles. Part I consists of Chapter 1 to 5. In Chapter 1 motivation and structural challenges of rotor blades covered within this PhD study are introduced. In Chapter 2 a brief introduction to the ultimate strength of composite materials and failure types is given. Chapter 3 describes the theory of fracture mechanics and continuum damage mechanics. Chapter 4 deals with failure types and fracture mechanics applied to wind turbine blade structures. In Chapter 5, the results of the research are summarised and a brief overview of future work is given. Part II consists of four publications (Papers A to D), which were written during this PhD study. The following publications are included:

- Paper A entitled *The effect of delaminations on local buckling in wind turbine blades*
- Paper B entitled *A comprehensive investigation of trailing edge damage in a wind turbine rotor blade*

- Paper C entitled *On initiation of trailing edge failure in full-scale wind turbine blade test*

- Paper D entitled *The effect of multiaxial loading on a wind turbine rotor blade*

During the PhD study, parts of the work were presented at the *Danish Center for Applied Mathematics and Mechanics* (DCAMM) 14^{th} Internal Symposium in Nyborg, Denmark in March 2013; the Proceedings of 9^{th} PhD Seminar on Wind Energy in Europe at the Uppsala University Campus Gotland, Sweden in September 2013; the 20^{th} *International Conference on Composite Materials* (ICCM20) in Copenhagen, Denmark in July 2015 and the *Danish Centre for Composite Structures and Materials for Wind Turbines* (DCCSM) Seminar in Middelfart, Denmark in September 2015.

From February to May 2015, I visited Dr. Rogier Nijssen at the independent research foundation *Knowledge Centre WMC* (Knowledge Centre Wind Turbine Materials and Constructions) in the Netherlands as part of the external stay.

Beside research activities, two 13-weeks Master courses ("Design of Lightweight Composite Structures" in 2013 and "Fiber Reinforced Lightweight Structures" in 2014) at DTU Lyngby were assisted and taught as teaching assistant during the PhD project.

Publications and conference contributions are listed below:

List of journal publications

- P. U. Haselbach, R. D. Bitsche and K. Branner, *The effect of delaminations on local buckling in wind turbine blades*, Renewable Energy (2016) pp. 295-305, DOI information: 10.1016/j.renene.2015.06.053

- P.U. Haselbach, M.A. Eder and F. Belloni, *A comprehensive investigation of trailing edge damage in a wind turbine rotor blade*, accepted for publication in Wind Energy on the 22^{nd} of November 2015

- P.U. Haselbach and K. Branner, *On initiation of trailing edge failure in full-scale wind turbine blade test*, submitted to Engineering Fracture Mechanics on the 28^{th} of October 2015

- P.U. Haselbach, P. Berring and T. Kim, *The effect of multiaxial loading on a wind turbine rotor blade*, preliminary draft - to be submitted.

List of presentations

- P. U. Haselbach, *Ultimate strength of wind turbine blade structures under multiaxial loading*, Danish Center for Applied Mathematics and Mechanics (DCAMM) 14^{th} Internal Symposium in Nyborg, Denmark in March 2013; poster presentation
- P.U. Haselbach, *Ultimate strength of wind turbine blade structures under multiaxial loading*, Proceedings of 9^{th} PhD Seminar on Wind Energy in Europe at the Uppsala University Campus Gotland, Sweden in September 2013; poster presentation
- P.U. Haselbach and K. Branner, *Effect of trailing edge damage on full-scale wind turbine blade failure*, 20^{th} International Conference on Composite Materials (ICCM20) in Copenhagen, Denmark in July 2015; oral presentation and article
- P.U. Haselbach, *Ultimate strength of wind turbine blade structures under multiaxial loading*, Danish Centre for Composite Structures and Materials for Wind Turbines (DCCSM) Seminar in Middelfart, Denmark in September 2015; oral presentation

A paid leave of seven months from the PhD project was taken to work on offshore projects within the DeepWind project at DTU Wind Energy. The work resulted in two publications which were presented at the 10^{th} Deep Sea Offshore Wind R&D Conference, DeepWind'2013 in Trondheim, Norway in February 2013 and at the 32*nd International Conference on Ocean, Offshore and Arctic Engineering*, OMAE2013, in Nantes, France in June 2013. The DeepWind'2013 conference contribution was published in the journal *Energy Procedia* with the title "Comparison of coupled and uncoupled load simulations on a jacket support structure" (P. U. Haselbach, A. Natarajan, R. G. Jivinangun and K. Branner). The article presented at the OMAE2013 is titled "Reliability assement of fatigue critical welded details in wind turbine jacket support structures" (K. Branner, H. S. Toft, P. U. Haselbach, A. Nataranjan and J. D. Sørensen).

Roskilde, 30-November-2015
Philipp Ulrich Haselbach

Acknowledgements

I would like to thank my supervisors Kim Branner, Robert David Bitsche and Christian Berggreen, who gave me the opportunity to carry out this PhD project at DTU Wind Energy. I am thankful for getting the chance to be part of this unique, dynamic and positive research environment at DTU Wind Energy, with a lot of highly skilled and friendly colleagues providing an excellent research atmosphere.

I am very grateful to Kim Branner, who introduced me to the research at DTU Risø and all his support over the years.

I would like to express my immense gratitude to Robert David Bitsche, who has always taken his time to discuss and share his great knowledge base and deep understanding of numerical mechanics with me. Whatever I was in doubt of or struggling with, Robert had answers like an encyclopaedia and explained me things patiently.

I would also like to express my deepest thanks to Martin Alexander Eder, who introduced me to conscientious, scientific work, with his passion for research and perfectionism. Martin has always showed great interest in my work, which led to several inspiring and fruitful discussions. I especially liked the challenging theoretical conversations on fracture mechanics. Thank you for your support!

Furthemore, I would like to thank my head of section Thomas Buhl, for his open mind, interest and strong support creating a joyful and productive working environment.

During my external stay at Knowledge Centre WMC in Holland I came in contact with many open-minded people, making this stay a great and unforgettable experience. Especially, I would like to thank Rogier P. L. Nijssen and Francisco Lahuerta for the smashing time in a nice atmosphere.

I have always enjoyed the great, inspiring and social atmosphere at DTU Wind Energy, with a lot of helpful and awesome colleagues. My special thanks go to my office mates Susana Rojas Labanda and Juan Felipe Gallego Calderon for enriching the working day by creating a lovely atmosphere throughout the entire PhD period.

I would like to thank my friends and commuting buddies Emmanuel Branlard, Ewan Machefaux, Niels Troldborg and Rogier Floor for always being there for me and making the commuting to a highlight of the day.

Many thanks also to my swimming mates from USG Svømning og Vandpolo allowing me to balance body and spirit during intense training sessions in a friendly ambience.

I would also like thank my friend Matthias Pieper for always being there with his sympathetic and humorous manner and deep going and reflecting conversations. Thank you!

Many thanks go to my parents and siblings for all the support throughout my entire life. Especially the support and engagement in a lovely environment from my parents during my childhood inspired my confidence, kindled my interests in technics and gave me the opportunity to get this awesome education.

Finally, I would like to express my sincere thanks to my girlfriend Stine for her support, patience, devotion and love.

Nomenclature

Lower case letters

a_i	Curve fitting constants
a	Length
a_0	Original crack length
a_c	Crack length
b	Element width
d	Internal damage variable
$d\Pi$	Difference in potential energy, overall potential
dA	Difference in area, fracture surface
dE	Difference in energy
d_f	Internal damage variable for fibre damage
d_m	Internal damage variable for matrix damage
d_s	Internal damage variable for in-plane shear damage
dx	Differential quotient
$f*$	Scalar within the Tsai-Wu failure criterion
f_d	Design material value
f_{ij}	Function of θ describing the stress field
g_{ij}	Function of θ describing the stress field
h_{ij}	Function of θ describing the stress field
k	Bond stiffness, stiffness
l_{cz}	Cohesive zone length
m	Number of buckle half wavelength (spanwise direction)
m	Metre(s)
min	Minute(s)
n	Number of buckle half wavelength (transverse direction)
r	Radius
t	Distance through the panel thickness

u_y	Displacement in y-direction
v	Wind speed
w_f	Fracture Energy
x, y, z	System axis
x_0	Distance in x-direction, gage length
z	Lengthwise position measured from the root
z_i	Lengthwise position measured from the root

Upper case letters

$[A]$	Extensional stiffness matrix
A	Area, rotor swept area
A_0	Initial area, starting point
$[B]$	Coupling stiffness matrix
C_d	Damage elasticity matrix
C_p	Maximum power coefficient
$[D]$	Bending stiffness matrix
D	Damage function
D_{ij}	Elements of the bending-stiffness matrix
E	Total energy
E_{11}	Longitudinal modulus
E_{22}	Transverse modulus
E_b	Bond energy
F	Force
F_d	Maximum design load
F_f^c	Hashin's criterion: Fibre compression
F_f^t	Hashin's criterion: Fibre tension
F_k	Characteristic value for the load
F_m^c	Hashin's criterion: Matrix compression
F_m^t	Hashin's criterion: Matrix tension
F_R	Resultant force vector
F_1	Nodal force in 1-direction
F_2	Nodal force in 2-direction
F_3	Nodal force in 3-direction
F_i	Tsai-Wu coefficient (with $i = 1, 2, 11, 22, 66, 12$)
G	Strain energy release rate
G_c	Critical strain energy release rate
G_I	Strain energy release rate for Modes I
G_{II}	Strain energy release rate for Modes II
G_{III}	Strain energy release rate for Modes III
G_{tot}	Total energy
G_{12}	Shear modulus
G_{ic}	Critical energy release rate

G_{Ic}	Critical energy release rate for Mode I
G_{IIc}	Critical energy release rate for Mode II
G_{IIIc}	Critical energy release rate for Mode III
GW	Giga Watt
I_F	Failure Index
J	Joule
K_i	Stress intensity factor
L_0	Initial length
L_e	Element length
M	Damage operator, parameter for the process zone calculation
M_R	Resultant moment
MW	Mega Watt
MWh	Mega Watt hours
Mx	Bending moment around the x-axis
My	Bending moment around the y-axis
Mz	Bending moment around the z-axis
N_0	Critical buckling load
N_e	Number of elements
Nm	Newton meter
P	Power
P_c	Cohesive force
QII	2^{nd} quadrant
R	Resistance function
S	Load function
S_l	Longitudinal shear strength
S_t	Transverse shear strength
T	Transformation matrix, panel thickness
U	Stored strain energy
W_s	Work required to form new surfaces
X	Stress component in x-direction
X_c	Longitudinal compressive strength
X_t	Longitudinal tensile strength
Y	Stress component in y-direction
Y_c	Transverse compressive strength
Y_c	Transverse tensile strength

Lower case Greek letters

α	Interaction coefficient
χ_{ij}	Function of θ describing the near tip displacement field
δ^0_{eq}	Initial equivalent displacement
δ_a	Element length
δ_{eq}	Equivalent damage displacement

δ_{eq}^{0}	Initial equivalent damage displacement
δ_{eq}^{f}	Equivalent damage displacement characterising complete material failure
δ_{eq}^{f}	Displacement at failure
δu_i	Relative nodal displacement (with $i = 1, 2, 3$)
ϵ	Strain
$\epsilon_{compressive}$	Allowable compressive strain
ϵ_{fibre}	Fibre strain
ϵ_{matrix}	Matrix strain
ϵ_{shear}	Allowable shear strain
$\epsilon_{tensile}$	Allowable tensile strain
η_i	Ratio factor, exponent
f_k	Characteristic material parameter
γ_f	Partial load safety factor
γ_m	Partial material safety factor
γ_m	Consequence of failure factor
λ	Distance, mode-mixity exponent, wave length
ν_{12}	Poisson's ratio
ν_{21}	Poisson's ratio
ϕ_{ij}	Function of θ describing the near tip displacement field
π	Pi, mathematical constant, π=3.14159...
ψ	Rotation angle, mode-mixity ratio
ψ_{ij}	Function of θ describing the near tip displacement field
ρ	Density
$\hat{\sigma}$	Effective stress tensor
σ	Stress tensor
σ_1	Stress component in 1-direction on lamina level
σ_2	Stress component in 2-direction on lamina level
σ_3	Stress component in 3-direction on lamina level
σ_c	Cohesive stress
$\sigma_{\|\|}^{c}$	Compressive stress in fibre direction
$\sigma_{\|\|}^{t}$	Tensile stress in fibre direction
$\sigma_{\perp}^{c}$	Compressive stress perpendicular to the fibre direction
$\sigma_{\perp}^{t}$	Tensile stress perpendicular to the fibre direction
σ_x	Stress component in x-direction
σ_y	Stress component in y-direction
σ_z	Stress component in z-direction
$\hat{\sigma}_{11}$	Component of the effective stress tensor
$\hat{\sigma}_{22}$	Component of the effective stress tensor
$\hat{\sigma}_{33}$	Component of the effective stress tensor
τ^0	Maximum interfacial strength/traction
τ_{ii}	Interfacial strength
$\tau_{\|\perp}$	Shear stress acting transverse to the fibre

	direction
τ_n	Interfacial strength longitudinal to the fibre
τ_n^0	Maximum interfacial strength longitudinal to the fibre
$\tau_{\perp\mid}$	Shear stress acting transverse to the fibre direction
$\tau_{\perp\perp}$	Shear stress acting transverse to the fibre direction
τ_s	Interfacial shear strength
τ_s^0	Maximum interfacial shear strength
τ_t	Interfacial transverse-shear strength
τ_t^0	Maximum interfacial transverse-shear strength
$\hat{\tau}_{12}$	Component of the effective stress tensor
$\hat{\tau}_{13}$	Component of the effective stress tensor
$\hat{\tau}_{23}$	Component of the effective stress tensor
θ	Transformation angle
θ_F	Angle of the resultant force vector
θ_M	Angle of the resultant moment
ψ	In-plane mode-mixity angle
ϕ	Out-of-plane mode-mixity angle

Upper case Greek letters

Δu_y	Displacement difference in y-direction
Δ	Separation
Γ	Fracture toughness
Λ	Wavelength
Π	Potential energy

Abbreviations

ABL	*Atmospheric Boundary Layer*
AC	*Aeroelastic Centre*
AIPS	*Automated Image Processing Software*
ALS	*Accidental Limit State*
ASM	*Linear cable position sensors of type "ASM Posiwire 6250"*
ASTM	*American Society for Testing and Materials*
BECAS	*Beam Cross Section Analysis Software*
BEM	*Blade Element Momentum*
BK criterion	*Benzeggagh-Kenane criterion*
Bladed	*Bladed wind turbine simulation tool*
C3D8I	*8-node linear brick elements in Abaqus*
CAE	*Computer-aided engineering*
CBM	*Constant Bending Moment*

CG	*Centre of gravity*
CDM	*Continuum Damage Mechanics*
CDS	*Crack Surface Displacement method*
CLT	*Classical Laminate Theory*
CO_2	*Carbon dixoide*
CoE	*Cost of Energy*
CZM	*Cohesive Zone Model*
DAMAGEMC	*Abaqus damage variable - Damage of Matrix under Compression*
DCAMM	*Danish Center for Applied Mathematics and Mechanics*
DCB	*Double Cantilever Beam*
DCCSM	*Danish Centre for Composite Structures and Materials for Wind Turbines*
DIC	*Digital Image Correlation*
DLC	*Design Load Case*
DOF	*Degrees of freedom*
DTU	*Technical University of Denmark*
DTU AED	*DTU Wind Energy - Section for Aeroelastic Design*
DTU KOM	*DTU Wind Energy - Section for Composite and Materials Mechanics*
DTU Nutech	*DTU Nutech - Center for Nuclear Technologies*
EC	*Elastic Centre - centre of elasticity*
EUDP	*Energy Technology Development and Demonstration Program*
FAST	*An aeroelastic tool for horizontal axis wind turbines*
FBG	*Fibre Bragg Grating*
FEA	*Finite Element Analysis*
FEM	*Finite Element Methods*
FF	*Fibre failure*
FLS	*Fatigue limit state*
FPF	*First-ply failure*
FPZ	*Fracture Process Zone*
GW	*Giga Watt*
HAWC2	*Horizontal Axis Wind turbine simulation Code 2nd generation*
HOLSIP	*HOListic Structural Integrity Process*
HRC	*High Resin Content*
ICCM20	20^{th} *International Conference on Composite Materials*
IFF	*Inter Fibre Failure*
ILS	*InterLaminar Stress*
ILSS	*InterLaminar Shear Stress*
LCOE	*Levelised Cost of Electricity*

LEFM	*Linear Elastic Fracture Mechanics*
LP	*Loading Point*
LPF	*Last-ply failure*
LP	*Load Point*
MDL	*Maximum Design Load*
MPa	Mega Pascal
NREL	*National Renewable Energy Laboratory*
Num	*Numerical result*
OMAE2013	32^{nd} *International Conference on Ocean, Offshore and Arctic Engineering*
PDA	*Progressive Damage Analysis*
Pre	*Pre-preg, preimpregnated fibres*
PSF	*Partial Safety Factor*
S8R	*8-node double curved thick shell elements with reduced integration*
SERR	*Strain Energy Release Rate*
SLS	*Serviceability limit state*
TSHR23	*Abaqus damage variable - transverse shear stress*
UL	*Ultimate Load*
ULS	*Ultimate limit state*
VARMT	*Vacuum Assisted Resin Transfer Moulding*
VCCT	*Virtual Crack Closure Technique*
VCE	*Virtual-Crack-Extension method*
WMC	*Knowledge Centre for Wind Turbine Materials and Constructions*
WWEA	*World Wind Energy Association*

Miscellaneous symbols

$\langle\rangle$	Macaulay brackets
$1D$	One dimensional
$2D$	Two dimensional
$3D$	Three dimensional
arctan	Arctan, trigonometric function of an angle
cos	Cosine, trigonometric function of an angle
\$	Currency: US-Dollar
∞	Infinity
$\parallel$	Longitudinal, in fibre direction
$\perp$	Transverse, perpendicular to the fibre direction
sin	Sine, trigonometric function of an angle

List of Figures

List of Tables

Contents

Part I

Background

Chapter 1

Introduction

1.1 Motivation

The strategy paper "Energy Strategy 2050", published by the Danish government in 2011, outlines Denmark's goal of becoming independent of coal, oil and gas by moving from fossil fuel to green energy [41]. A key role in the transition towards a CO_2-neutral energy sector is played by wind power. In 2013, the Danish wind power production accounted for 32.5 % of the Danish electricity supply [3] and this wind power share increased to 39 % in 2014 [24]. Denmark's position as world leader in domestic power supply based on wind power generated electricity was, by the end of September 2015, based on 5585 wind turbines with an installed capacity of 5029 MW according to the Danish Master Data Register of Wind Turbines [86]. While the number of wind turbines reduced from 6260 in 2000 to 5585 in 2015, the capacity of installed wind power increased from 2390 MW to 5029 MW. Turbines larger than 2 MW produced more than 60 % of the total energy from wind turbines. Offshore wind power – with its 516 wind turbines and a nominal capacity of 1271 MW – produced almost 40 % of the total wind power production in 2014 [3]. Not only in Denmark, but world-wide, wind power develops rapidly due to the rise in attention paid to the mitigation of climate change. According to the *World Wind Energy Association* (WWEA), a total capacity close to 370 GW was gathered with more than 50 GW newly installed in 2014 [12].

Figure 1.1 shows that there has been continuous development of larger and taller

wind turbines over the past decades. Together with this development in size, technological progress has led to a reduction of the *Levelised Cost of Electricity* (LCOE) (Figure 1.1), which is the sum of costs over lifetime divided by the sum of electricity produced over lifetime [85].

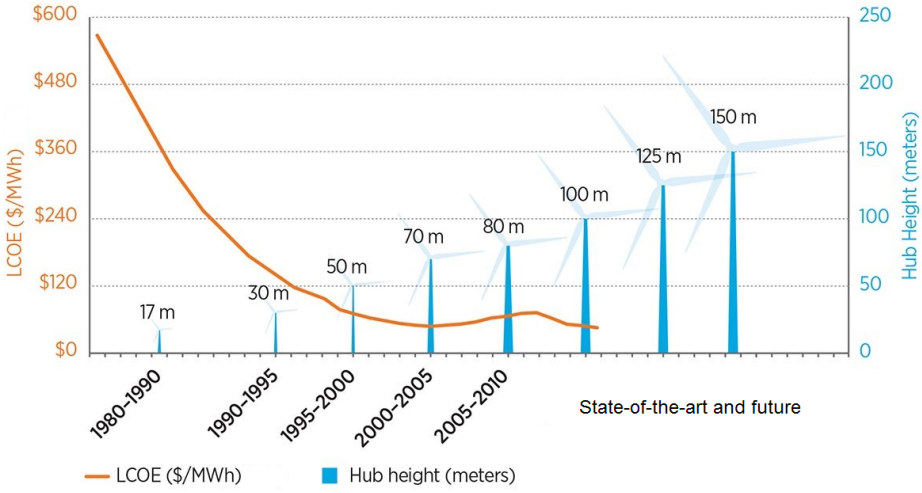

Figure 1.1: Wind turbine size development and decrease of the LCOE (taken from Office of Energy Efficiency & Renewable Energy [85]).

The theoretical power output (P) from a wind turbine is proportional to the third power of the wind speed (v) and proportional to the second power for the rotor radius (r) as shown in Equation 1.1, where $A = \pi r^2$ is the rotor swept area, C_p the maximum power coefficient with a theoretical maximum of 0.59 and the air density (ρ) [6]. Following the *Atmospheric Boundary Layer* (ABL) theory, the wind speed increases and becomes more constant with increasing height above the ground due to a decrease of aerodynamic drag/friction with the ground. An increase in rotor diameter and turbine height increases the power output. Simultaneous to the power increase, an increase in mass as well as higher loads comes with larger rotor blades, if the same or similar production methods and materials are used [94, 77]. Theoretically, scaling all three dimensions of an object leads to a cubic increase of mass. However, studies show that the mass of rotor blades (per meter of the rotor radius) only increases with a power of 2.2 to 2.5, depending on the innovation in design and construction of the rotor blade concept [37, 40].

$$P = \frac{1}{2}\rho A v^3 C_p \tag{1.1}$$

Modern wind turbine rotor blades are sophisticated lightweight structures, optimised towards achieving the best compromise between aerodynamic and structural design as well as cost efficient manufacturing. The aeroelastic design leads to complex, asymmetric rotor blade structures made of diverse composite structures in order to create structures with a high-strength-to-mass ratio. In favour of obtaining low *Cost of Energy* (CoE) and to become more competitive with other energy sources, wind turbine rotor blades became longer, slender and more flexible. Moreover, wind turbines are increasingly placed in wind parks, where interactions between adjacent turbines cause turbulent wind conditions, which can be structurally challenging [79]. While pushing the envelope for large wind turbine structures with ingenious rotor blade designs in correlation to complex wind conditions, rotor blades have shown increased failure rates the bigger and more advanced the wind turbines become [101].

Failures in the rotor blade usually lead to long downtimes and costly repairs. Whereas most of the aggregated downtime per turbine subsystem between 2003 to 2012 could be decreased, rotor blades stayed the same with a little variation in sequence [101]. Annually, 1 % to 3 % of the wind turbines require blade replacements with spikes in the first year and after 5 years [72]. This increases the CoE, especially when repair and maintenance have to be done on offshore sites, where blade replacement is approximately six times more costly than for onshore sites [1]. Blade replacements in the first two years of operation are usually the result of manufacturing defects or damages that occurred during transport and installation [101]. Inspection reports and technical papers indicate that other failure types, such as delaminations, adhesive joint failures, shear web/spar cap failures and trailing edge failures, are widespread over the operation time [7].

The occurring failures in wind turbine rotor blades show that their root causes have not been understood well enough to sufficiently prevent them. The reason is that the failure types are complex in their origin and result, in part, as an interplay of complex loading conditions, anisotropic material behaviour, complex geometries, faults during the manufacturing process and damages during transportation and/or installation.

To strengthen the competitiveness of wind power and to ensure that wind turbines operate reliably, it is of great importance to understand and to develop robust methods to predict damage initiation and growth. The purpose of this PhD study is to investigate how multiaxial loading effects influence the ultimate strength of typical composite structures in wind turbine blades and to develop methods to perform reliable prediction of failure. In this thesis, detailed failure origin, propagation and effects, as well as modelling strategies of blade failure are characterised in order to improve blade reliability by understanding failure origin. The project particularly focuses on the topics that follow:

- Strength and stiffness effects of local buckling caused by delaminations in

wind turbine blades.

- Comprehensive trailing edge damage investigations on a wind turbine rotor blade.
- Failure modelling and numerical failure analysis of damages in wind turbine blades.
- Effects of multiaxial loading on the wind turbine structures

The problems are investigated within the framework of solid mechanics, mainly focusing on laminate length to full scale level. Numerical simulations and experimental results are used in order to characterise areas particularly exposed to multiaxial loading and their effect on wind turbine structures.

The term *multiaxial loading* defines load situations, in which a structure is exposed to load combinations of e.g. bending and torsion. This combination is described as a *complex load* or *multiaxial load* [105]. According to Skibicki [105], the relationship between uniaxial and multiaxial loading states and unidirectional and complex states of strain and stress is not always directly related to the similarity of terms (Figure 1.2). Uniaxial loading states can locally evoke multiaxial stress states and requires detailed analysis of the complex stress state as illustrated in Figure 1.2. Multiaxial loading states usually cause complex stress states. In cases where one of the components of the multiaxial loading state is dominating in its properties, uniaxial strength analysis may be sufficient (Figure 1.2) [105].

1.2 Structural challenges of rotor blades

Wind turbine structures are exposed to varying environmental conditions and loads during their lifetime. Besides changing wind conditions with different wind speeds, turbulence intensities, wind directions, wind shear (which especially affects large and/or flexible rotor blades), extreme winds, other site-specific conditions like temperature changes, humidity, radiation and ultraviolet light, rain, snow, hail, ice, lightning, wave loads, and possibly earthquakes can affect the wind turbines [28]. Despite external conditions, manufacturing uncertainties, material properties and design variations also have an effect on the structure and the ultimate capacity of wind turbine blades.

For the design process of wind turbines, all the aforementioned issues have to be considered in order to ensure the structural integrity of the turbine over its anticipated service life of at least 20 years [28]. To account for uncertainties in characteristic values, partial safety factors are applied to both loads and materials parameters [28]. In all cases, the design load should not exceed the design

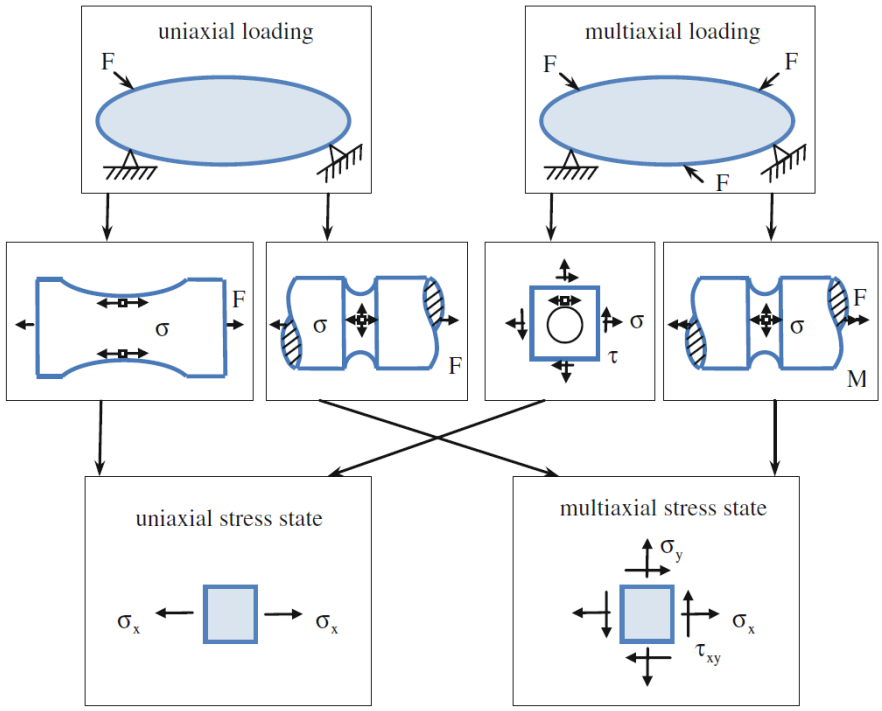

Figure 1.2: Uniaxial and multiaxial loading and uniaxial and multiaxial stress state (taken from Skibicki [105]).

capacity of the wind turbine structure and tower clearance must be maintained. However, as documented by damage and failure reports [7, 124], wind turbines fail due to various reasons.

In this PhD study selected topics regarding the ultimate capacity of horizontal axis wind turbine rotor blades under multiaxial loading were investigated. Consequently, only a condensed overview of the state-of-the-art and a brief introduction into the key aspects of the theoretical background concerning these topics is presented. Furthermore, the challenges and their relevance for wind turbine manufacturers and owners are proposed. This section is not meant to provide a complete state-of-the-art literature review, but rather a summary of key aspects and useful concepts used throughout the presented study.

Chapter 2

Ultimate strength and multiaxial loading

2.1 Ultimate strength and multiaxial loading

Ultimate strength describes the maximum stress that a material can withstand before failing or breaking. The maximum uniaxial material strength (applied load divided by the original cross-sectional area of the specimen) is usually determined in an uniaxial stress-strain test on coupon level. Depending on the investigated material and its characteristics (isotropic/anisotropic, brittle/ductile) different stress-strain curves can occur. Brittle materials usually have a linear stress-strain curve, where failure is reached shortly after exceeding the linear elastic stress-strain region. In contrast, stress-strain curves for ductile materials usually have a linear elastic region and also a non-linear plastic region for loads exceeding the elastic limit, before rupture.

For homogeneous, isotropic materials like most metal specimens, the uniaxial characterisations of the material properties is sufficient. However, composite materials have anisotropic, inhomogeneous material properties. Composite materials arise by forming a structure of two or more constituent materials designed for a specific purpose. Hereby, the characteristics of the individual components are usually utilised as well as possible in order to create a superior overall structure. In consequence, the ultimate strength of composite materials is highly dependant on the load direction and stress state. Uniaxial characterisation of

composites, such as the ASTM D3039 [116] (standard testing procedures for obtaining tensile properties of polymer matrix composites) and others standard testing procedures are well established. However, these test standards are limited in generating useful strength data for composite materials exposed to multiaxial stress states.

In the recent decade, a large body of research on small scale and coupon level has been accumulated to create and improve test methods for composite materials exposed to bi- and multiaxial stresses as described by Escárpita et al. [34]. Nevertheless, material data based on bi- or multiaxial experiments is rare. State-of-the-art for full scale and subcomponent analysis and design is still the usage of material properties determined by uniaxial characterisation.

Beside the ultimate strength parameter on a material level, other physical aspects, e.g. the blade geometry, imperfections, initial defects and damages, affect the ultimate capacity of wind turbine blades [90]. For a more comprehensive view on wind turbine blades exposed to extreme load it is important to asses the ultimate capacity accurately. Methodologies accounting for the physical aspects of structures in the most unfavourable conditions to which a structure may be subjected, are called ultimate limit state-based approaches [90]. In this thesis the ultimate strength assessment follows the ultimate limit state-based approach, which is well recognised to be a much better methodology than the traditional working stress-strain-based approaches [90] because it includes beyond the ultimate strength other effects that can cause failure, as explained in the following.

A limit state describes the conditions beyond which a component or entire structure fails to perform its designated function [90]. Usually, four different types of limit states are characterised [90], namely

- *Ultimate limit state* (ULS)
- *Serviceability limit state* (SLS)
- *Fatigue limit state* (FLS)
- *Accidental limit state* (ALS)

The *Ultimate limit state* (ULS) defines the collapse of a structure due to a loss of structural capacity in terms of stiffness and strength that typically arises from the geometrical collapses (e.g. buckling) of structural components. The *Serviceability limit state* (SLS) describes failure modes in normal operations due to a deterioration in routine functionality. SLS typically represents local damages, unacceptable deformations and excessive vibration and noise that affect the proper functioning. Fatigue cracking of structural details as the result of stress concentration and damage accumulation under repeated loading actions

are characterised as *Fatigue limit state* (FLS). Damage resulting from accidents such as impacts, fire etc. are defined as *Accidental limit state* (ALS) [90].

According to the IEC 61400-1 standard [112], the limit state function can be separated into load and resistance functions S and R in such a way that the condition becomes:

$$\gamma_n S\left(F_d\right) \leq R(f_d) \tag{2.1}$$

where γ_n is defined as the consequence of failure factor, F_d and f_d are functions that describe the design load values and the design material values respectively. The resistance R as a function of $R(f_d) = f_d$ corresponds to the maximum allowable design values of the materials, defined as follows:

$$f_d = \frac{1}{\gamma_m} f_k \tag{2.2}$$

where γ_m is the partial material safety factor and f_k represents the characteristic material properties.

$S(F_d)$ for ultimate strength analysis represents the maximum value of the structural response as a function of the maximum design load, defined as follows:

$$F_d = \gamma_f F_k \tag{2.3}$$

where the partial safety factor for loads is γ_f and F_k is the characteristic value for the load.

Equation 2.1, 2.2 and 2.3 lead to the limit state condition (Equation 2.4) for the ultimate strength assessment of wind turbine components and shall be verified for the most critical limit state [112].

$$\gamma_f F_k \leq \frac{1}{\gamma_n} \frac{1}{\gamma_m} f_k \tag{2.4}$$

The ultimate limit state of wind turbines includes four types of analysis, which shall be performed:

- Analysis of ultimate strength
- Analysis of fatigue failure
- Stability analysis (buckling, etc.)
- Critical deflection analysis (mechanical interference between blade and tower, etc.).

In this PhD study the ultimate strength of wind turbine blade structures under multiaxial loading on full scale level is investigated, where the ultimate capacity is assessed based on the ULS approach. Ultimate strength and stability analyses are the primary focus of this thesis.

The characterisation of generic load interactions, their origin and effects on wind turbine blade structures is examined, where the conception of causal relations is of interest instead of material specific strength properties. Results from numerical analyses and experimental tests are used to study the effect of multiaxial loads on the ultimate strength of wind turbine blade components. Different failure types, loading cases and prediction methods, as well as the ability of different criteria to predict failure under multiaxial loading conditions, are investigated and methods to account for imperfections are studied.

However, the understanding of failure types and mechanical failure modes is imperative for this purpose. A brief theoretical overview into lamina and laminate failure modes and numerical prediction methods is given in this chapter.

2.2 Lamina failure modes

Failure of composite materials occurs differently for different loading situations. According to Puck [93], the different failure types for an unidirectional composite material can be distinguished into *fibre failure* (FF) and *inter fibre failure* (IFF) modes. The failure type (brittle/ductile) and its mode (FF/IFF) depend on the properties of the composite laminate and load direction. Fibre failure occurs when the critical fibre strain is exceeded and the critical fibre strain is smaller than the critical matrix strain ($\epsilon_{fibre} < \epsilon_{matrix}$). In cases where $\epsilon_{fibre} > \epsilon_{matrix}$, inter fibre failure (matrix failure) can occur. Puck differentiates between tensile and compressive failure types. Principal stress aligned with the fibre direction is designated as $\sigma^c_{||}$ for compressive failure and as $\sigma^t_{||}$ for tension. Stresses perpendicular to the fibre direction are labelled as $\sigma^t_{\perp}$ for tension and $\sigma^c_{\perp}$ for compression. Shear stresses are denoted as $\tau_{\perp\perp}$ or $\tau_{|\perp}$ and $\tau_{\perp|}$ depending on the shear direction. The different failure modes are illustrated in Figure 2.1.

As described in Schultz [99], unidirectional composite lamina under compressive stress in fibre direction can fail under out-of-phase micro buckling (low fibre volume content), in-phase micro buckling (high fibre volume content) or shear failure as shown in Figure 2.2 [57]. For laminae exposed to stresses perpendicular to the fibre direction or subjected to shear stresses mainly inter fibre failure occurs. Fibre failure is only found in those cases, where the fibre alignment is a straight-line and the transverse strength of the fibre is very low [57].

According to Puck, inter fibre failure modes can be categorised into three failure

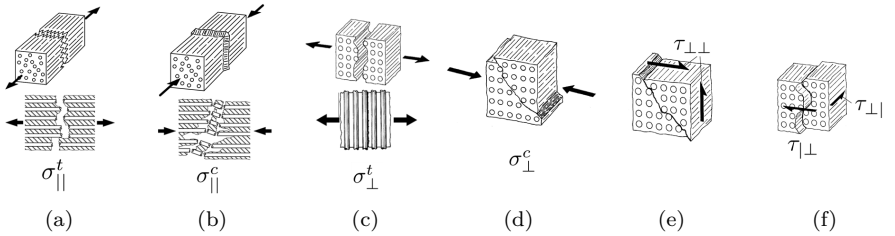

Figure 2.1: Failure types of unidirectional lamina (illustrations taken from Schürmann [100]).

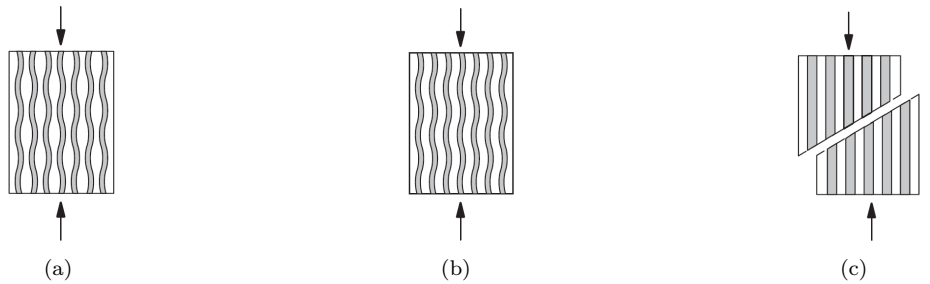

Figure 2.2: Failure types of unidirectional lamina under $\sigma^c_{||}$. (a) Out-of phase micro buckling, (b) in-phase micro buckling, (c) shear failure (illustrations taken from Hörmann [57]).

types (Figure 2.3), described as modus A, modus B and modus C [93]. Modus A occurs for combinations of $\sigma^t_{\perp}$ and $\tau_{\perp|}$ or $\tau_{|\perp}$ respectively. For this kind of load configuration, the unidirectional layer will typically fail in thickness direction. The ply rupture will lead to a redistribution of the stress to the adjacent plies of the laminate. For load combinations of $\sigma^c_{\perp}$ and $\tau_{\perp|}$ modus B or modus C can occur. The fracture type of modus B is similar to those of modus A, except that the evoking transverse loads causing the failure modus B are compressive instead of tensile. Failure modus C is prone to occur under high compressive stresses, which causes the fracture fronts to be pressed together and can form a cuneiform. A high load level is required for failure modus C to occur. Failure modus C is then considered to be more critical than failure modus B, since not only single ply failure occurs, but rather the cuneiform failure can damage adjacent layers and initiate delamination [93].

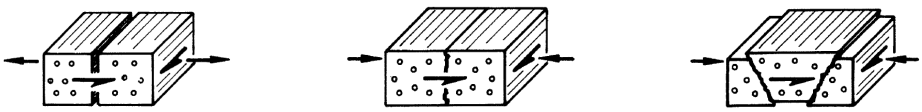

(a) (b) (c)

Figure 2.3: Inter fibre failure types of unidirectional laminates, (a) modus A, (b) modus B, (c) modus C (illustrations taken from Puck [93]).

2.3 Analysis of laminate strength

To identify the inherently complex failure types of fibre laminae and fibre composite laminates, different failure criteria and fracture mechanics models and concepts have been developed. Fibre composite materials are utilised in many applications, facing different challenges, where failure criteria tailored to the specific application often exist, e.g. for composite pressure vessels. Predicting the ultimate strength of fibre composite materials accurately with an universal failure criteria represents a challenge, as demonstrated in the study "Failure Criteria in Fibre Reinforced Polymer Composites: The World-Wide Failure Exercise" [55]. The challenges are based on the heterogeneity and anisotropy of composite materials, the fracture type, mode dependency on loading type and direction, as well as on the chosen material components with its chemical and mechanical properties.

Usually, the analysis procedure of laminate strength is based on the *Classical Laminate Theory* (CLT), which is an extension of the Kirchhoff–Love theory of plates [64]. The Kirchhoff-Love theory has some limitations [52]:

- Small deformations
- Linear elastic material behavior
- Constant plate thickness
- The cross sections remain plane and normals remain normal

In addition to Kirchhoff's assumptions three further assumptions are made [52]:

- Thin single layers are expected to be homogeneous with an isotropic or orthotropic material behaviour
- The layer thickness remains constant

- No slide/relative displacement/shifting between the single layers in the laminate

The CLT reduces complex three-dimensional elasticity problems to a manageable two-dimensional framework. The use of this approach is limited by the assumptions that are necessary to enable two-dimensional simplification [52]. However, the CLT is one of the most used theories and covers a wide field of composite material calculations [52]. In the CLT, a state of plane stress for each individual lamina in a multi-ply composite laminate is assumed [84]. The stresses in the laminae are evaluated separately by transforming the laminate stresses (σ_x, σ_y and τ_{xy}) in the principal material axis direction of each lamina by the use of the transformation matrix $[T]$ given in Equations 2.5 and 2.6 to get the on-axis stresses for the individual lamina (σ_1, σ_2 and τ_{12}) [84]. θ describes the transformation angle between on-axis and off-axis.

$$\begin{bmatrix} \sigma_1 \\ \sigma_2 \\ \tau_{12} \end{bmatrix} = [T] \begin{bmatrix} \sigma_x \\ \sigma_y \\ \tau_{xy} \end{bmatrix} \tag{2.5}$$

$$[T] = \begin{bmatrix} \cos^2\theta & \sin^2\theta & -2\sin\theta\cos\theta \\ \sin^2\theta & \cos^2\theta & 2\sin\theta\cos\theta \\ \sin\theta\cos\theta & -\sin\theta\cos\theta & \cos^2\theta - \sin^2\theta \end{bmatrix} \tag{2.6}$$

Different failure criteria can be applied to determine failure in composite materials based on the stresses and strains calculated from the CLT. The failure mode of a composite laminate is, among others, dependant on the fibre direction and stacking sequence. Most of the existing macroscopic failure criteria can be distinguished into two different failure principles, namely strain and stress based failure criteria. Moreover, laminate failure modes can be differentiated as *first-ply-failure* (FPF) or *last-ply-failure* (LPF) and interlaminar failure [84].

2.3.1 First-ply-failure

For the FPF approach the laminate is considered to be failed as soon as the first ply in a laminate has failed, although other plies could carry the re-distributed load after FPF. FPF describes a rather conservative failure mode, which is mainly described for primary structures. Within the scope of the conducted investigations, maximum strain, maximum stress, Tsai-Hill, Azzi-Tsai-Hill and Tsai-Wu failure theories were used for a preliminary FPF prediction.

The maximum strain, maximum stress, Tsai-Hill, Azzi-Tsai-Hill and Tsai-Wu failure theories represent strain and stress based failure criteria, which post-process stresses or strains from a model and generate an output variable for

the individual failure criterion in order to indicate failure (> 1) or no failure (< 1). Applying these failure criteria to a *Finite Element Analysis* (FEA), the results do not affect the stiffness matrix of the analysed structure. The maximum strain failure criterion and the maximum stress failure criterion are rather simple criteria. Failure is identified when any of the strain or stress components in the principal material axes exceed the corresponding critical value. The components are independently judged and the failure envelope is a rectangle. For the maximum strain criteria, an interaction of stresses based on the Poisson's effect is given and thus the failure envelope is a parallelogram.

The Tsai-Hill, Azzi-Tsai-Hill and Tsai-Wu theories are quadratic, orthotropic plane stress failure criteria normally used for fibre-reinforced composite materials. These criteria calculate an equivalent stress and account for interactions in case of multiaxial stress states. The failure envelopes are ellipses.

The Azzi-Tsai-Hill and Tsai-Hill failure criteria are similar failure theories, and only vary in the definition of the interaction terms ($\sigma_{11} \cdot \sigma_{22}$) indicating material failure (I_F = failure index). This variation leads to differences in the second and fourth quadrants of the failure envelopes (Equations 2.7 and 2.8), which means that differences between both criteria only show up when σ_{11} and σ_{22} have opposite signs [27]. In the following equations, stresses and strengths are defined as follows: σ_{11}, σ_{22} and τ_{12} are components of the stress tensor σ. X_t is the longitudinal tensile strength, X_c the longitudinal compressive strength, Y^T the transverse tensile strength, Y_c the transverse compressive strength, S_l the longitudinal shear strength and S_t the transverse shear strength.

$$I_{F\ Hill} = \frac{\sigma_{11}^2}{X^2} - \frac{\sigma_{11} \cdot \sigma_{22}}{X^2} + \frac{\sigma_{22}^2}{Y^2} + \frac{\sigma_{12}^2}{S^2} < 1.0 \tag{2.7}$$

$$I_{F\ Azzi} = \frac{\sigma_{11}^2}{X^2} - \frac{|\sigma_{11} \cdot \sigma_{22}|}{X^2} + \frac{\sigma_{22}^2}{Y^2} + \frac{\sigma_{12}^2}{S^2} < 1.0 \tag{2.8}$$

If $\sigma_{11} >= 0$, which means that the lamina is exposed to tensile stress in fibre direction (1-direction), then the fibre direction tensile strength will be used as reference strength ($X = X_t$), otherwise the fibre direction compressive strength is $X = X_c$. The same principle applies for the stress perpendicular to the fibre direction (2-direction), if $\sigma_{22} >= 0$ the stress $Y = Y_t$ perpendicular to the fibre direction is taken, otherwise $Y = Y_c$ applies [27].

In contrast to the Tsai-Hill and Azzi-Tsai-Hill failure criteria, the Tsai-Wu failure criterion (Equation 2.9) contains an adaptable interaction term f^* (Equation 2.15), which allows the rotation of the ellipsoidal failure surfaces around the τ_{12}-axis.

$$I_{F\ Wu} = F_1\sigma_{11} + F_2\sigma_{22} + F_{11}\sigma_{11}^2 + F_{22}\sigma_{22}^2 + F_{66}\sigma_{12}^2 + 2F_{12}\sigma_{11}\sigma_{22} < 1.0 \tag{2.9}$$

with the Tsai-Wu coefficients defined as follows:

$$F_1 = \frac{1}{X_t} + \frac{1}{X_c} \tag{2.10}$$

$$F_2 = \frac{1}{Y_t} + \frac{1}{Y_c} \tag{2.11}$$

$$F_{11} = -\frac{1}{X_t X_c} \tag{2.12}$$

$$F_{22} = -\frac{1}{Y_t Y_c} \tag{2.13}$$

$$F_{66} = \frac{1}{S^2} \tag{2.14}$$

$$F_{12} = f^* \sqrt{F_{11} F_{22}} \tag{2.15}$$

where f^* is a scalar within the range $-1.0 \leq f^* \leq 1.0$.

Setting $f^* = 0$ eliminates any longitudinal and transverse stress interaction in Equation 2.9. The scalar f^* affects the surface of the failure envelope significantly and becomes an essential variable for curve-fitting the strength criterion (2.9). For biaxial stress states or multiaxial stresses, the failure envelope in 2D and 3D can be modified. For example, by setting the scalar to $f^* = -0.45$, the ellipsoid will be rotated around the τ_{12}-axes (Figure 2.4). Without considering the interaction term, the extreme points of the ellipsoids intersect the principle stress axes. Figure 2.4 clearly shows that F_{12} is a very sensitive and critical quantity in the Tsai Wu criteria and has to be handled with great care by the users as described by Tsai and Wu [119].

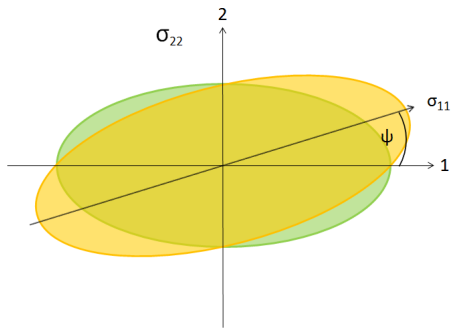

Figure 2.4: Projection of the ellipsoid on the σ_{11} - σ_{22} plane with a rotation (rotation angle = ψ) of the ellipsoid around the τ_{12}-axis.

Although most of the first-ply-failure criteria were developed for unidirectional fibre composites, they can be applied to triax materials as long as the strength

data measured directly for a triax mat laminate will be used as investigated by Laustens et al. in [76].

FPF criteria indicate only the most stressed ply and lamina failure but do not predict the ultimate strength of a composite structure since the results do not have any effects on the stiffness matrix.

2.3.2 Last-ply-failure, a progressive damage and failure approach

To calculate the ultimate strength of laminates, *Continuum Damage Mechanics* (CDM) are applied by the use of *last-ply-failure* (LPF) methods, where stress redistribution and stiffness changes in the laminate after damage initiation are taken into account (Section 3.2). Two different approaches are usually considered, namely total-ply failure or partial-ply failure. For the total-ply failure method, all of the elastic constants describing the lamina are set to zero by exceeding the failure criterion for the individual lamina, whereas partial-ply failure method clears only the elastic constants where the damage variable is reached. Abaqus is used to conduct *Finite Element Analysis* (FEA). The LPF approach in Abaqus is based on Hashin's failure criterion [47, 48, 73, 82] for damage initiation and computes the damage evolution with a damage elasticity matrix, which corresponds to a partial-ply failure method. The procedure of the progressive failure analysis is visualised in Figure 2.5.

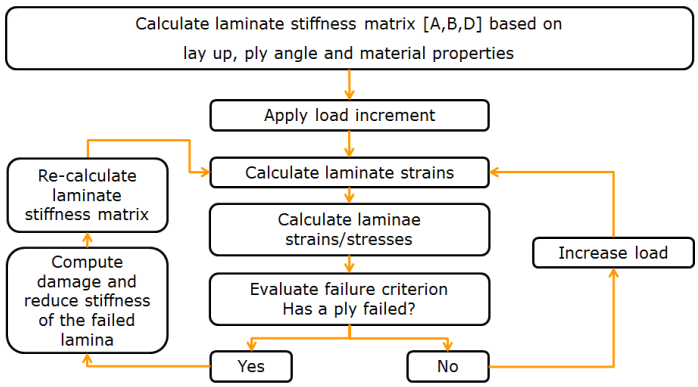

Figure 2.5: Progressive Damage Analysis procedure schematically represented.

If a lamina of a multi-ply composite material fails, its stiffness is reduced and the stiffness of the laminate has to be recalculated. The stiffness matrix for

composite laminates consists of the extensional stiffness matrix (A), the coupling stiffness matrix (B) and the bending stiffness matrix (C). The load will be redistributed to the laminate with the reduced stiffness. If the redistributed load does not cause any further damage on the laminate with the updated stiffness matrix, the load can be increased. This *Progressive Damage Analysis* (PDA) can be repeated until ultimate failure is reached and the structure fails [73, 82]. Figure 2.6 illustrates the LPF approach applied to a displacement-controlled loaded layered composite material exposed to tension simulated in Abaqus.

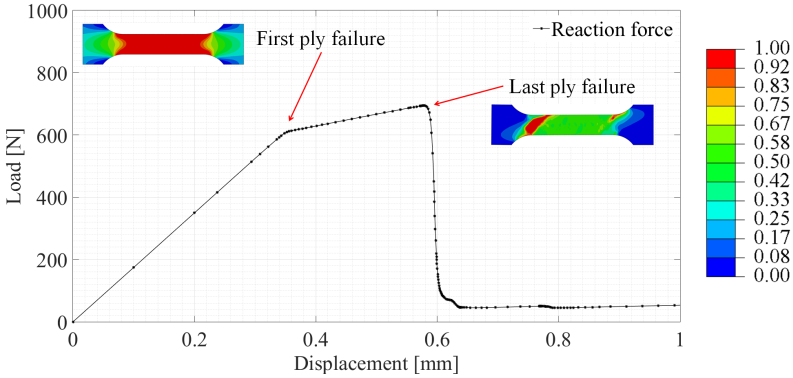

Figure 2.6: PDA of a composite structure exposed to displacement-controlled tension illustrating the LFP approach. FPF occurs in the outer ply with fibres aligned to the load direction. LPF occurs in the ply with 45° fibre alignment. The colour bar indicates the value of the damage variable d.

In Abaqus, damage onset is defined by the Hashin and Rotem initiation criteria [47, 48]. Hashin's criterion distinguishes between fibre and matrix failure and whether the stress is positive or negative. Four different initiation mechanisms are considered: fibre rupture in tension; fibre buckling and kinking in compression; matrix cracking under transverse tension; shearing and matrix crushing under transverse compression and shearing. The initiation criteria are defined as follows:

Fibre tension for $\hat{\sigma}_{11} \geq 0$:

$$F_f^t = \left(\frac{\hat{\sigma}_{11}}{X_t}\right)^2 + \alpha \left(\frac{\hat{\tau}_{12}}{S_l}\right)^2 \tag{2.16}$$

Fibre compression for $\hat{\sigma}_{11} \leq 0$:

$$F_f^c = \left(\frac{\hat{\sigma}_{11}}{X_c}\right)^2 \tag{2.17}$$

Matrix tension for $\hat{\sigma}_{22} \geq 0$:

$$F_m^t = \left(\frac{\hat{\sigma}_{22}}{Y_t}\right)^2 + \left(\frac{\hat{\tau}_{12}}{S_l}\right)^2 \tag{2.18}$$

Matrix compression for $\hat{\sigma}_{22} \leq 0$:

$$F_m^c = \left(\frac{\hat{\sigma}_{22}}{2S^T}\right)^2 + \left[\left(\frac{Y_c}{2S_t}\right)^2 - 1\right]\frac{\hat{\sigma}_{22}}{Y_c} + \left(\frac{\hat{\tau}_{12}}{S_l}\right)^2 \tag{2.19}$$

α is a coefficient that determines the contribution of the shear stress to the fibre tensile initiation criterion and $\hat{\sigma}_{11}$, $\hat{\sigma}_{22}$ and $\hat{\tau}_{12}$ are components of the effective stress tensor $\hat{\sigma}$ (Equation 2.20). Depending on the settings, the initiation criteria can be specialized to obtain the model proposed in Hashin and Rotem [48] by setting $\alpha = 0.0$ and $S_t = Y_c/2$, or the model proposed in Hashin [47] by setting $\alpha = 1.0$ [27]. In the current study the parameter α was set to 1.0 to account for the contribution of shear stress to the fibre tensile initiation criterion.

The failure surface is expressed in the effective stress space $\hat{\sigma}$. The effective stress tensor $\hat{\sigma}$ is the product of the true stress (σ) and the damage operator M (Equation 2.21). The effective stress tensor $\hat{\sigma}$ represents the stress, which effectively resists the internal forces (Equation 2.20) [27]. With increasing damage, the corresponding damage variable (d) increases. Consequently, the nominal value of the damage operator M increases. Thus, the stress multiplied with the stress tensor leads to an increase of the effective stress.

$$\hat{\sigma} = M\sigma \tag{2.20}$$

where M is defined as

$$M = \begin{bmatrix} \frac{1}{(1-d_f)} & 0 & 0 \\ 0 & \frac{1}{(1-d_m)} & 0 \\ 0 & 0 & \frac{1}{(1-d_s)} \end{bmatrix} \tag{2.21}$$

with the internal damage variables (d_f, d_m and d_s) characterising fibre, matrix and in-plane shear damage [27]. The damage variable (d) for a particular mode is given by the following expression and is active after damage initiation, when $\delta_{eq} \geq \delta_{eq}^0$.

$$d = \frac{\delta_{eq}^f\left(\delta_{eq} - \delta_{eq}^0\right)}{\delta_{eq}\left(\delta_{eq}^f - \delta_{eq}^0\right)} \tag{2.22}$$

where δ_{eq}^{0} is the initial equivalent displacement at which the initiation criterion for that mode was met, and δ_{eq}^{f} is the displacement at which the material is completely damaged in this failure mode [27].

Up to damage initiation the material behaviour is assumed to be linearly elastic and so is the stiffness matrix of the orthotropic material. After damage initiation the material response is computed from

$$\sigma = C_d \epsilon \tag{2.23}$$

where ϵ is the strain and C_d is the damage elasticity tensor, which has the form

$$C_d = \frac{1}{D} \begin{bmatrix} (1-d_f)\,E_{11} & (1-d_f)\,(1-d_m)\,\nu_{21}E_{11} & 0 \\ (1-d_f)\,(1-d_m)\,\nu_{12}E_{22} & (1-d_f)\,E_{22} & 0 \\ 0 & 0 & (1-d_s)\,G_{12}D \end{bmatrix} \tag{2.24}$$

where $D = 1 - (1-d_f)\,(1-d_m)\,\nu_{12}\nu_{21}$, E_{11} is the longitudinal modulus and E_{22} the transverse modulus, ν_{12} and ν_{21} reflect the Poisson's ratio and G_{12} the shear modulus [27].

Failure in multi-layer composite structures cannot always be classified into the presented intra-lamina failure types because interactions between different failure modes are common. Also, interlaminar failure between adjacent plies can occur. One of these interlaminar failures is delamination.

2.3.3 Interlaminar failure and delamination

Delamination describes failure in laminated materials, which leads to the separation of adjacent plies. Delamination is characterized as areas with poor or no bonding between adjacent layers of almost equal layer thickness and material properties. The separation of two adhering materials with different thickness and material properties is different to the delamination called debonding. The term debonding characterises the ungluing of an adhered or substrate material from another. Debonding usually describes separation of glued laminates or sandwich structures, which consist of at least one thicker component with a low shear resistance, e.g. core material or adhesive glue, and face sheet materials/thin top layers with high strength properties.

Delamination in composite materials can be induced by poor manufacturing processes; impact damage in service, production or transportation; or originate at areas with high stress concentrations around structural discontinuities such as unreinforced openings with e.g. holes and notches, ply drops, surface cuts or defects. Especially thick laminates, such as spar caps or box girders in wind turbines blades, are difficult to manufacture as described in [71]. For 40 m long

blades the cap thickness typically varies between 30 mm to 50 mm, whereas the cap thickness of 60 m to 70 m long wind turbines blades becomes considerably thicker with approximately 100 mm to 150 mm [71]. The thick laminates are prone to evoke fabrication defects like thermal shrinkage of the matrix during the curing process, insufficient resin distribution, inaccurate lay-up or faults during the thermo-hardening process (internal stresses caused by temperature changes or inadequate heating). These possible manufacturing flaws can affect thick laminates in their material properties and cause high *InterLaminar Stresses* (ILS), provoking delamination [64]. The interlaminar stress as principal stress, perpendicular to the laminated layer as well as *InterLaminar Shear Stress* (ILSS) can arise on the interface between two adjacent layers in a composite material. Typically, ILSS is regarded to be more critical although principal stresses can be more dangerous when occurring as peeling stress [100]. Interlaminar stresses can also be affected by the way in which the laminate is stacked. The more the fibre orientation between adjacent layers differs, the bigger the interlaminar stress is [64].

Delaminations split composite structures into two substructure parts. The basic sublaminate denotes the thicker cross section in the delaminated region whereas its thinner counterpart is termed sublaminate [95].

2.3.3.1 Growth of delaminations

High stress levels in delaminated areas can cause delamination growth for static and fatigue loads. Treating delamination phenomenologically, the propagation of delaminations can cause instability and strength decreases. Looking at delaminations from a discrete fracture mechanics point of view, interlaminar crack growth is characterised by the formation of a damage zone ahead of the crack tip also referred to as *Fracture Process Zone* (FPZ) [120]. The size and crack characteristic of the FPZ depends on the load configuration (Mode I, Mode II and Mode III or mixed mode) as well as on the matrix and fibre characteristics. The crack opening modes I, II and III are shown in Figure 2.7. The damage zone for Mode I loading is smaller than for Mode II and III because the shear stress in the stress field ahead of the crack tip for the shear modes decreases more slowly [120]. Furthermore, the damage zone for a brittle laminate is smaller than for a more ductile composite, since brittle materials absorb relatively little energy prior to fracture [120].

According to Sørensen et al. [111], crack growth in fibre composite materials often shows intact fibres behind the damage front, which the crack has already passed. This extrinsic toughening mechanism is called fibre bridging [109]. The bridging fibres connect the separated sublaminates and restrain further crack opening and crack growth. Thus, fibre bridging increases the fracture toughness of delaminated areas and decreases the risk of unstable crack growth [120, 109].

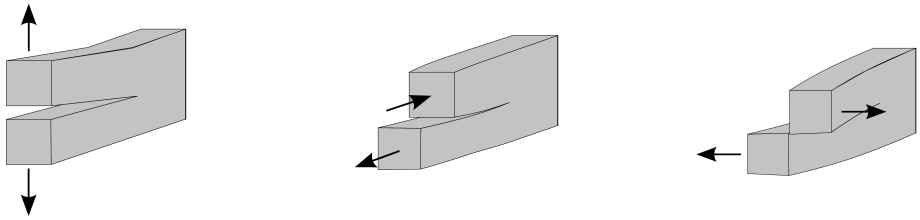

(a) (b) (c)

Figure 2.7: Crack opening modes; (a) Mode I: opening mode, (b) Mode II: in-plane shear mode, (c) Mode III: out-of-plane shear mode.

Observed fibre bridging on small scale specimens (Figures 2.8(a) and 2.8(b)) is characterised and described in detail in [111].

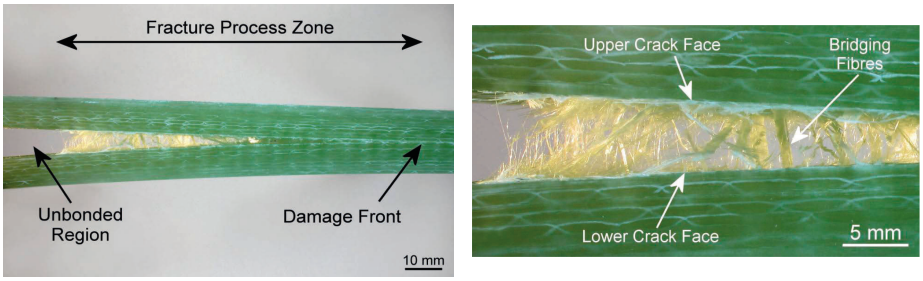

(a) (b)

Figure 2.8: Photographs taken from Sørensen et al. [111] of a large-scale fracture process zone. (a) Fibre bridging along the FPZ from the unbonded region to the damage front. (b) A close view of the FPZ reveals crack bridging by fibres [111].

2.3.3.2 Effect of delaminations

Depending on the size and the location of the delamination, the effect of the defect can, to a greater or lesser extend, be critical. In particular, composite structures exposed to compressive or bending dominated loads are a jeopardy of being split into basic sublaminate and sublaminate. The division is typically accompanied by a significant stiffness reduction due to a reduced critical

buckling and shear stiffness, respectively, such that the structure can fail earlier than expected [63]. Therefore, delaminations are consider to be one of the most critical damages in composite laminates.

On panel level, delaminations located close to the surface, so-called near-surface delaminations, exposed to compressive loading tend to show local buckling behaviour where the sublaminate starts to deform, while the basic laminate usually remains straight (Figure 2.9(a)). For delaminations located deeper inside the composite structure, basic sublaminate and sublaminate may deflect in a similar way and a so-called global buckling mode will occur (Figure 2.9(b)). Global buckling can significantly affect the overall flexural behaviour of the structure for certain load situations as described by Short et al. [103]. Branner and Berring [19] concluded – based on an investigation on the compressive strength of thick composite panels exposed to compressive stress – that local buckling occurs for large delaminations close to the surface, whereas global buckling is caused by smaller and/or deeper located delaminations.

In order to distinguish between local and global buckling behaviour of delaminated structures, the out-of-plane displacements of the two sublaminates can be schematically visualised by two control points. The control points represent the local out-of-plane displacement of the adjacent faces of the separated sublaminates [95]. Similar local out-of-plane displacement of the adjacent sublaminates characterises global buckling behaviour, whereas a drifting apart is typical for local buckling behaviour.

(a) (b)

Figure 2.9: (a) Local and (b) global buckling mode visualised for plates exposed to compressive loading (taken from Short et al. [103]).

2.3.3.3 State of the art to simulate delaminations in composites

Simulations of delaminations in composite materials are usually executed in two steps. Firstly, locations with high risk of delamination occurrence must be predicted. Secondly, the locations with high risk of delamination occurrence are typically modelled with special interface elements to simulate delamination initiation and growth. The second step is necessary to analyse the degradation effect on the structure.

Often first-ply-failure analyses within the field of continuum mechanics are used to predict regions where delaminations could occur. FPF analyses based on the CLT can predict in-plane strain and stress concentrations in the laminate, but are incapable of predicting delamination and its effects on the structure. One reason for that is the assumed simplifications within the CLT, where the ILS ($\perp$) and principal stress ($\sigma_\perp$) are neglected [38]. Although transverse shear components are usually small compared to other stress components, they can induce failure. The other reason is that the separation of the composite structure in the delaminated area is an essential detail of delaminations and has to be considered in analyses. Thus, the computed results from the FPF analyses can be used to localise regions with high risk of delaminations but they are inadequate to predict delaminations and its effects on the structure. This is because important aspects of delamination failure (like the separation of the composite structure and the stresses ILS ($\perp$) and $\sigma_\perp$) are neglected.

After locating critical regions within the composite structure, different approaches for the numerical simulation of delaminations can be used to predict the effect of the defect. The available approaches can be divided into two groups, namely the *Linear Elastic Fracture Mechanics* (LEFM) and the *Continuum Damage Mechanics* (CDM). The LEFM and CDM approaches are described in the next chapter.

Chapter 3

Fracture Mechanics and Continuum Damage Mechanics

3.1 Linear Elastic Fracture Mechanics

In continuum mechanics it is assumed that the mechanical behaviour of an object is modelled as a continuously distributed material, filling the entire region of space [122]. Small scale discontinuities on material level are averaged out. For structures with linear elastic material behaviour, the entire volume is in a linear elastic state and the methods of linear elasticity may be applied [13].

In the field of linear elasticity, the stress distribution in an elastic body can be described with trajectories of the maximum principal stress. The basic problem with this approach is to determine the stress state for elastic bodies with a sharp crack. Griffith [42] noted that strength criterion cannot be applied because stress singularities at the tip of a sharp crack occur. Griffith proposed an energy approach to describe the fracture process and thus originated the basic theory of fracture, *Linear Elastic Fracture Mechanics* (LEFM). Figure 3.1 shows the elastic stress distribution at the crack tip.

The field of fracture mechanics describes the mechanics of sharp cracks, assuming that all of the fracture process takes place at the crack tip [13]. Cracks can

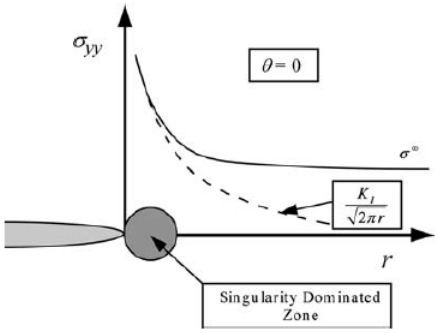

Figure 3.1: Elastic stress distribution at the crack tip. σ_{yy} is the stress in y-direction, r the radial coordinate from the crack tip and K_I the stress intensity factor (taken from Anderson [5]).

be described as a topology discontinuity on a micro mechanics level. Material fracture is assumed when sufficient force and work are applied to break the bonds that hold the material together on an atomic level [5]. A tensile force exceeding the cohesive force is required to separate the atomic bond. The bond energy (E_b) is given by

$$E_b = \int_{x_0}^{\infty} P \, \mathrm{d}x \tag{3.1}$$

where x_0 is the equilibrium spacing and P is the applied force (Figure 3.2) [5].

According to Anderson [5], the cohesive strength at the atomic level can be estimated by idealising the interatomic force-displacement relationship as one half of the period of a sine wave:

$$P = P_c \sin\left(\frac{\pi x}{\lambda}\right) \tag{3.2}$$

where the distance λ is defined in Figure 3.2, x_0 is the origin distance and P_c is the cohesive force. For small displacements, the force-displacement relationship is linear

$$P = P_c \left(\frac{\pi x}{\lambda}\right) \tag{3.3}$$

and the bond stiffness (i.e., the spring constant) can be defined as:

$$k = P_c \left(\frac{\pi}{\lambda}\right) = \frac{EA_0}{L_0}. \tag{3.4}$$

Multiplying both sides of Equation 3.4 by the number of bonds per unit area and the gage length, x_0, converts the bond stiffness k to Young's modulus E

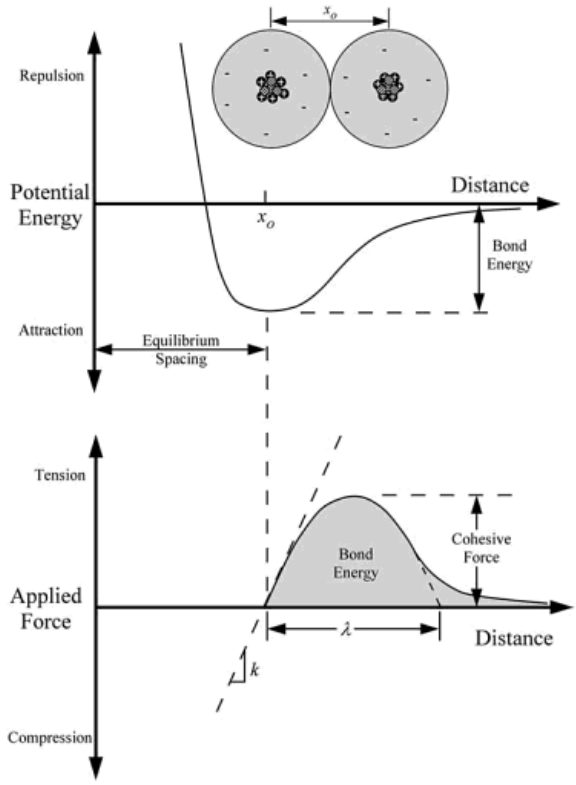

Figure 3.2: Potential energy and force as a function of atomic separation. At the equilibrium separation x_0 the potential energy is minimized, and the attractive and repelling forces are balanced (taken from Anderson [5]).

and P_c to the cohesive stress $\sigma_c = F/A$ [5]. Solving for σ_c gives

$$kx_0 = P_c \left(\frac{\pi}{\lambda}\right) x_0 \tag{3.5}$$

$$\frac{EA_0}{L_0} x_0 = P_c \left(\frac{\pi}{\lambda}\right) x_0 \tag{3.6}$$

$$E = \frac{P_c}{A_0} \left(\frac{\pi}{\lambda}\right) x_0 \tag{3.7}$$

$$E = \sigma_c \left(\frac{\pi}{\lambda}\right) x_0 \tag{3.8}$$

$$\sigma_c = \frac{E\lambda}{\pi x_0} \tag{3.9}$$

$$\sigma_c \approx \frac{E}{\pi} \tag{3.10}$$

if λ is assumed to be approximately equal to the atomic spacing [5].

Experimentally determined fracture strength for brittle materials shows that the theoretical cohesive strength of a material (E/π given by Equation 3.10) is orders of magnitude higher [5] than experimental values. Inglis [58], Griffith [42] and other researchers observed that the discrepancy between the theoretical tensile strength to break atomic bonds and the experimental strength for brittle materials was related to the presence of microscopic flaws in the material, which lower the global strength by magnifying the stress locally [5, 42].

Griffith [42] developed an energy balanced approach, based on the theorem that the potential energy stored in a system will decrease when it goes from a non-equilibrium state to equilibrium [5]. Griffith proposed in [42] that crack initiation or growth will cause a decrease in potential energy stored in the structure by sudden annihilation of tractions acting in its surface. This means physically that for cracks to grow in size, sufficient potential energy must be available to overcome the surface energy of the material. Therefore, crack initiation or growth may only occur if the total energy decreases or remains constant [5]. According to Anderson [5], Griffith energy balance for an incremental increase in crack area dA under equilibrium conditions can be expressed as follows:

$$\frac{dE}{dA} = \frac{d\Pi}{dA} + \frac{dW_s}{dA} = 0 \quad \Longleftrightarrow \quad -\frac{d\Pi}{dA} = \frac{dW_s}{dA} \tag{3.11}$$

where E is the total energy of the system, Π the potential energy supplied by the internal strain energy and external forces, and W_s describes the work required to create new crack surfaces [5].

The potential energy per unit area of crack growth with the unit J/m^2 was defined by Irwin [59] as the strain energy release rate G and describes the available energy in a system to form an increment of crack extension. The term *rate* defines the rate of change in potential energy with the crack area [5]. G is also called the crack-driving force.

$$G = -\frac{d\Pi}{dA} = \frac{overall\ potential}{fracture\ surface} \tag{3.12}$$

The amount of energy, at which crack growth occurs, is the critical strain energy release rate G_c. The latter is a measure of the *fracture toughness* Γ, describing the ability of material containing a crack to resist crack growth. Equation 3.13 defines G and Γ as:

$$G_c = \frac{dW_s}{dA} = 2w_f = \Gamma \tag{3.13}$$

where w_f is the fracture energy, which can be influenced by crack meandering and branching leading to an increase of surface area [5].

The potential energy of an elastic body (Π) is defined as follows:

$$\Pi = U - F \tag{3.14}$$

where U is the strain energy stored in the body and F is the work done by external forces [5]. This means that loading plays a significant role in the stability of cracks. In load-controlled structures, incremental crack growth for Mode I leads to an increase in strain energy due to the applied external force P and the extended crack length (da). The reason for that the size of the uncracked cross section of the structure decreases during crack growth. Thus, the applied load is distributed to a smaller area which again increases the stress in the remaining uncracked cross section. For displacement-controlled loaded structures, the strain energy decreases at crack growth because the crack extension leads to crack opening of the structure, and thus reduces the stress level [5]. This aspect is an important detail for the stability evaluation of crack propagation and for damage tolerance design processes. Whether a crack grows stable or unstable when $G = 2w_f = G_c$ depends on how G and w_f vary with the crack size (a). A *resistance curve* ($R = 2w_f$) or *R curve* describing the material resistance to crack extension is introduced to define the material behaviour for crack extensions. The *R curve* can be constant, rising or falling with increasing crack size (Figures 3.3(a) and 3.3(b)). Moreover, size and geometry of the cracked structure can affect the shape of the *R curve* due to higher stress triaxiality at the crack tip for thicker structures. The critical energy release rate can be determined by experiments and can be understood as the fracture resistance depending on the crack length a where $G_c = R(da)$ with $da = a - a_0$ (Figure 3.4).

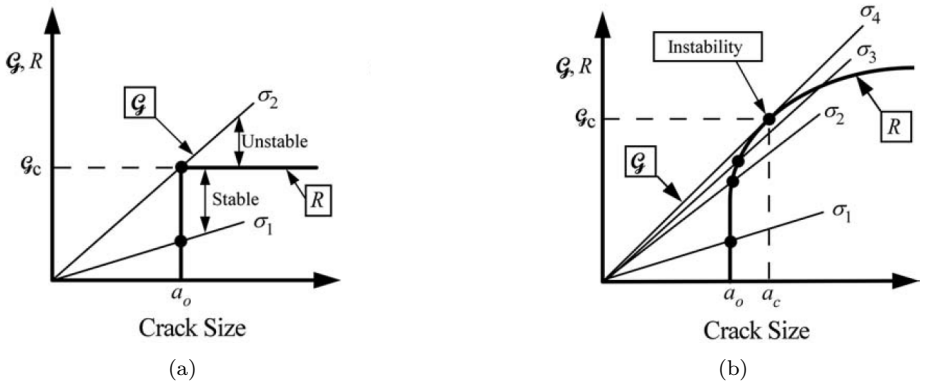

Figure 3.3: Schematic driving force vs. *R curve* diagrams (a) flat *R curve* and (b) rising *R curve* (taken from Anderson [5]).

The conditions for stable (3.15, if the released energy is smaller than the critical SERR), critical point (3.16) and unstable crack growth (3.17) are as follows [5]:

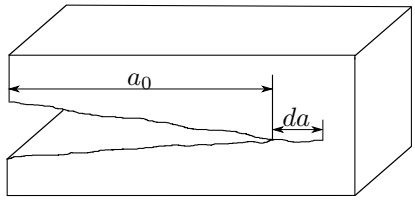

Figure 3.4: Original crack length a_0 and extended crack length da.

$$\frac{dG}{da} < \frac{dR}{da} \tag{3.15}$$

$$\frac{dG}{da} = \frac{dR}{da} \tag{3.16}$$

$$\frac{dG}{da} > \frac{dR}{da}. \tag{3.17}$$

The fracture toughness for materials is determined from the stress intensity factors K_i, describing the stress state near the tip of a crack, at which a thin crack in the material begins to grow [123]. Three different stress intensity factors according to the three different crack opening modes as shown in Figures 2.7(a) to 2.7(c) are defined. Different subscripts are used to designate the stress intensity factors for the different modes. Mode I is designated to K_I, Mode II to K_{II} and Mode III to K_{III}. The modes are related to the stresses acting in the direction. The coordinate system around the crack tip is by convention defined in the way that the x-axis points towards the crack front as shown in Figure 3.5.

The stress intensity factors are defined as follows:

$$K_I = \lim_{r \to 0} \sqrt{2\pi r}\, \sigma_{yy}(r, 0) \tag{3.18}$$

$$K_{II} = \lim_{r \to 0} \sqrt{2\pi r}\, \sigma_{yx}(r, 0) \tag{3.19}$$

$$K_{III} = \lim_{r \to 0} \sqrt{2\pi r}\, \sigma_{yz}(r, 0) \tag{3.20}$$

and results of the near-tip asymptotic field of stress σ_{ij} and displacement u_i. For isotropic materials it has the form:

$$\sigma_{ij} = \left[K_I f_{ij}(\theta) + K_{II} g_{ij}(\theta) + K_{III} h_{ij}(\theta)\right] r^{\lambda - 1} \tag{3.21}$$

$$u_i = \left[K_I \phi_{ij}(\theta) + K_{II} \psi_{ij}(\theta) + K_{III} \chi_{ij}(\theta)\right] r^{\lambda - 1} \tag{3.22}$$

where $\lambda = 1/2$ f_{ij}, g_{ij}, h_{ij}, ϕ_{ij}, ψ_{ij} and χ_{ij} are functions of the polar angle θ [13].

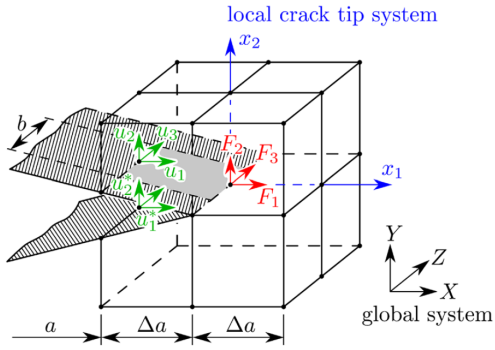

Figure 3.5: Nodal and global coordinate systems of a local crack tip system shown for the *Virtual-Crack-Closure Technique* (VCCT) (taken from Eder and Bitsche [30]).

When only 2-D is assumed the mode-mixity ψ is defined by mode I and mode II stress intensity factor Equation 3.23

$$\psi = \arctan\left(\frac{K_{II}}{K_I}\right). \tag{3.23}$$

This concept applies in the case of identical material properties on both sides of the crack. It does not apply in the case of bi-material interfaces with oscillating stress fields as described by Eder and Bitsche [30].

Based on the aforementioned equations, the LEFM allows the prediction of crack growth, but not without an initial crack [120]. This means that LEFM needs a crack tip with a geometrical starting condition where a stress singularity exists. Several numerical techniques have been developed and described in literature in order to predict the *strain energy release rate* (SERR) and its mode-mixity at the crack tip. The most commonly methods are as follows:

- the *Virtual-Crack-Closure Technique* (VCCT) [69]
- the *Virtual-Crack-Extension method* (VCE) [91]
- the *Crack Surface Displacement method* (CDS) [15]
- the *Finite-Crack-Extension Method* [57, 120]

Crack growth is assumed to occur when these techniques predict critical fracture energies. However, the challenges with these techniques are the computational expenses. In order to predict fracture parameters, e.g. stress intensity factors

or SERRs, nodal variables and topology information from the nodes ahead and behind the crack tip are used. Clearly, this is a big disadvantage of these approaches and can cause difficulties when progressive crack propagation shall be simulated [57, 120]. Furthermore, LEFM approaches always require initial crack existing and cannot predict crack initiation.

3.1.1 Virtual-Crack-Closure Technique

The *Virtual-Crack-Closure Technique* (VCCT) was used to predict the SERR and mode-mixity at the crack front within the content of the PhD study. The VCCT is based on Irwin's assumption [59] stating that a crack incrementally extends when the energy released during crack growth is equal to the work required to close the crack to its original length. In case where SERR is equal to or exceeds the critical energy (G_c), the crack will grow [120]. The SERRs G_I, G_{II} and G_{III} for corresponding opening modes (Mode I, Mode II and Mode III) can be computed from the nodal forces and displacements obtained from the solution of a finite element model as described and illustrated in detail by Krueger in [69].

The SERR according to the VCCT is the work done by the nodal forces required to close the crack tip by one unit area (as shown in Figure 3.5) and is defined as follows:

$$G_I = \frac{1}{2b\delta a} F_2 \delta u_2 \tag{3.24}$$

$$G_{II} = \frac{1}{2b\delta a} F_1 \delta u_1 \tag{3.25}$$

$$G_{III} = \frac{1}{2b\delta a} F_3 \delta u_3 \tag{3.26}$$

where F_i is the nodal forces at the crack tip, δu_i denotes the relative nodal displacement, b represents the element width, and δa describes the element length. The total energy (G_{tot}) released is calculated by adding the individual SERRs for each mode (Equation 3.27).

$$G_{tot} = G_I + G_{II} + G_{III} \tag{3.27}$$

Different approaches exist to define an equivalent SERR (G_{equ}) to relate G_{tot} to. Within this PhD study the Benzeggagh and Kenane [14] definition for (G_{equ}) was used, which is defined as follows:

$$G_{equ} = G_{I_c} + (G_{II_c} - G_{I_c}) \left(\frac{G_{II} + G_{III}}{G_I + G_{II} + G_{III}} \right)^{\lambda} \tag{3.28}$$

where G_{I_c} and G_{II_c} are the experimentally determined Mode I and Mode II fracture toughnesses. The exponent λ describes the mode interaction between G_{I_c} and G_{II_c} depending on the material characteristic.

VCCT is a useful tool for the calculation of the mode-mixity of the SERRs in locations of predefined cracks in order to estimate the driving force directions and critical magnitudes. The VCCT is based on the assumption that crack growth does not significantly alter the state at the crack tip [87]. This means that the displacement ahead of the crack tip (nodes 2-3-4-5 in Figure 3.6) can be assumed to be equal to the displacement that occurs upon crack extension (nodes 1-2-5-6 in Figure 3.6) [87]. This assumption is referred to as self-similar propagation and allows the calculation to be performed in a single FEA. The drawback of the self-similar propagation is that an initial crack must always exist and thus crack initiation cannot be predicted [120]. Moreover, VCCT is based on LEFM and does not take fibre bridging into consideration which limits its application to brittle material. Another disadvantage of VCCT is that it cannot be applied to bi-material interfaces as described by Eder and Bitsche [30]. In order to overcome this limitation another approach for numerical simulation of crack propagation for debonds and delaminations can be used based on the framework of *Continuum Damage Mechanics* [120].

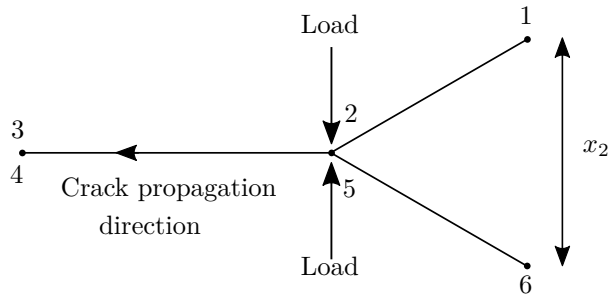

Figure 3.6: VCCT crack opening for Mode I.

3.2 Continuum Damage Mechanics

While fracture mechanics deals with the mechanics of sharp cracks with its focus on the fracture process zone in detail, *Continuum Damage Mechanics* (CDM) treats the fractured/cracked structures phenomenologically [13]. CDM is an engineering approach to model the effects of material damage initiation, propagation and fracture in structures. The effect of cracks in the framework of CDM is usually represented by stiffness degradation models, lowering the material properties in dependency of damage based on thermodynamic and continuum mechanics assumptions. Contrary to the mechanics of sharp cracks around the crack tip as focused on in fracture mechanics, CDM quantifies damage on a

macroscopic level. Within CDM emphasis is put on the effect of the defect regarding the structure as a continuum instead of being focused on the crack itself. Microscopic defects in materials are regarded as effects of smeared and homogeneously distributed defects, representing damage by introducing an internal state variable. The state variable usually describes the damage state and its corresponding material properties. Initially, the state variable represents an undamaged material in full possession of its strength and stiffness. Irreversible damage activation onsets by reaching a damage initiation criterion. After damage initiation, damage progresses based on a damage evolution model describing the degradation of the material can be simulated [127]. Thus, CDM is able to predict both damage initiation and evolution in such a way that damage tolerance and strength analyses can be conducted with the same design tool [120].

3.2.1 Cohesive Zone Models

Aside from the LPF theory mentioned in Section 2.3.2, *Cohesive Zone Models* (CZM) were used for studies in this thesis. The CZM approach can be tracked back to Dugdale [29] who introduced a concept, where cohesive stress is equal to yield stress. Barenblatt [11] proposed cohesive forces on a molecular scale in order to solve the problem of equilibrium in bodies with cracks, and thus introduced the basic concept of CZM. Hillerborg et al. [54] extended the CZM approach by introducing the concept of tensile strength to a model similar to Barenblatt's model. The advantages of Hillerborg's model is that it allows both crack initiation and crack growth [120]. Furthermore, for CZM, mesh topology remains unaltered as the nodes do not separate. The crack opening is modelled by two identical nodes along the crack interface creating a cohesive element. Thus, the opening process is modelled by a softening of the constitutive matrix of the cohesive element.

Crack modelling with CZM is strongly connected to special interface elements, the so-called cohesive elements or contact surfaces, representing the surfaces where crack initiation and propagation can take place. This is of course a limitation because cracks modelled with CZM can only initiate or propagate in the modelled interface (cohesive surface).

Cohesive interfaces do not represent any physical material, but describe the stiffness degradation and softening of the CZM interface represented by traction-separation laws (Figure 3.7). The traction defines the interfacial strength related to the separation of the material. Damage initiation is usually defined as the point, where the maximum traction τ^0 is reached. The constitute behaviour of the crack propagation is characterized by the traction-separation curve. The area under the traction-separation curve represents the critical energy (G_c) needed for crack propagation. When the SERR is equal to the critical energy, then the traction is reduced and new crack surfaces are generated.

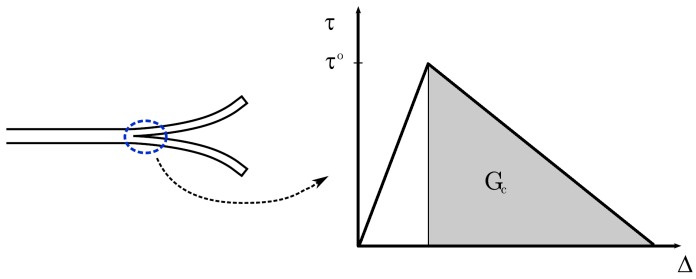

Figure 3.7: Schematic visualisation of a traction-separation curve in the cohesive zone ahead of the crack tip. The white area marks the elastic range, prior to damage initiation. The grey shaded zone the post initiation phase, defined by the critical SERR.

As soon as damage initiation onset crack propagation follows the energy principles:

$$\frac{dG}{da} < \frac{dG_c}{da} \quad \Leftrightarrow \quad \textit{no crack propagation} \tag{3.29}$$

$$\frac{dG}{da} = \frac{dG_c}{da} \quad \Leftrightarrow \quad \textit{stable crack propagation} \tag{3.30}$$

$$\frac{dG}{da} > \frac{dG_c}{da} \quad \Leftrightarrow \quad \textit{unstable crack propagation.} \tag{3.31}$$

For pure single mode loading, delamination initiation onsets for the corresponding mode of the three opening modes (Figures 2.7(a) to 2.7(c)) when the traction (τ_i) reaches the corresponding interfacial strength (τ_i^0). The same applies to delamination propagation when the SERR (G_i) is equal the corresponding critical energy release rate (G_{Ic}) [120]. Under mixed-mode loading, coupling effects between the different crack opening modes for crack initiation and propagation have to be considered. Different approaches are available. In this PhD study a quadratic nominal stress criterion was used to account for the mode-mixity. Damage is assumed to initiate when the quadratic interaction function (Equation 3.32) reaches 1:

$$\left(\frac{\langle t_n \rangle}{t_n^0}\right)^2 + \left(\frac{t_s}{t_s^0}\right)^2 + \left(\frac{t_t}{t_t^0}\right)^2 = 1 \tag{3.32}$$

where t_n (normal traction), t_s(shear traction) and t_t (transverse-shear traction) are the three components of the nominal traction stress vector t. The brackets $\langle\rangle$ represent the Macaulay bracket, which means that values surrounded by the Macauly bracket can only be positive (e.g. $\langle x \rangle = \frac{1}{2}(x + |x|)$), meaning that t_n can only be a tensile stress [27, 120].

The mode-mixity for crack propagation or damage evolution is defined by the Benzeggagh-Kenane (BK) criterion [14]. The BK criterion (Equation 3.28) is particularly useful when the critical fracture energies along the first and second shear direction are the same ($G_{II_c} = G_{III_c}$) [27] which was consistently assumed for the used materials in the presented studies. In principle, G_{II_c} and G_{III_c} can have different values. The problem is only that no valid unbiased G_{III_c} test data exists to date. The BK criterion is defined by the components of the SERRs G_i and the critical energy release rates G_{i_c} as given in Equation 3.28, where λ is a mixed-mode coefficient depending on the material characteristic describing the interaction between the Mode I and Mode II [27]. Figure 3.8 illustrates on a bilinear traction-separation curve the mode-mixity interaction. A study conducted by Alfano [4] clarified that bilinearly shaped traction-separation curves represent the best compromise between computation cost and accuracy out of four investigated cohesive laws. In Alfano's study bilinear, trapezoidal, exponential and linear-parabolic laws for typical double-cantilever-beam under static tests were investigated [120]. Therefore, bilinear traction-separation curves were consistently used throughout the performed numerical simulations in this thesis.

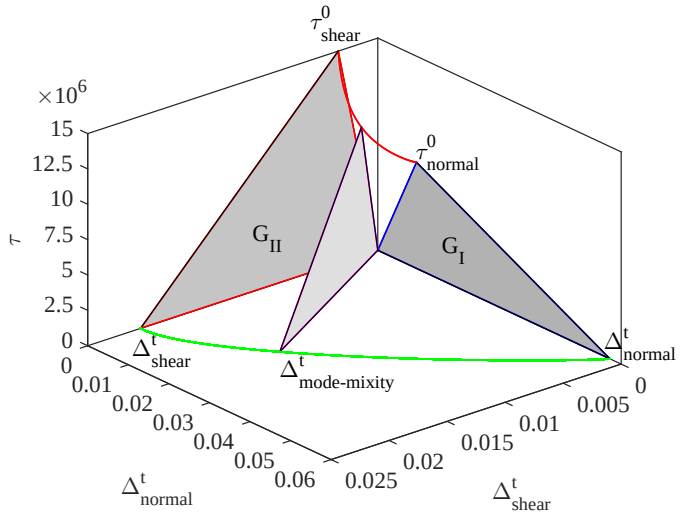

Figure 3.8: Schematic visualisation of a traction-separation curve for mode-mixity.

The CZM has also some drawbacks. The CZM usually requires an extremely high mesh resolution to accurately predict failure on small scale. Between three

and ten elements are suggested to use within the cohesive zone length, representing the FPZ [120, 21, 22]. This makes the numerical simulations computationally expensive or limits the application to small areas. Turon [120] proposed a method to handle also large scale modelling with cohesive elements but the methods requires an artificial lowering of τ_0. Furthermore, CZM is element type and element size dependent, which to date has not been resolved. Moreover, the availability of mixed mode traction-separation laws is extremely limited and additional testing and measurement methods are required. In addition, numerical stability of this highly non-linear problem is poor which in combination with the high mesh resolution makes this method less applicable to engineering practise. However, the method gives valuable information about crack growth processes and effects on the structural response which less sophisticated methods cannot provide in the same content.

Chapter 4

Failure types and applied fracture mechanics for wind turbine blades

A major contribution to downtimes on turbines are blade issues. According to a study from the *National Renewable Energy Laboratory* (NREL) published in a report by Sheng [101], the contribution of rotor blade issues to the total downtime of wind turbines ranges between 8 % and 20 %. Moreover, in an article written by Wittrup [124] it was announced that all 273 rotor blades of Horns Rev 2 wind park in Denmark will be repaired and upgraded to increase production capacity. Significant deterioration of the blades after only six years of operation motivated Dong Energy and Siemens to undertake this big makeover [124]. Consequently, research on structural problems that may improve blade designs, and in this way increase lifetime, offers a great cost saving potential for blade manufacturers as well as operators. However, literature dedicated to failure in wind turbine rotor blades is scarce.

Figure 4.1 shows an overview of a cause and effect analysis of blade failure. External conditions like temperature, chemical environments, humidity and radiation are not listed but also affect the rotor blade reliability.

In the following sections of this chapter, the structural design of wind turbine rotor blades and frequent failure types, that have been investigated within this PhD study, with potential to cause ultimate failure, are presented.

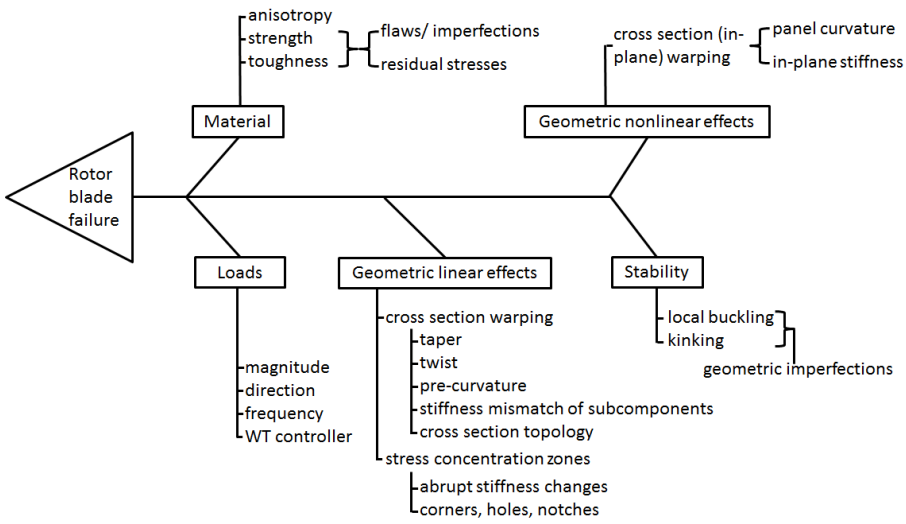

Figure 4.1: Fish bone diagram of possible sources of rotor blade failure.

4.1 Structural design of rotor blades

The structural design of horizontal axis wind turbines rotor blades usually consists of a hollow profile formed by two asymmetrically shaped shell structures glued together [28]. The streamlined upper and lower shell form the aerodynamic suction and pressure side of the rotor blade and carry a part of the bending loads. In order to increase the strength and stiffness, shear webs are glued onto the upper and lower shell in the interior of the blade. The spars/shear webs carry the shear load and part of the bending loads [28]. Moreover, they restrain the cross section against transverse deformation and the panels/caps against buckling. The shear webs in conjunction with strong shell structures, the so-called caps, form a boxlike structure, acting as the load carrying structure of the blade (Figure 4.2). Sandwich structures are often used to increase the moment of inertia of area and thus to prevent buckling. Sandwich concepts are primarily used in the shear webs, trailing edge panels and leading edge panels [126, 28].

In general, the blade geometry constitutes a mix between structural considerations and aerodynamic properties. Blade profiles usually consist of a strong, circular root section, in order to withstand the high loads. Blade profiles show thinner sections along the blade span, where the loads are lower and the aerodynamic shape becomes more important. In between the strong, circular root

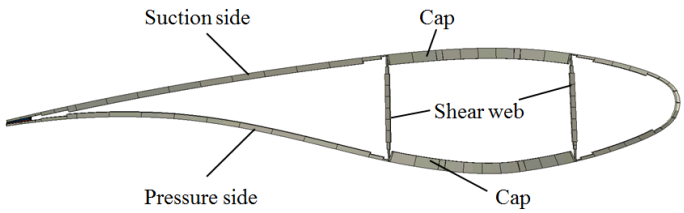

Figure 4.2: Cross section of a blade showing the upper and lower shells connected to shear webs at the thick cap sections.

section and the thinner, highly aerodynamic shaped blade section towards the blade tip, a transition zone with significantly tapered blade profiles exist (Figure 4.3). Not only the aerodynamic shape of the cross sections along the blade span changes, but also the orientation of the chord line. The reason for that is the change of direction of the resulting wind due to an increase in rotational speed from the blade root towards the blade tip. To account for these changes, the blade profiles are twisted along their axis. The twist angles between the chord of the blade profile and the rotor plane creates a highly non-linear geometry (Figure 4.4) [28].

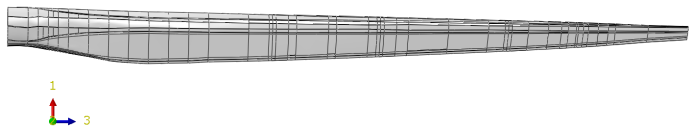

Figure 4.3: Side view of a 34 m rotor blade profile designed for a wind turbine with a power capacity of 1.5 MW.

4.2 Stability analysis and geometric effects

Stability analyses (e.g. buckling analysis) and the study of geometric effects (e.g. twist, ovalisation) are essential for the ultimate strength assessment of wind turbine blades. The reason for that is the complex blade geometry, with its hollow and to some extend thin walled shell structures, which makes wind turbine rotor blades prone to buckling failure mode [61, 62]. The critical buckling load is very depended on local cross-sectional deformation, which is a highly non-linear phenomenon and varies depending on the load configurations [96, 61, 31, 32]. Cross-

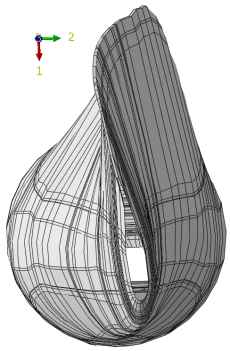

Figure 4.4: View of a blade from the blade tip towards the root, illustrating the twist of the blade.

section deformations are often provoked by combined load situations, where e.g. bending moments and torsional moments act simultaneously.

Rotor blade trailing edges are very sensitive to stability effects like local buckling or fibre kinking, which are usually caused by geometrical imperfections. Small manufacturing deviations with respect to the trailing edge shape or the fibre alignment can effect the structure significantly. Also the load carrying capacity of wind turbine rotor blades is highly dependant on the load direction. While rotor blades can deal with high flapwise bending moments, load directions exposing the trailing edge to compressive stresses can lead to trailing edge buckling and failure at a much lower load.

Moreover, wind turbine blades are slender beam-like structures made from composite materials. This allows the blades to undergo tip deformations in the flapwise direction of up to 20 % of their span [31]. These large deflections, in conjunction with high out-of-plane and low in-plane cross-section stiffness, lead to geometric non-linear in-plane cross-section deformations. This bending-induced in-plane warping effect is also referred to as *Brazier effect* or *cross-section ovalisation* and has been investigated by Damkilde and Lund [26] as well as Cecchini and Weaver [23]. These deformations can, among others, lead to high compressive stresses in the load carrying cap/shear web regions and may cause buckling.

With ever increasing blade length, stability against buckling will most likely be a design driver. Therefore, non-linear calculations concerning buckling and non-linear wrapping issues as well as geometrical imperfections, fibre misalignment and manufacturing accuracy should be taken into account [28].

In all four papers within this thesis, buckling phenomena are analysed and discussed. Paper A deals with the effect of delaminations on local buckling in

the load carrying cap of a large wind turbine blade. In this context, the effect of imperfections on the buckling analysis is discussed. In Paper B, the effect of local instabilities at the trailing edge on the SERR is analysed. In Paper C, the impact of buckling onset in the trailing edge on the ultimate strength of a 34 m wind turbine blade is analysed. Paper D reveals the importance of non-linear stability analyses on the ultimate strength of a wind turbine blade exposed to varying load directions and magnitudes.

4.3 Delamination

Wind turbine rotor blades are usually made of fibre composite materials and sandwich composite materials with foams or woods as core materials since rotor blades are large rotating structures, exposed to dynamic loads, light-weight, high-strength-to-weight-ratio and good fatigue properties are necessary criteria for the materials used. Typically, glass fibre mats with unidirectional, biaxial or triaxial fibre orientation with different material properties, moduli and strengths are used. Some manufacturers also use carbon fibres in the caps, to strengthen the load carrying structure, due to the higher tensile moduli of carbon fibres compared to glass fibres. Polyesters and epoxies are used as resins to impregnate the fibre mats [28].

Usually, the fibre mats are put into negative forms by hand. Subsequently, the fibre mats are covered with plastic foils and vacuum is introduced. Then, an infusion process starts, where resin flows because of the atmospheric overpressure into the mould. The *Vacuum Assisted Resin Transfer Moulding* (VARMT) process is mainly used, because of good laminate quality and the relatively low manufacturing costs. However, the quality and accuracy of the layup and the infusion process highly depends on the individual skills of the worker and provided flow media. Especially thick laminates, such as spar caps or box girders, are difficult to manufacture and fabrication defects can occur from thermal shrinkage of the matrix during the curing process, insufficient resin distribution, trapped air, inaccurate lay-up or faults during the thermo-hardening process [71]. Among others, fabrication defects can provoke delamination in the caps [64].

The effect of delaminations on the load carrying capacity of a large wind turbine blade was studied numerically and is described in Paper A. The study showed that for initial delaminations with a width of 30-50 % of the cap width, delamination close to the surface started to grow in load ranges of normal operation conditions and led to local buckling modes. The local buckling caused high strains and stresses in the surrounding of the delamination, which exceeded the material design properties and therefore should be considered dangerous. Delaminations placed near the mid-surface of the cap did not have a significant effect on the blade response under static loads for load magnitudes referring

to normal operation conditions. In the simulations the static load exceeded the design load by more than 40 % before delamination growth or cap buckling occurred. It was concluded that delamination induced near-surface buckling modes have to be considered critical due to an onset of local sublaminate buckling below the design load level.

4.4 Loads - Ultimate loads

Wind turbine structures are exposed to a variety of different loads as described in Section 1.2. The load carrying capacity of composite materials in general, and wind turbine structures in particular, are highly depending on the load direction. To determine the ultimate capacity of wind turbine rotor blades under multiaxial loading, it is important to assume correct loads. Numerical simulation tools based on the *Blade Element Momentum* (BEM) theory such as HAWC2 [49], Bladed [17], FAST [35] etc. are usually used to perform the load calculations.

In the context of this PhD study, aero-elastic simulations based on the in-house aero-elastic code HAWC2 [49, 75] were conducted for a 34 m long wind turbine blade with a rated capacity of 1.5 MW. The results from the conducted load analyses were used as reference loads. In Paper D, the aero-elastic simulation procedure and analyses, as well as a load envelope are described in detail. Moreover, the multiaxial loading as a combination of bending and torsional moments are described and its effects on the ultimate strength assessment evaluated.

In Paper B, the effects of geometrical non-linear cross-section deformation and trailing-edge wave formation on the energy release rates were investigated based on aeroelastic load simulations. The paper concludes with a discussion about critical loading directions that trigger two different non-linear deformation mechanisms and their potential impact on adhesive trailing-edge joint failure.

4.5 Bondline challenges

Aside from Siemens Wind Power's patented IntegralBlade technology, most of the current wind turbine design and manufacturing concepts are based on the aforementioned separated production of multi-material sub-components, where the sub-components are finally joined through adhesives. Adhesive joints exit usually at the unification between the upper and lower aerodynamic shells at the leading and trailing edge, as well as around the load carrying structures between shells and shear webs/spars or box girder (Figures 4.5(a) and 4.5(b)). In this PhD study only trailing edge failure was studied in detail.

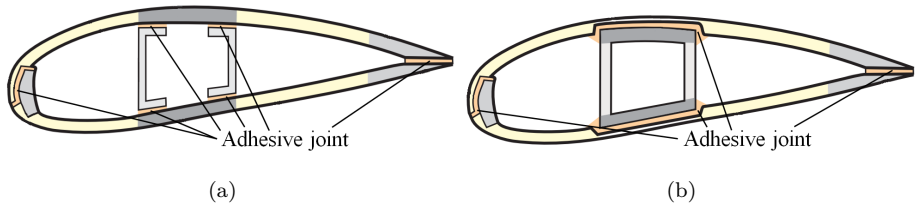

Figure 4.5: Schematics of the cross-section of two common design principles of wind turbine blades. (a) A design that uses load-carrying laminates in the aeroshell and webs to prevent buckling and (b) a design that uses a load-carrying box (taken from Sørensen [107]).

4.6 Trailing edge failure

Trailing edge failure is a very complex issue, with a huge cost and liability impact, and to date a poorly understood phenomenon. Publicly available research regarding trailing edge failure has been conducted by Ataya and Ahmed [7], Eder and Bitsche [30] and Eder et al. [33, 32]. Ataya and Ahmed [7] investigated mainly the forms, location and root causes of damage to wind turbine blade trailing edges based on data for small wind turbines with a capacity of 100 kW and 300 kW. They conclude that most of the trailing edge failures occur at 0.73 of relative rotor length, at locations highly exposed to fatigue loads. Eder and Bitsche [30] investigate based on the estimation of the *Strain Energy Release Rates* (SERRs) systematically potential design drivers causing trailing edge failure for different opening angles of the trailing edge [33]. For simplified models, an analytical solution based on contour integration with the J-integral for parallel crack faces was used. The *Virtual Crack Closure Technique* (VCCT) was applied to calculate the SERRs for various load conditions and opening angles of non-parallel cases. The authors concluded that the SERRs of a typical blade section, subjected to various loading conditions, is Mode III governing. Accordingly, flapwise shear and torsion are the most important load cases [33]. In Reference [30], the effect of differently shaped adhesive flow fronts on the SERRs and the mode-mixity for three different adhesive flow fronts for *Double Cantilever Beam* (DCB) specimens loaded with uneven bending moments is described. Furthermore, the authors conducted a non-linear numerical study on a blade section analysing the relationship between non-linear effects, SERRs and mode-mixity. They concluded that local buckling induces significant SERR levels in the trailing edge joint [30]. In Reference [32], the Eder and Bitsche investigate the effects of geometrical non-linearity on SERR of transversely oriented cracks in the trailing edge, using a numerical slice model of a blade cross section. They conclude a critical bending moment vector direction angle sector

of 277° - 279° for DTU Wind Energy's 10 MW light rotor reference blade. Furthermore, Eder et al. mention in Reference [32] that the SERR magnitudes in the trailing edge joint is rather low ($G_{tot}/G_{equ} \ll 1$) unless the cross-section is subject to excessive loads, neglecting Mode-III effects and local buckling, which can not be handled by the slice approach.

Contrary to the small amount of available information specifically related to trailing edge failure in rotor blades, a lot of research on fundamental and general adhesive bond failure mechanism, material properties, calculation and simulation methods, failure modes and mode-mixities has been conducted and published e.g. by Sørensen et al. [110, 109], Camanho and Davila [22], Turon [120], He [51] and Kenane and Benzeggagh [66, 14] in recent years.

Sørensen et al. [110, 109] contributed considerably to the understanding, testing and modelling of adhesive joints in composite materials. Their experiments and theoretical approaches delivered valuable input for design processes of experiments and for numerical analyses, e.g. CZM, as well. Moreover, their experiments, mainly on DCB test specimens loaded by uneven bending moments, showed that the fracture resistance of adhesive joints consist of large-scale fracture process zones, composed of a crack tip and a fibre bridging zone. Furthermore, analytical solutions for the calculation of SERR of adhesive joints with dissimilar materials were derived. Xiaocong He [51] conducted intensive review of finite element analysis of adhesive joints. Xiaocong He concluded that the behaviour and debonding process of adhesive joints depend on the complex interaction of geometry, mechanical properties and hygrothermal behaviour. Camanho, Davila [22] and Turon [120] are experts in the field of numerical fracture mechanics and cohesive zone modelling. Their research has significantly contributed to improving computational methods in this field. Moreover, Turon proposed an approach to realise large scale modelling with CZM. Kenane and Benzeggagh [66, 14] contributed with research related to mixed mode behaviour and its characterisation to the field of CDM.

In Paper B, a comprehensive numerical investigation of energy release rates at the tip of a transversely orientated crack in the trailing edge of a 34 m long blade for a 1.5 MW wind turbine is presented. The effects of geometrical non-linear cross section deformation and trailing-edge wave formation on the energy release rates were investigated. The paper concludes with a discussion about critical loading directions that trigger two different, non-linear deformation mechanisms and their potential impact of adhesive trailing-edge joint. In the article, the root causes of trailing edge failure are investigated by presenting the complex problem split into the relevant failure causes presented in a fishbone diagram. In that way, critical SERR modes, load directions and geometrical trailing edge opening and closing could be shown.

In Paper C, the reliability and accuracy of a numerical shell model and the prediction capabilities of existing failure criteria and approaches are compared

to experimental findings of a blade tested to ultimate failure. The experimentally obtained blade response, based on measurements from linear cable position sensors catching the global blade displacement as well as the use of *Digital Image Correlation* (DIC) techniques evaluating local trailing edge deformations, was compared with numerical simulations. The study shows in detail how the interaction between trailing edge buckling and sandwich panel failure led to blade failure. FPF methods and progressive damage mechanics techniques were used to analyse blade failure. Here, the CDM models significantly improved the accuracy of ultimate strength prediction, whereas the limitation of FPF methods capturing relevant failure modes in blade structure was clearly demonstrated. Furthermore, the sensitivity of trailing edges to show local instabilities was demonstrated and consequential the effects as a series of events leading to failure were shown.

Chapter 5

Conclusions and future work

The research conducted within this PhD study aims at the investigation of multiaxial loading effects and its influence on the ultimate strength of typical wind turbine rotor blade structures. For this purpose, origin and consequence of some of the typically occurring failure types in wind turbine rotor blades were investigated. The main contribution from this PhD study towards more reliable and robust operating wind turbine systems can be divided into two fields. One part covers numerical modelling approaches and the other part deals with failure origin and effects.

5.1 Numerical modelling approaches

Paper A deals with buckling and delamination modelling in wind turbine blades. An approach was demonstrated, where a region, discretised with shell elements, was replaced by a subset of brick elements connected to the remaining shell element model. Cohesive elements within the subset model, consisting of brick elements, allowed to simulate delamination initiation and growth prediction. The contribution in the field of delamination growth modelling on large scale in wind turbine blade is the coupling between the shell model and the highly discretised brick element subset model. This approach allowed very detailed delamination modelling of a local failure under consideration of realistic, interactive boundary conditions. The great advantage of interactive boundary

conditions is that blade deformations from the shell model are not only externally provided boundary conditions but rather influenced by the response of the subset model including damage initiation and damage propagation. This highly discretised and interactive sub-modelling approach made it possible to directly predict the effect of delaminations on a wind turbine blade structure. Moreover, the demonstrated subset modelling approach allowed to study the delamination behaviour and to analyse the load carrying capacity of the blade with realistic boundary conditions. Thus, the critical delamination size and load level for delamination growth onset and propagation in dependency of the through thickness location could be determined more precisely.

In Paper B, a rather simple but effective way of trailing-edge modelling with the purpose of determining the SERR in a transversely orientated crack in the trailing edge was demonstrated. The coupling between the highly discretised brick element subset model to a shell model allowed to predict the SERR based on the VCCT. The demonstrated approach allowed to predict the SERR in the trailing-edge bondline embedded in a comprehensive blade model, meaning that not only the trailing-edge crack was modelled but rather the entire blade. This approach has the advantage that the highly complex trailing-edge failure process with the interaction between geometry, material, loads and stability effects leading to trailing-edge failure, can be analysed. Thus, all important effects could be considered in the numerical model and allowed to investigate how they affect trailing-edge failure.

In Paper C the accuracy of an extended numerical shell model to predict ultimate failure is described. FPF criteria and CDM approaches for the prediction and simulation of failure in a wind turbine blade, loaded to ultimate failure, were analysed and compared to experimental findings. The investigation clarified the strength and weakness of plane stress failure criteria and makes the reader aware of not identified phenomena by the use of in-plane theories. Apart from the good agreement between the Hashin failure prediction in comparison to the experimental data, the study clearly demonstrates the limitation of in-plane, first-ply-failure criteria with regard to pure laminated composite materials in its inability to reveal core shear failure in the sandwich structure. Furthermore, the study shows the importance of shear stress analysis for sandwich construction. The work synthesizes experimental and theoretical-computational studies yielding results with direct engineering significance for wind industry in order to improve the numerical prediction accuracy of simple finite element analyses based on shell elements.

5.2 Failure origin and effects

In Paper A, the effect of delaminations in the caps of a blade section was studied with the aim of assessing the danger of delaminations on the load carrying capacity of wind turbine rotor blades. It was found that blade structures with initial delaminations with a width between 30-50 % of the cap width, positioned close to the surface, showed the danger to propagate in load ranges of normal operation conditions and could lead to local cap opening buckling modes. The local cap opening buckling modes caused only little bending stiffness reductions of less than 1.5 % compared to the intact structure. Nevertheless, the near-surface local cap buckling modes led to high strains and stresses in the area surrounding the delamination. Therefore, near-surface delamination has to be considered critical. Full cap buckling for the investigated blade and delamination configurations, showed not to have any significant effect on the blade response under normal operation conditions. In the simulations, the static load exceeded the design load by more than 40 % before delamination growth onset or buckling occurred. The conclusion, based on the study described in Paper A is, that the load threshold of delamination propagation is highly depending on the location and size of the initial delamination. Delamination induced local cap opening buckling modes have to be considered to be more critical due to an earlier onset of local cap opening buckling compared to full cap buckling modes.

Paper B deals with the effects of geometrical non-linear cross section deformation and trailing-edge wave formation on the energy release rates. The main contribution from this work can be summarised as follows. It could be demonstrated both experimentally and numerically that a geometric non-linear longitudinal trailing-edge wave can occur in blades which are designed to prevent local buckling already at lower load level. Such a wave can have serious consequences for the integrity of the adhesive trailing-edge joint, since trailing-edge wave suppressed G_I and amplified G_{II} and G_{III} in the investigated blade model. Such induced SERR levels can lead to adhesive joint failure under maximum design loading conditions. This knowledge led to the conclusion that trailing-edge subcomponent tests should not only examine Mode-I fracture but also mixed mode conditions. However, the numerically obtained G_I levels exceeded experimentally obtained fatigue thresholds of adhesive joints and thus Mode-I failure should be considered, too. Furthermore, it was found that surface strain measurements on laminates with FBGs were influenced by local effects (e.g. material imperfections) leading to strain concentrations, and by the alignment between the fibre reinforcement and the FBG sensor. Moreover, based on a numerical study, two critical bending moment vector directions emerged in the investigated case. The first occurred at α=135° and is consistent with the Brazier effect reported in [31]. The second occurred at approx. α=240° and is associated with geometrically non-linear wave formation.

Paper D shows an approach to improve the design process of wind turbine rotor blades and simulations by using a 3D load envelope. This approach, under consideration of non-linearity, makes it possible to analyse the entire blade structure for different load directions and their extreme loads. Furthermore, the impact of torsion on the blade response was demonstrated.

5.3 Future work

The performed research in this PhD study showed that trailing-edge deformation can cause high SERR, due to high shear stresses in the pre-cracked bondline. Future work on the ultimate strength assessment of wind turbine rotor blades under multiaxial loading should aim at the relationship of blade geometry and strain and stress distributions. Focus should be put on geometries reducing the danger of trailing-edge failure by redesigning the trailing edge/bondline region. This is a highly challenging topic, since the structural design should avoid changes in the airfoil geometry, because the airfoil camber has a significant effect on the aerodynamic performance.

Furthermore, the performed studies have shown that blades, exposed to extreme loads, response with highly non-linear deformations, where geometry details, anisotropic material behaviour and load components can have a huge impact on local the strain and stress state. Moreover, the studies have shown that FEA can predict very accurately the global response of large scale structure but determining local phenomena of e.g buckling sensitive structures such as trailing edges, can be challenging. Therefore, the ongoing validation of FEA based on experimental results is necessary. Due to the highly non-linear deformations of rotor blades, it would be optimal to investigate local structural phenomena based on full scale experiments in order to consider all possible effects. However, rotor blades getting larger and thus testing becomes more expensive, meaning that this approach is not feasible. Instead, research focusing on hybrid testing methods should be performed to create interactive boundary conditions of tested subcomponents. The subcomponent should be embedded in a test environment, where the boundary conditions can imitate the virtual blade response based on FEA, and thus account for the highly complex deformation state of wind turbine rotor blades.

Part II

Publications

Paper A

The effect of delaminations on local buckling in wind turbine blades

---

Article status: Accepted for publication on the 21^{st} of June 2015.

Article title: *The effect of delaminations on local buckling in wind turbine blades*

Authors: P. U. Haselbach, R. D. Bitsche and K. Branner

Journal title: Renewable Energy (2016) pp. 295-305 (the article is available online)

DOI information: 10.1016/j.renene.2015.06.053

A.1 Abstract

In this article the effect of delaminations on the load carrying capacity of a large wind turbine blade is studied numerically. For this purpose an 8.65m long blade section with different initial delaminations in the main spar was subjected to a flapwise dominated bending moment. The model was setup in Abaqus and cohesive elements were chosen for modelling delamination growth.

For initial delaminations with a width of 30-50% of the cap width the study showed that delamination close to the surface started to grow in load ranges of normal operation conditions and led to local buckling modes. The local buckling caused high strains and stresses in the surrounding of the delamination, which exceeded the material design properties and therefore should be considered as dangerous.

Delaminations placed near the mid-surface of the cap did not have a significant effect on the blade response under normal operation conditions. In the simulations the static load exceeded the design load by more than 40% before delamination growth or cap buckling occurred.

It could be concluded that delamination induced near-surface buckling modes have to be considered critical due to an onset of local sublaminate buckling below the design load level.

A.2 Introduction

Areas of poor or no bonding in the interface between adjacent layers of a composite material are defined as delaminations. These interlaminar gaps/cracks normally originate from manufacturing flaws, areas with high stress concentrations around structural discontinuities such as holes, notches, ply drops or connections, or from impact damage during production, transport or service [64, 93, 100].

Delaminations embody a local separation of the laminated composite structures into sublaminates. The critical buckling load of the sublaminates may be well below the critical buckling load of the original structure. Consequently, the presence of delaminations may lead to a reduction of structural stiffness and strength. Due to this delaminations in laminated composite structures are considered to be the most critical type of damage that composite structures under compression can experience [92, 2, 117].

Delaminations in composite structures can trigger different buckling mode shapes, which poses different levels of danger to the structure. Considering buckling on a panel level the buckling behaviour of the structure with a delamination

can be divided into local and global buckling modes (see Figure A.1) as well as into other combinational modes. A local buckling mode shape represents deformations of mainly one sublaminate on one side of the delamination. This local buckling mode will then introduce bending of the buckled sublaminate and reduce its load carrying capacity. Therefore, the other sublaminate will be subjected to higher compressive loading and additionally experience bending caused by the adjacent buckled sublaminate [104]. Higher ply stresses than in a sound structure will therefore occur, the consequence being that a reduced failure load of the composite structure under compression will arise. A significant reduction of the global critical buckling load can occur. The strength and stiffness reduction can be linked to the initial buckling of the structure. Local buckling typically occurs when the delamination is large and close to the surface (thin sublaminate on one side), which allows one part of the structure to buckle locally; whereas the remaining structure (basic laminate/ thick sublaminate) does not buckle. For smaller delaminations located closer to the mid-surface global buckling predominantly occurs, wherein both sublaminates buckle towards the same side.

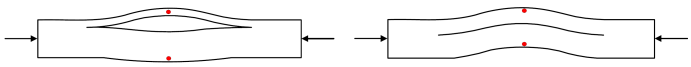

Figure A.1: Left: Local buckling mode (local cap opening); Right: Global buckling mode (full cap buckling); Figure from Paik et al. [90]. The red dots symbolise displacement evaluation points.

Under operation conditions wind turbine blades experience high aerodynamic loads, which lead to blade bending. The loading introduces compression on the suction side and tension on the pressure side of blades in normal operation. The loading-carrying structure providing the blade with sufficient strength and stiffness often consists of a main spar and shear webs integrated into the aerodynamic shell. Usually the main spar is made of fibre composite materials, where most of the fibres are oriented in longitudinal direction. Often glass fibres or glass and carbon fibre combinations embedded in epoxy resin matrices are used, providing the composite structure with a high strength-to-weight ratio.

Delaminations may be found within the main spar of the blade. Overgaard et al. [88, 89] e.g. investigated experimentally and numerically the structural collapse of a wind turbine blade and came to the conclusion that the structural collapse was caused by multiple local buckling-driven delamination processes. For an accurate assessment of detected delaminations based on size and location in wind turbine blades, guidelines and recommendations are needed.

In order to understand the effect of delamination under compression on lami-

nated composite materials several tests and studies have been conducted. Short et al. [104] tested small glass-fibre-reinforced plastic test specimens, ran Finite Element simulations and developed simple closed-form models for isotropic materials. They also created for flat and curved test specimens a delamination induced buckling mode map for varying delamination sizes and through thickness positions differentiating between local and global.

Studies on the behaviour of delaminations in rectangular composite panels with an initial delamination under compressive loading were carried out by Branner and Berring [19]. They compared experimental findings with a numerical parameter study. Branner and Berring created a buckling mode map for panels under in-plane compression similar to the load carrying flange in the main spar of a typical wind turbine blade. The study showed how the buckling mode shape depends on the size and on the location of the delamination through thickness.

Gaotti et al. [39] studied numerically the panel behaviour under uni-axial loading. They compared advanced numerical prediction methods with the simple models, where delaminations were modelled as disconnected finite element regions.

In all these studies the authors concluded that the panels under uni-axial in-plane loading experience a significantly reduced compressive strength in case of simply supported boundary conditions. Short et al. [104] also concluded that delaminations near the convex side lead to more significant strength reductions than delaminations near the concave side of the panel. Much work was done to address delaminations on component and panel level. However, due to the assumed boundary conditions used in the studies the authors were limited in drawing solid conclusions whether or not their results can be transferred to full scale wind turbine blade structures. Does a delamination in a main spar of a blade cause a similar strength reduction or does the surrounded structure compensate the local stiffness and strength loss up to a certain size of the delamination? A design criterion for how large and deep delaminations can be accepted without increasing the risk of blade collapse taking the surrounding structure into account is missing.

Such a criterion could help blade manufactures and turbine operators to decide whether a detected delamination can be accepted, needs to be repaired, or whether the blade must be scrapped.

The aim of this numerical study was to investigate how much the strength of a wind turbine rotor blade is affected by delaminations. Two different approaches were used to study the effect of delaminations, where one of the numerical approaches allowed interlaminar crack growth in order to achieve higher accuracy.

A.3 Methods

A.3.1 Modelling method

The DTU 10MW reference wind turbine blade was used as a basis for simulating the effect of delaminations. The blade, described in detail in [10], has a length of 86.4m and a root diameter of 5.4m. The load carrying structure of the blade is based on two caps and two shear webs. For the studies an 8.65m long section of the blade was used to investigate delamination behaviour under static load. The section represented the rotor blade in a distance from 41.65m to 50.3m from the root at radial position from 44.45m to 53.1m (see Figure A.2).

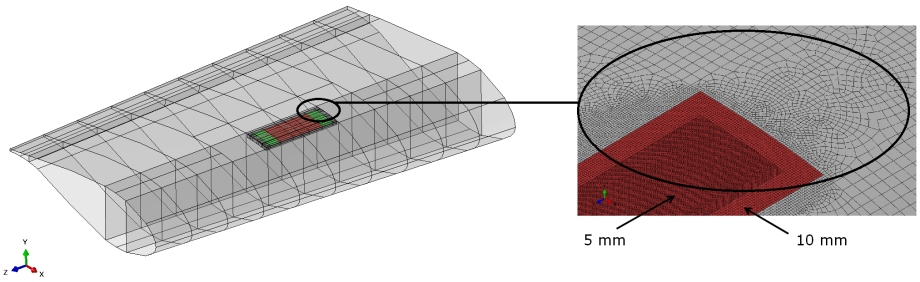

Figure A.2: Blade section shell model (grey) of the DTU 10MW Reference Wind Turbine including submodel (red). The submodel on the left picture is subdivided into two section cohesive zone I (red) and cohesive zone II (green).

The blade section was modelled with four node shell elements (Abaqus element type S4) in the commercial finite element software Abaqus/CAE 6.12-2. The outer surface of the blade was used as the reference surface containing the finite element nodes ("node offset option") (see Figure A.3). Apparent material properties were assumed to represent the multi-directional plies instead of a more detailed lay-up description. The entire layup and the material properties for the blade are available online: http://dtu-10mw-rwt.vindenergi.dtu.dk/ and can be accessed after free registration. In this paper only the apparent material properties of the unidirectional material used in the caps is given in Table A.1 to illustrate the properties of the region studied in detail. The critical energy release rate values were chosen according to typical magnitudes for unidirectional composite materials [106].

Further simplifications were made due to the shell modelling approach. The

trailing edge and the cap/web joints were modelled in a general way without specifying the geometrical details at the joints. The modelling strategy is shown in Figure A.3 for the shear web to cap joints and the trailing edge joint, where simple edge to edge joints were assumed.

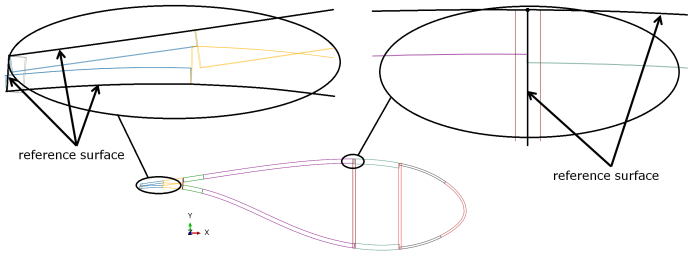

Figure A.3: Simplifications due to the shell modelling approach.

The shell model contains 60,999 four node shell elements. The typical elements in the model had a characteristic element length of 0.05m. Mesh refinement applied to shell elements around the area of interest, where an initial delamination was modelled, reduced the characteristic element length to 0.01m.

Table A.1: Apparent material properties of the unidirectional composite material. Young's modulus (E), Poission's ratio (ν)), density (ρ), shear modulus (G), critical energy release rate (G_c), mixed mode exponent (η), maximum traction (τ), stiffness of the interface(K), critical strain parameter (ϵ), safety factor (γ) [10, 106, 120]..

$\boldsymbol{E_{11}}$	$\boldsymbol{E_{22}}$	$\boldsymbol{E_{33}}$	$\boldsymbol{\nu_{12}}$	$\boldsymbol{\nu_{13}}$	$\boldsymbol{\eta}$
$41.63GPa$	$14.93GPa$	$13.43GPA$	0.2410	0.2675	3.8
$\boldsymbol{\nu_{23}}$	$\boldsymbol{\rho}$	$\boldsymbol{G_{12}}$	$\boldsymbol{G_{13}}$	$\boldsymbol{G_{23}}$	
0.3301	$1900kg/m^3$	$5.047GPa$	$5.047GPa$	$5.047GPa$	–
$\boldsymbol{G_{I_C}}$	$\boldsymbol{G_{II_C}}$	$\boldsymbol{G_{III_C}}$	$\boldsymbol{\gamma_F}$	$\boldsymbol{\gamma_{Ma}}$	
$200\ J/m^2$	$1000\ J/m^2$	$1000\ J/m^2$	2.205	1.35	–
$\boldsymbol{\tau_I}$	$\boldsymbol{\tau_{II}}$	$\boldsymbol{\tau_{III}}$	$\boldsymbol{\epsilon_1^T}$	$\boldsymbol{\epsilon_1^C}$	
$7.5MPa$	$15MPa$	$15MPa$	2.10 %	1.50%	
$\boldsymbol{K_{nn}}$	$\boldsymbol{K_{ss}}$	$\boldsymbol{K_{tt}}$	$\boldsymbol{\epsilon_1^T/\gamma_{Ma}}$	$\boldsymbol{\epsilon_1^C/\gamma_{Ma}}$	
$3e14N/m^3$	$1.15e14N/m^3$	$1.15e14N/m^3$	0.9523%	0.6802%	

The region surrounding the delamination was discretised using a fine mesh of

solid brick elements. In the following this region will be referred to as "submodel". The term should not be confuse with a technique of the same name, where a local part of a model is analysed based on interpolation of the solution from a coarser mesh. In our simulation the submodel was implemented in order to simulate buckling driven delamination growth in the cap. The submodel had a span of ca. 1.7m and was placed centrally in the cap (see Figure A.2). The width of the cap (B) varied between 0.707m and 0.725m. The thickness of the cap at this location was 0.0817m.

In order to investigate the behaviour of rotor blades with initial delaminations, rectangularly shaped delaminated areas were centrally positioned in the submodel. The initial delaminated areas varied in size and position through the thickness. The ratio t/T described the position through the thickness (see Figure A.4) with the total cap thickness T=0.0817m and the distance to the outer surface t. The length (a) and width (b) of the initially delaminated area were varied. For all simulations in this study the aspect ratio $a/b = 1.29$ was used. This aspect ratio was chosen to promote the formation of a single buckle at low loads. The minimum buckling load (critical buckling load = N_0) depends on both the elastic properties and the initial delamination size (a, b) and position (t).

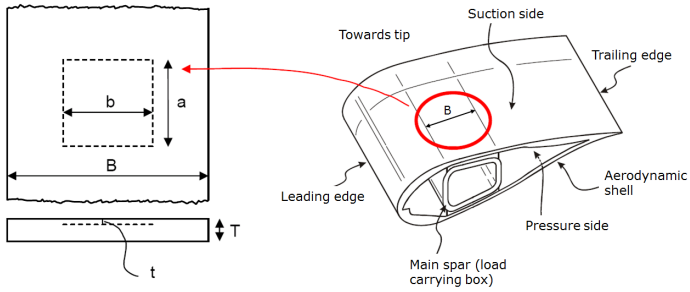

Figure A.4: Geometrical description of positioning the initial delaminated (taken from Sørensen et al. [108].

For the cap with the material properties given in Table A.1 the aspect ratio $a/b = 1.29$ can be derived for orthotropic panels subjected to uniaxial in-plane compression where all edges are simply supported [64, 19, 39]. The assumption leads to the following equation:

$$N_0(m,n) = \pi^2 \left[D_{11} \left[\frac{m}{a}\right]^2 + 2\left(D_{12} + 2D_{66}\right) \left[\frac{n}{b}\right]^2 + D_{22} \left[\frac{n}{b}\right]^4 \left[\frac{a}{m}\right]^2 \right] \quad \text{(A.1)}$$

where N_0 is the critical buckling load in terms of a force per length, D_{ij} are the elements of the bending-stiffness matrix from classical laminate theory which

relates bending and torsion moments with curvatures, and m and n are the numbers of buckle half wavelength in spanwise and transverse direction, respectively. Assuming $n = 1$ it can easily be shown that the critical buckling load N_0 is minimal if:

$$m = \frac{a}{b}\left[\frac{D_{22}}{D_{11}}\right]^{\frac{1}{4}} \tag{A.2}$$

Assuming m=1 in Equation A.2 yields $a/b = 1.29$. The aspect ratio is similar to the results Braner et al. presented in [104] with a/b = 1.31 .

The submodel is a highly discretised 3D model of the cap (see Figure A.2) consisting of incompatible mode eight-node brick elements (Abaqus element type: C3D8I) and 3D cohesive elements (Abaqus element type: COH3D8). The cohesive elements were placed in a $0.817mm$ $(= 1/100 \cdot T)$ thin layer. The cohesive elements provided the possibility of delamination growth whereas the initial delamination was modelled by a missing layer of elements corresponding to the size of the delaminated area. Contact constraints are used to prevent element interpenetration.

The submodel has two different mesh densities with an element length of 0.01m and 0.005m, respectively, in order to smoothen the transition between the coarser shell and the finer brick elements (see Figure A.2). The entire submodel consists of approximately 180,000 solid elements and 22,000 cohesive elements. The solid elements are equally distributed into seven layers through the thickness. The outer (rougher) and inner (finer) submodel element areas were tied together via so-called tie constraints (provided by Abaqus).

The submodel 3D brick elements were coupled with suitable constraint equations to the shell element edges of the basic model (shell-to-solid coupling provided by Abaqus).

A.3.1.1 Cohesive elements

Cohesive elements were chosen for modelling delamination growth because this method allows existing cracks to grow and also to initiate new cracks within the framework of Continuum Damage Mechanics (CDM) [120].

In general material damage considers crack initiation, crack growth and crack merging. CDM describes the state of damage with a damage variable (d). The variable ranges between d = 0 (no damage) and d = 1 (full damage). The material fails completely when the value d = 1 is reached. CDM can be described with the cohesive zone model (CZM) approach. Within the energy based CZM approach material properties, crack initiation conditions and a crack evolution functions are defined and can be visualised in a tension softening diagram.

A critical energy release rate defines the area under the traction-separation-

relation. Cohesive elements are used to model material discontinuities and damage based on Griffith´s energy approach [121, 38]. For the current work a bilinear traction-separation relation was chosen because of its simplicity [38].

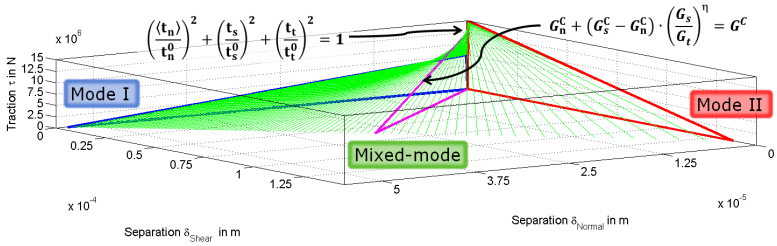

Figure A.5: Illustration of mixed-mode response in cohesive elements with Benzeggagh-Kenane fracture criterion (equation on the right hand side) and quadratic damage initiation interaction function (equation on the left hand side).

The energy release rate associated with delamination growth strongly depends on the fracture mode. The criteria for crack initiation and crack propagation have to take mode-mixity into account. Generally, three different modes of fractures are assumed and consequently also three traction-separations laws according to the different interfacial strength and maximum tractions have to be defined. The delamination growth process starts when the stresses and/or strains satisfy a damage initiation criterion. In the present work a quadratic nominal stress criterion was used to interpolate between these different traction-separation laws. The criterion assumes damage initiation when a quadratic interaction function reaches the value one (see Figure A.5).

The delamination evolution was defined by the Benzeggagh-Kenane (BK) fracture criterion [14], which considers the dependence of the fracture energy on the mode mixity. The BK criterion is particularly useful when the critical fracture energies for the second and third mode of fracture are the same, which is commonly assumed.

The BK fracture criterion is defined by the components of the energy release rate G_i and the critical energy release rate G_i^C (see Figure A.5). Further assumptions were that the delamination can only propagate in the interface between two plies. The interface was represented by the cohesive elements. Additionally, the delamination cannot jump between the plies during crack propagation because the model only contains one layer of cohesive elements [120, 80].

In numerical FEM analyses the calculation time is mainly determined by the number of degrees of freedom (DOF) of a model. Therefore, on the one hand the

mesh discretisation should be as coarse as possible. On the other hand often fine discretizations are needed to yield accurate results. Especially in areas, where stress concentrations are expected or energies have to be determined accurately. The latter is the case for the process zone of the cohesive layer where the crack propagation takes place. The length of the process zone is called cohesive zone length (l_{cz}). The cohesive zone length should contain at least three elements to calculate the energy release rate during the delamination growth precisely [21]. The length of the process zone can be estimated as:

$$l_{cz} = M * E * \frac{G_c}{(\overline{\tau}^0)^2} \quad with \;\; M = 1 \text{ (Hillerborg's model) [21]} \tag{A.3}$$

where M is a parameter depending on the adopted calculation model. The interfacial strength is expressed by $\overline{\tau}^0$, G_c is the critical energy rate and E the Young's modulus.

Typically, glass fibre epoxy or carbon fibre epoxy composite materials have a l_{cz} that is only a few millimetres long. Discretisation of the l_{cz} with at least three elements would require an element size of around a millimeter or smaller depending on the material. The calculation time to analyse large structures with such a high discretisation would cause problems and predictions for large scaled progressive delaminations would not be realised in reasonable time with current state of computational power.

An engineering solution for using coarser meshes was given by Turon et al. [121] by artificially lowering the interfacial strength. Lowering the interfacial strength ($\overline{\tau}^0$) increases the l_{cz}. As a consequence the length of each element (L_e) in the cohesive zone can be increased, which decreases the calculation time without having a strong influence on the accuracy:

$$N_e = \frac{l_{cz}}{L_e}. \tag{A.4}$$

According to Turon et al. [121] the required $\overline{\tau^0}$ for a desired L_e and N_e representing the l_{cz} can be calculated by

$$\overline{\tau}^0 = \sqrt{\frac{9 * \pi * E * G_c}{32 * N_e * L_e}}. \tag{A.5}$$

The reduction of $\overline{\tau^0}$ by e.g. a factor of 10 increases the length of the cohesive zone by a factor 100. Table A.1 shows the used material properties, where $\overline{\tau^0}$ was reduced by a factor of seven compared to a typical interfacial strength of glass fibre epoxy with $\overline{\tau}^0 = 53$ MPa.

In the numerical study the cohesive element layer was divided in two sections (cohesive zone I and cohesive zone II) as shown in Figure A.2. The partition

ensured that delamination growth always initiated around the initially delaminated area and avoided artificially induced delamination growth evoked by stress concentrations at the transition zones between the zones with different level of discretisation. Cohesive zone II describes the material properties of the first and last 0.1m in radial position of the cohesive elements which embody the transition to the coarser solid elements. Cohesive zone I specifies the material properties of the remaining cohesive elements. The critical energy release rate between cohesive zone II were increased by a factor of ten compared to the values for cohesive zone I given in Table A.1 in order to ensure delamination growth starting around the initial delaminated area and not at areas with artificially high stresses and strains due to mesh refinement.

A.3.1.2 Numerical analysis and boundary conditions

In order to simulate delamination growth moments dominated by flapwise bending, comparable to those blade structures experience under normal operation conditions, were applied. All nodes representing the back section (the section closest to the root) were fully constrained. The nodes representing the front section were coupled to a reference node using a so-called kinematic coupling constraint (see Figure A.6). This forces the front section to move like a rigid body. Three moments were applied to the references node at the front section: $M_x = -16.4e6Nm$, $M_y = 2.4e6Nm=$ and $M_z = 0.32e6Nm$. The moments correspond to approximately 100% of the moments of the design loads evaluated for the blade cross section at $r = 48.775m$ (middle of the simulated blade section).

Experimental investigations on the compressive strength of thick composite panels have shown that the loading has to be high before delaminations located close to the centre of the panels propagate [19]. In order to ensure delamination growth for all simulated cases, the applied moment was scaled up to 200% of the design load including the safety factor of 1.35. 100% of the load applied to the sound blade section leads to maximum and minimum strain values of around 0.6% at a load level of 100% of the design load. At a load level between 125% (compression) to 145% (tension) the design strain values (see Table A.1) are reached.

The numerical study is based on a quasi-static nonlinear analysis implemented in Abaqus/Explicit. The Abaqus/Explicit solver employs an explicit time integration scheme [27]. The explicit solver was chosen due to its efficiency when analysing large models and because it is really suited for models which exhibit a softening response (cohesive elements), and contact. No mass scaling was used. In order to simulate a quasi-static loading process the loading speed was kept so low that the kinematic energy of the system was very small compared to the internal energy of the structure ensuring that inertia forces were insignificant.

Two different modelling approaches were conducted. One approach only included solid elements in the submodel, but no cohesive elements, and therefore did not allow delamination growth. This approach is referred to as "solid element approach" in the following.

Cohesive elements were used for the second modelling strategy. This approach allowed delamination growth around the initial delamination. The delamination growth was limited to the area of the cohesive elements. The approach is referred to as the "cohesive element approach" in the following.

Three different initial delamination sizes (variation of b/B) placed at different thicknesses (t/T) in the laminate were studied. The width took the values b/B=0.278, b/B=0.4 and b/B=0.5. The delaminations were placed in thicknesses of t/T=0.05 up to t/T=0.35, divided in steps of $\Delta t/T = 0.05$.

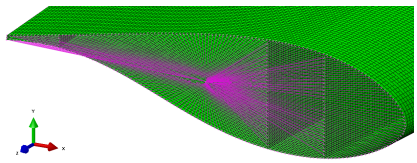

Figure A.6: Boundary condition at the front end of the blade section.

A.4 Results

A shell model including the implemented submodel without delamination was validated against the original blade shell model without submodel. No significant differences between both models were found. Also the stresses and strains at the interface from the shell to solid elements showed smooth transition. The submodel approach has therefore been found reliable and suitable.

The local occurring buckling modes in the main spar were divided into two different groups *full cap buckling* and *local cap opening*. The out-of-plane displacement of the central nodes of the sublaminates (see Figure A.1) were used to distinguish between the local cap opening and full cap buckling. The full cap buckling is comparable to global buckling on panel level. It is characterized by both nodes following the same path [90]. The sublaminates on both sides of the delamination move in the same out-of-plane direction, which usually leads to delamination gap closing. The local cap opening buckling mode is comparable to local buckling on panel level. The central nodes of the sublaminates move in opposite out-of-plane directions and cause an opening of the delamination [90].

Furthermore stable and unstable delamination growth was observed. For delaminations close to the surface stable delamination growth was observed. Stable delamination growth is characterised by gradual crack propagation and a slow increase of dissipated energy, respectively. Increasing loading is required in order to have crack propagation under stable crack growth conditions. Unstable/sudden delamination growth is characterized by progressive crack propagation without or with only very little additional loading. The delamination grows significantly faster and partly independent from additional external energy. Unstable delamination growth occurred for delaminations located deeper inside the caps.

A.4.1 Local cap opening buckling mode with stable crack growth

For local cap opening modes with stable delamination growth the solid and the cohesive element approach showed good agreement regarding buckling onset such as the one example shown in Figure A.7(a). At a load level of approximately 50% the upper sublaminate buckled whereas the basic laminate (lower sublaminate) remained undeformed. The delamination led to a local cap opening buckling mode. Simultaneously with the opening of the initial delamination, the delamination started to grow. The delamination propagation originated from the initial delaminated area and grew circularly around it (see Figure A.8(a) to Figure A.9(b)). This phenomenon was indicated by the dissipated energy and the damage stage of the cohesive elements. At a load level of approximately 135% the out-of-plane displacement of the upper sublaminate (cohesive element approach) shows a small kink. This kink can be explained with changes in the buckling mode shape. The sine-shaped buckling mode with a single local cap opening buckle was moving towards another buckling mode configuration with three buckles (see Figure A.10).

At low load levels both modelling approaches showed small reductions in the bending stiffness caused by the Brazier effect [20] (see Figure A.7(b)). The bending stiffness was determined by dividing the applied bending moment by the strain at the center of the cap on the pressure side in longitudinal direction. At a load level of approximately 50% buckling occurred and delamination growth started, which caused a progressive decrease of the bending stiffness for the cohesive element approach. No significant changes in the bending stiffness due to the buckling could be observed for the solid element approach at this load level.

The next significant decrease happened at a loading of around 135% for the cohesive element approach. The decrease of the bending stiffness was accompanied by the change in the buckling mode shape, which showed progressive decrease. A small increase of the bending stiffness due to contact between the upper and

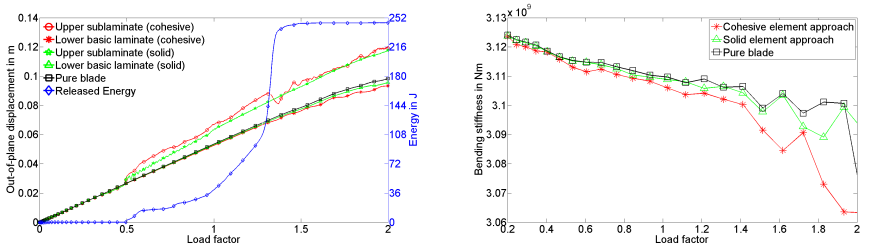

(a) (b)

Figure A.7: (a) Local cap opening buckling mode with stable crack growth (t/T=7.5%, b/B=0.40). The figure shows the out-of-plane displacement of the central points and the released energy as a function of the load. (b) Bending stiffness plot of the entire blade section evaluated at the pressure side in the middle to the cap.

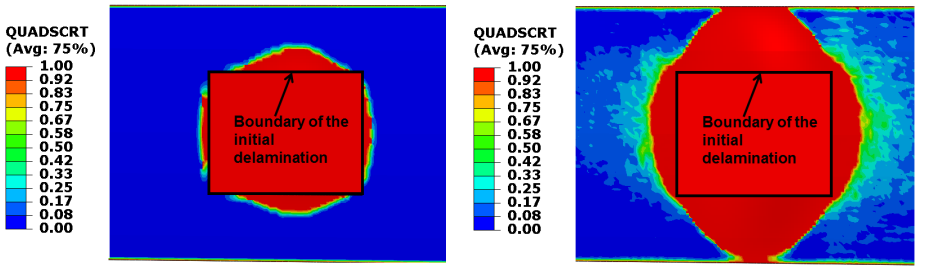

(a) (b)

Figure A.8: The figures show the progressive damage initiation of the cohesive elements around the initial delamination (white square) for local cap opening buckling mode with stable crack growth (t/T=7.5%, b/B=0.40) for different load levels. The variable ranges between d = 0 (no damage) and d = 1 (full damage).

lower sublaminate at a load level around 175% occurred. First at load levels of more than 160% the solid element approach showed an progressive decrease in the bending stiffness. However, the blade bending stiffness only slightly decreased in the overall performance with less than 1% for both approaches for loads up to the design load and up to 2% for a load factor of 2.

During the buckling of the sublaminate high stresses and strains in the upper

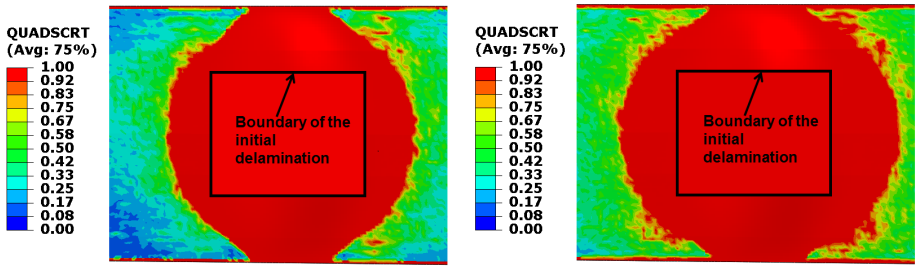

(a) (b)

Figure A.9: The figures show the progressive damage initiation of the cohesive elements around the initial delamination (white square) for local cap opening buckling mode with stable crack growth (t/T=7.5%, b/B=0.40) for different load levels. The variable ranges between d = 0 (no damage) and d = 1 (full damage).

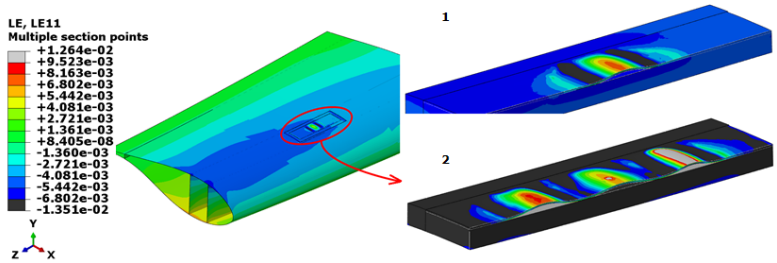

Figure A.10: Local cap opening buckling mode with stable crack growth (t/T=7.5%, b/B=0.40). The strain in longitudinal direction is plotted. The color bar indicates the design strain values of the longitudinal tensile strain (0.9523%) and compressive strain (-0.6802%) to failure. The sine-shaped local cap opening buckling mode with a single buckle at 100% loading (Picture 1.) moved towards another buckling mode configuration. Picture 2 represents the buckling mode shape at a load level of 150%.

sublaminate occurred. In Figure A.11 the longitudinal normal strain of the blade section with a cap opening buckling mode is plotted at a loading of 80%. The colour bar for the design strain values for the unidirectional material used in the main spar ranges from red (tensile design strain, ϵ_1^T/γ_{Ma}=0.9523%) to blue (compressive design strain, ϵ_1^C/γ_{Ma}=-0.6802%). The black colour indicates areas where the compressive design strain value is exceeded. The figure shows

that the cap opening buckling mode causes stress concentrations and that the compressive strain around the initial delamination in the upper sublaminate exceeds the compressive strain design value (ϵ_1^C/γ_{Ma}) by more than 40%. The local cap opening buckling modes with stable delamination growth caused less than 1% decrease of the bending stiffness at the design load level but caused high strains and stresses in the surrounding of the delamination. This high strains and stresses in the upper sublaminate were close to and partly even above the material design properties and could easily have led to material failure.

For all simulated delaminations that caused local cap opening buckling with stable delamination growth the critical buckling load, when delamination propagation started, was below the maximum design load. The local cap opening buckling modes led to a bending stiffness reduction of less than 1% for loads lower than the design load. The fact that the delamination grew already at these load levels raises awareness of how critical delaminations can be.

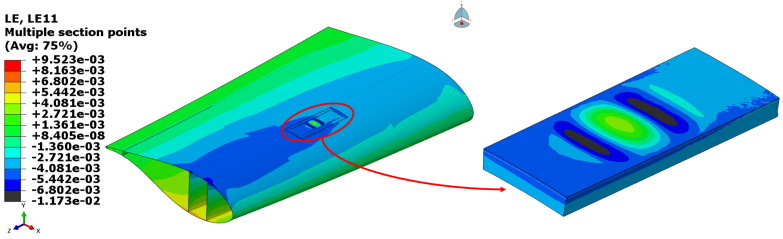

Figure A.11: Local cap opening buckling mode with stable crack growth (t/T=10%, b/B=0.50). The strain in longitudinal direction under 80% of the design load is plotted. The color bar indicates the design strain values of the longitudinal tensile strain (0.9523%) and compressive strain (0.6802%) to failure.

A.4.2 Local cap opening buckling with sudden/unstable crack growth

The differences between the simulations based on the solid element approach and simulation based on the cohesive elements approach became apparent for local cap opening buckling modes with sudden/unstable crack growth. The models with cohesive elements showed local cap opening up to a thickness ratio of t/T=0.25, whereas models with solid elements had already shown a delamination closing and tended towards full cap buckling behaviour at that thickness ratio (see Figure A.12(a)).

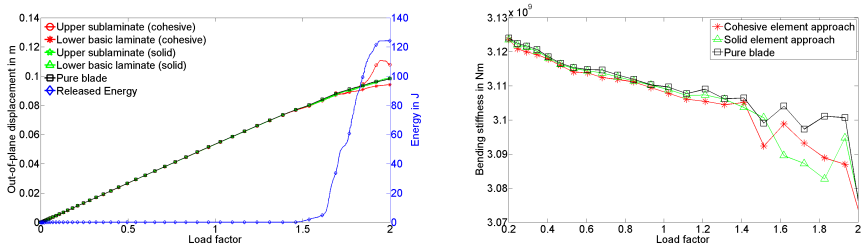

(a) (b)

Figure A.12: (a) Local cap opening buckling mode and cap closing buckling mode with sudden/unstable crack growth (t/T=25%, b/B=0.50). The figure shows the out-of-plane displacement of the central points and the released energy as a function of the load. (b) Bending stiffness plot of the entire blade section evaluated at the pressure side in the middle to the cap. The bending stiffness reduces after passing the design load (load factor=1).

The graphs representing the solid model without delamination growth possibility (solid element approach) showed delamination gap closing/full cap buckling at high loads. The initial delamination size to depth ratio prevented the solid model from local cap opening buckling. While delamination growth for initial delaminations close to the surface (low t/T ratio) were driven by buckling at low loads and with stable delamination propagation, the opposite was the case for deeper placed initial delaminations. For delaminations deeper inside the main spar, the thicker sublaminates were less flexible and could withstand higher loads before buckling onset. For simulations based on the cohesive element approach delamination growth occurred due to the high stresses and strains before cap opening buckling occurred. The delamination propagation operated like a splitting of the load carrying main spar and extended the area of the initial delamination. Delamination-driven buckling occurred. For initial delaminations placed at t/T$\geq$0.15 the buckling first occurred at load levels significantly above the maximum design load level(>125% loading) and with prior delamination growth as shown in Table A.2. Before reaching these high load levels the blade section had already exceeded the design strain values in the main spar as shown on the sound blade structure in Figure A.13.

For the cohesive element approach a clear reduction of the bending stiffness first occurred when the delamination started to grow (see Figure A.12(b)). Before the delamination growth started the reduction of the bending stiffness was mainly caused by the Brazier effect [20]. The cohesive element approach predicted the bending stiffness degradation at an earlier stage due the delamination

growth and thus an increase of the delamination. At a certain load level the delamination started to grow in size and consequently the delaminated area got large enough to cause local cap opening buckling at the given load level. In cases where simulations based on the solid element approach predicted full cap buckling behaviour/delamination closing, it can be concluded that the size of the initial delamination was too small and too deep through the thickness to cause local cap opening. However, the maximum bending stiffness reduction for both approaches was less than 1.5%.

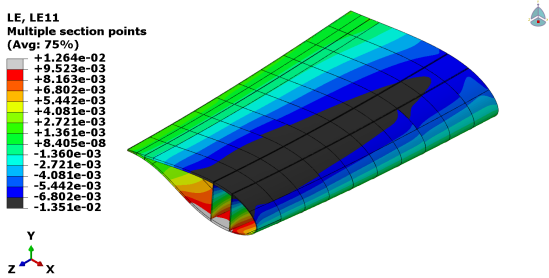

Figure A.13: Strain distribution in the sound blade structure at a load level of around 146% of the designated load.

A.4.3 Full cap buckling

Full cap buckling modes occurred for both simulation approaches when the initial delamination was positioned deep inside the structure. The blade model with cohesive elements showed blade collapse on lower load levels than the model based on the solid element approach due to a significant reduction in the bending stiffness caused by delamination growth. Typical observed full cap buckling behaviour responses looked like the one example shown in Figure A.14(a). In all simulated cases, where full cap buckling had been observed, the load level was higher than 140% of the design load before a significant bending stiffness reduction could be observed. By exceeding this load level high stress and strain levels were also obtained. These high stresses and strains exceeded the design strain values but were still below the critical material strain values when critical buckling loads were reached as shown in Figure A.13. For models based on the cohesive element approach delamination growth always had occurred before full cap buckling occurred. The simulations showed clear differences between both approaches regarding the bending stiffness reduction. The cohesive element approach clearly predicted more conservative results with bigger losses in the bending stiffness than the solid element approach. The bending stiffness degra-

Table A.2: Results of the delamination study, width ratio (b/B), delamination placed in through cap thickness ratio (t/T), local cap opening buckling load (P_{open}), buckling mode shape, delamination growth onset as a factor of the design load.

b/B	t/T	P_{open}coh.	P_{open}solid	Buckling mode	Del. onset
0.278	0.05	0.53	0.54	Local cap opening	0.53
0.278	0.075	1.08	1.11	Local cap opening	1.08
0.278	0.010	1.55	1.59	Local cap opening	1.55
0.278	0.015	1.84	-	Local cap opening	1.60
0.278	0.020	1.90	-	Local cap opening	1.60
0.278	0.025	1.90	-	Local cap opening	1.60
0.278	0.030	-	-	Cap closing	1.60
0.40	0.05	0.24	0.24	Local cap opening	0.34
0.40	0.075	0.50	0.50	Local cap opening	0.50
0.40	0.010	0.80	0.80	Local cap opening	0.80
0.40	0.015	1.50	1.50	Local cap opening	1.42
0.40	0.020	1.64	-	Local cap opening	1.53
0.40	0.025	1.83	-	Local cap opening	1.53
0.40	0.030	-	-	Cap closing	1.53
0.50	0.010	0.60	0.59	Local cap opening	0.60
0.50	0.015	1.26	1.25	Local cap opening	1.25
0.50	0.020	1.53	1.65	Local cap opening	1.38
0.50	0.025	1.75	-	Local cap opening	1.42
0.50	0.030	-	-	Cap closing	1.42

dation for the cohesive element approach happened on lower load levels. The extension of the delaminated area during delamination growth process led to the earlier bending stiffness reduction. The alternation of the bending stiffness starting around a load level of 130% resulted from the contact during the gliding between the upper and lower delaminated sublaminates during the buckling process. However, the maximum bending stiffness reduction was less than 1% for loads up to the design load.

All buckling modes that occurred during the study are summarised in Figure A.15 and Table A.2. The modes, as described above, were divided into different buckling modes, local cap opening buckling mode and full cap buckling mode. In the figure the buckling modes are plotted with their initial delamination width b/B over the position through the cap thickness t/T. For each configuration both modelling approaches were adopted and compared.

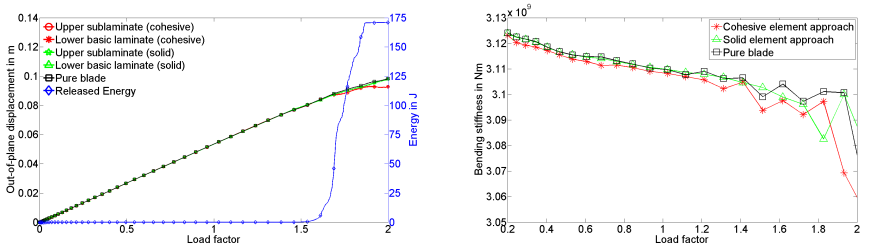

(a) (b)

Figure A.14: (a) Full cap opening buckling mode with sudden/unstable delamination growth (t/T=30%, b/B=0.40). The figure shows the out-of-plane displacement of the central points and the released energy as a function of the load. (b) Bending stiffness plot of the entire blade section evaluated at the pressure side in the middle to the cap.

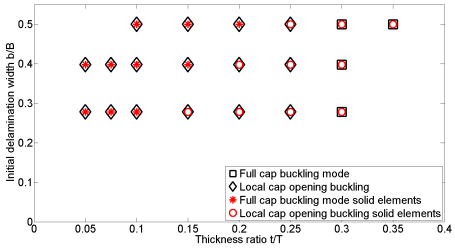

Figure A.15: Buckling mode map for the cap section with an initial delamination aspect ratio a/b=1.29.

A.4.4 Blade vs. panel studies

The buckling mode map (Figure A.15) clearly shows that the bigger the initial delamination was in size the bigger the tendency for local cap opening buckling modes. This tendency is compliant with the observation of panel experiments and simulations conducted by Branner and Berring [19].

However, differences arose when comparing the Branner and Berring's residual strength map for simply supported composite panels with imbedded delaminations published in [19] with the results of the current blade study. Branner and Berring's residual strength map shows for delaminations with a size of b/B=0.3 and a through thickness positioning ratio between $0 < t/T < 0.5$ no or less than

5% reduction of the compressive strength for the load carrying capacity of the panels. Comparing these results with the present blade study similar results were found if the design load (load factor of 1) is considered to be the maximum load the blade has to withstand.

Looking at delaminations with a size of b/B=0.5 and a through thickness positioning ratio between $0 < t/T < 0.5$, Branner and Berring predicted a compressive strength reduction between 5% and 15% of its load carrying capacity. Only very little reductions of the bending stiffness of less than 1.0% for loads up to the maximum design load (load factor of 1) could be noticed in the blade study.

The delaminations in the main spar of the blade under quasi-static loading did not cause the same bending stiffness reduction as strength reductions observed in the panel experiments and simulations conducted by Branner and Berring [19]. Reflecting the results from the blade study, the results make sense anyway. Considering 60% of the blade flapwise bending stiffness is provided by the caps, each cap provides 30% of the flapwise bending stiffness. If the upper 10% of the bending stiffness over the complete cap width B would be removed and would not contribute at all to the overall blade bending stiffness, the bending stiffness would be reduced by maximum 3%.

It seems that differences in boundary conditions (the main spar as part of the entire blade vs. simply supported panel) were essential. It looked as if the local stiffness bending and strength reduction caused by the delamination (for the here simulated cases) in the blade could be compensated by the surrounded blade structure. The main spar as an integrated part of the entire blade structure cannot twist, rotate and strain freely as the panel can. The panels in Branner's study were the more flexibly supported at the panel edges and thus tended to buckle earlier than the spar in the present blade study. Furthermore, the laminated caps in the blade only provide a share to the overall flapwise bending stiffness. Other effects like the distance between the caps, the shear webs and the aerodynamic shell also have a significant contribution to the overall blade bending stiffness, which was neglected in the panel study.

A.5 Discussion and conclusion

The study showed that modelling buckling driven delamination in wind turbine blades is feasible. The highly discretised sub-modelling approach where a subset of brick elements was connected to a shell element model via suitable couplings constraints, made it possible to predict the effect of delaminations on wind turbine blade structures. Two different subset modelling approaches were applied. One approach was purely based on solid elements and the other included the possibility to simulate delamination growth based on the implementation of

cohesive elements.

The cohesive element approach was more comprehensive and provided, due to the possibility of delamination growth simulation, good insights of the delamination process and buckling behaviour. The implementation of cohesive elements was clearly the superior approach compared to the solid element approach because additional information such as the load level for delamination growth onset/ propagation could be extracted. Thus, the cohesive element approach made it easier and more precise to evaluate the critical delamination size. The cohesive element approach was the more conservative approach due to the consideration of delamination propagation and its effect on the blade structure.

Beside the different numerical approaches the effect of the delamination on the blade section was studied. The study showed that blade structures with initial delaminations with a width between 30-50% of the cap width positioned close to the surface started to grow in load ranges of normal operation conditions and led to local cap opening buckling modes. The local cap opening buckling modes with stable delamination growth (with numerical limitation of maximum delamination growth) caused only little bending stiffness reductions of less than 1.5% compared to the sound structure. Nevertheless, the near-surface local cap buckling modes led to high strains and stresses in the surrounding of the delamination. Therefore, near-surface delamination has to be considered to be critical.

The study showed how critical near-surface delamination in wind turbine blades under design load conditions can be even though only quasi-static loading was applied, the delamination growth was limited in size due to the modelling approach and no ply failure criteria has been considered. In the simulations the delamination growth started at loads of around 50% of the design load. In reality already this normal operation load for local near-surface delaminations would probably be high enough to cause delamination growth due to cyclic loading. At a certain size of the delaminated area and at a corresponding load level local cap opening would occur. High stresses and strains in the sublaminate around the delamination induced by local cap opening would be the consequence. The highly stressed and strained plies would probably be reduced in their life-time and fatigue failure would occur. Consequently, the adjacent plies have to compensate for the failed plies and would be loaded higher, too. This process would continue until ultimate failure occurs.

Full cap buckling for the here tested blade and delamination configurations did not have any significant effect on the blade response under normal operation conditions. In the simulations the static load exceeded the design load by more than 40% before delamination growth onset or buckling occurred.

The conclusion based on the study is that the load threshold of delamination propagation is highly depending on the location and size of the initial delam-

ination. Delamination induced local cap opening buckling modes have to be considered to be more critical due to an earlier onset of local cap opening buckling compared to full cap buckling modes. This finding is in good agreement with the finding described in Overgaard et al. [89] that moderately sized initial and near-surface delamination will reduce the critical load significantly.

With the hereby presented study the authors came a little closer to the goal of getting to a design criterion for improved and more reliable prediction of delamination induced failure in wind turbine blades.

Interesting future studies would be to investigate how big and in which distance to the outer surface delaminations have to be to become critical and how local delaminations behave under dynamic load conditions.

A.6 Acknowledgement

The research paper is based upon work supported by the new Danish Centre for Composite Structures and Materials for Wind Turbines (DCCSM), grant no. 09-067212 from the Danish Strategic Research Council. The financial support is greatly appreciated.

Paper B

A comprehensive investigation of trailing edge damage in a wind turbine rotor blade

Article status: Accepted for publication on the 22^{nd} of November 2015.

Article title: *A comprehensive investigation of trailing edge damage in a wind turbine rotor blade*

Authors: P.U. Haselbach, M.A. Eder and F. Belloni

Journal title: Wind Energy

DOI information: 10.1002/we.1956

B.1 Abstract

Wind turbine rotor blades are sophisticated, multipart, lightweight structures whose aeroelasticity driven geometrical complexity and high strength-to-mass utilisation lend themselves to the application of glass- or carbon-fibre composite materials. Most manufacturing techniques involve separate production of the multi-material subcomponents of which a blade is comprised and which are commonly joined through adhesives. Adhesive joints are known to represent a weak link in the structural integrity of blades where particularly the trailing edge joint is notorious for its susceptibility to damage. Empiricism tells that adhesive joints in blades often do not fulfil their expected lifetime, leading to considerable expenses due to repair or blade replacement. Owing to the complicated structural behaviour – in conjunction with the complex loading situation – literature about the root causes for adhesive joint failure in blades is scarce. This article presents a comprehensive numerical investigation of energy release rates at the tip of a transversely oriented crack in the trailing edge of a 34 m long blade for a 1.5 MW wind turbine. First, results of a non-linear finite element analysis of a 3D blade model, compared with experimental data of a blade test conducted at DTU Wind Energy, showed to be in good agreement. Subsequently, the effects of geometrical non-linear cross-section deformation and trailing-edge wave formation on the energy release rates were investigated based on realistic aeroelastic load simulations. The paper concludes with a discussion about critical loading directions that trigger two different non-linear deformation mechanisms and their potential impact on adhesive trailing-edge joint failure.

B.2 Introduction

Wind turbine rotor blades are sophisticated multipart, multi-material, lightweight structures. The aeroelastic optimisation of the lift-generating surfaces that maximise power production leads to complex curved, asymmetric geometries which involve taper, twist and curvature. The use of glass- or carbon-fibre composite materials for blades lends itself due to shape manufacturability and their desirable high-strength-to-low-mass ratios. Most manufacturing techniques involve the separate production of the many subcomponents of which a blade is comprised and which are fittingly connected via adhesive joints

Empirical evidence presented by Ataya and Ahmed [7] show that exactly those adhesive joints present a weak link in the structural integrity of blades, where particularly the trailing edge joint is notorious for its susceptibility to damage. Adhesive joints which do not fulfil their expected lifetime result in considerable cost expenses due to downtime, repair and – even worse – blade replacement.

According to a study from the *National Renewable Energy Laboratory* (NREL) published in a report by Sheng [101], the contribution of rotor issues to the total downtime of a wind turbine ranges between 8 % and 20 %.

Just recently it was announced in an article by Wittrup [124] that all rotor blades in the Horns Rev2 wind park in Denmark are about to be replaced. The observed damage types of the rotor blades covered a wide range of failure types. Many of the observed damages concerned leading and trailing edge issues. Consequently, research on structural problems that may improve blade designs and hence increase lifetime offers a great cost saving potential for blade manufacturers as well as operators. However, literature dedicated to adhesive joint failure in wind turbine rotor blades is scarce. One of the underlying reasons is that the interplay of the various structural effects lead to inherently complex structural behaviour.

In blades, the cross-section warping deformations are associated with different modal *Strain Energy Release Rates* (SERRs). Such deformations are caused by both linear and non-linear effects. It appears that in blades, linear effects on SERRs are largely due to out-of-plane warping. The latter is mainly caused by shear and torsion, both of which induce Mode-III SERRs as discussed in [33]. Geometrical effects such as taper add to the problem by altering the shear flow distribution and therefore affect the Mode-III SERRs. In addition, the use of materials with different Poisson's ratios between subcomponents can induce linear effects owing to the additional fracture modes struggle to deform at different rates.

Regarding the non-linear effects, note that wind turbine blades are beam-type structures with thin-walled cross sections made from orthotropic materials. Using composite materials allows blades to undergo tip deformations of up to 20 % of their span. These large deflections, in conjunction with high out-of-plane and low in-plane cross-section stiffness, lead to geometric non-linear in-plane cross-section deformations. This bending-induced in-plane warping effect – also referred to as *Brazier effect* or *cross-section ovalisation* as investigated for blades by Damkilde and Lund [26] as well as Cecchini and Weaver [23] – is typically associated with Mode-I and Mode-II SERRs as discussed in [102, 31, 32]. The formation of geometrically non-linear lengthwise wave deformation patterns in the trailing edge increases the severity. In this case the SERR magnitudes increase exponentially, leading to unstable crack growth as discussed in [30].

Rotor blade trailing edges are very sensitive to stability effects like e.g. local buckling or fibre kinking, which are usually caused by geometrical imperfections. Small manufacturing deviations with respect to the trailing edge shape or the fibre alignment can effect the structure significantly. Also the load carrying capacity of wind turbine rotor blades is highly depending on the load direction and magnitude. While rotor blades can deal with high flapwise bending moments, load direction exposing the trailing edge to compressive stresses with

lower magnitudes can lead to trailing edge buckling and failure.

Figure B.1 shows an overview of a cause and effect analysis of trailing edge failure based on a system engineering framework to the structural integrity concept presented by Hoeppner [56]. The *holistic structural integrity process* (HOLSIP) is based on the fundamental idea that failure modes or mechanisms are interconnected and considers all fracture mechanisms for monotonic loading with consideration of the intrinsic nature of solids [56]. Beside the here presented interaction of different failure modes, external conditions like as e.g. temperature, chemical environments, humidity and radiation are not listed but affecting the trailing edge reliability, too.

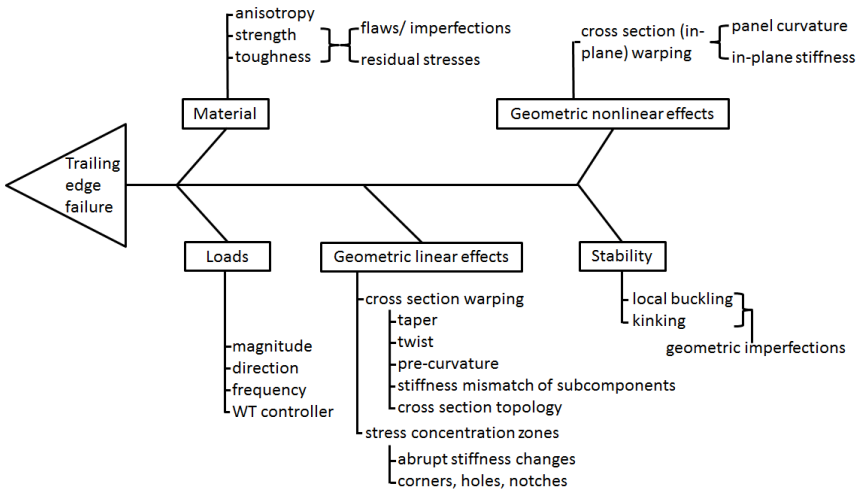

Figure B.1: Cause and effect analysis of trailing edge failure.

This paper aims at a comprehensive approach by simultaneously considering the aforementioned linear and non-linear effects and their interplay implicitly in the model and the test structure. The conducted work could serve as a basis for a holistic structural integrity process of trailing edge failure. This investigation sheds light on both the SERRs and mode mixity of a crack in the trailing-edge joint of a 34 m long blade for a 1.5 MW wind turbine. The introduced crack represents a flaw that runs along the internal fillet edge of the adhesive. It is beyond the scope of this paper to perform crack growth analysis. Instead the crack in the adhesive served as an indicator and was used to study the prevailing fracture modes as functions of the load magnitude and its direction.

Initial experimental results of a four-point loading blade test conducted at DTU

Wind Energy are presented. The measurement methodology aimed at the detection of a wave as it formed in the trailing edge and which eventually led to brittle debonding of the trailing-edge joint. Subsequently, aeroelastic simulation results are used to create a realistic load envelope which serves to benchmark the loads applied during the experiment. A detailed, numerical 3D model of the blade is first validated against the test data and subsequently used to investigate SERRs in the trailing edge for the aeroelastic load envelope. The paper concludes with a discussion of critical loading directions and their associated SERRs, as caused by cross-section deformation and geometrically non-linear wave formation.

B.3 Methods

B.3.1 Experimental setup

The tested wind-turbine rotor blade with an original length of 34 m was truncated at 29.5 m to accommodate it in the blade-testing facility at DTU Wind Energy. The root of the blade was bolted to a reaction frame at a pitch angle of 120° as shown in Figure B.2(a), which refers to a bending moment angle of 210° (Section B.3.5). Figure B.2(b) shows that the blade was loaded at four loading points (LPs) by means of carbon steel anchor plates (approx. $0.4\,\mathrm{m} \times 0.4\,\mathrm{m} \times 0.015\,\mathrm{m}$). Steel wires were attached to the carbon steel anchor plates, which were adhesively connected underneath the suction side cap. Additional, blind bolts were used to reinforce the connection. The loads were applied by pulleys in connection with displacement-controlled winches that pulled the blade towards the floor. The forces in the loading points could be measured by interconnected load cells as shown in Figure B.2 a).

The loading procedure of the blade is a non-linear problem. During the loading process, individual LPs unload due to structural coupling effects thereby rendering a multiple-point loading scheme uncertain with regard to meeting repeatability and accuracy demands. The loads were therefore applied at a quasistatic rate of $\leq 0.1\,\mathrm{m\,min^{-1}}$ in an iterative procedure until a convergence threshold was reached for every LP. The convergence threshold was defined as 2 % relative error between the measured force and the target load. During this iterative procedure, every LP starting with LP1 was brought up to the target load individually and irrespective of the response of the inactive LPs. This procedure was repeated in so-called loops until the convergence threshold was satisfied in all individual LPs at every load step. Typically, 15 to 20 loops per load step were needed to satisfy the convergence threshold in all four LPs. Table B.1 gives the individual loads normalised with LP1 (tip) for different key load steps where the load ratios between the LPs are constant.

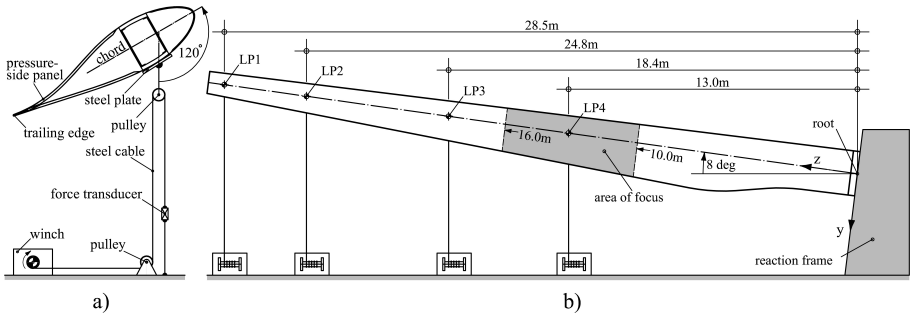

Figure B.2: a) Cross section with pulley system and force transducer, b) Elevation of test setup with LP positions and area of measurement focus.

Table B.1: Normalised target loads at LPs for specific key load steps as will be referred to in subsequent sections.

Load step	LP1	LP2	LP3	LP4
57 %	0.57	0.53	0.44	0.44
67 %	0.67	0.63	0.52	0.52
76 %	0.76	0.71	0.59	0.59
90 % (MDL)	0.90	0.84	0.70	0.70
100 % (Ultimate)	1.00	0.94	0.78	0.78

B.3.2 Conventional sensors

Quasi-vertical displacements of the blade were measured with *ASM Posiwire 6250* draw wire transducers and will be referred to as ASMs in this paper. Four ASMs were mounted on the strong floor with the draw wires attached to the suction-side cap at 10.0 m, 16.0 m, 22.0 m and 29.0 m. Two additional ASMs were directly attached to the trailing edge at 13.0 m and 16.0 m to validate the optical displacement measurements described in Subsection B.3.4. Electrical resistance strain gauges were used to validate longitudinal strains in the vicinity of the fibre sensors discussed later in Subsection B.4.2. These complementary strain gauges were glued directly on to the laminate after gelcoat removal and surface preparation.

B.3.3 Fibre sensors

Commercial fibre-sensing equipment from *HBM FiberSensing* was used to measure both longitudinal and transverse surface strains along the adhesive trailing-edge joint. The sensors were directly glued on the laminate after the gelcoat was ground off and the surface degreased and cleaned. The convention for the measurement direction *longitudinal* and *transverse* is stipulated in Figure B.3 (a). The measurement principle is based on Bragg reflection as explained in Hill [53], Kersey [67], Morey [83] and Kashyap [65]. *Fibre Bragg Grating* (FBG) sensors are introduced into an optical fibre along a gauge length of approx. 4 mm at customised spacings. Each FBG sensor represents a crystallographic plane which reflects a specific wavelength of the light spectrum travelling through the fibre and appears as a specific power output peak. Any elongation or contraction of the sensor causes a phase shift of the reflected wave which is proportional to the change of strain in the sensor. The strain measurable bandwidth is an inverse function of the amount of sensors in a fibre line. In the adopted configuration a band width (of 2.9nm which is) equal to $\pm$ 2400 μm/m was considered a proper compromise in order to have 10 sensors per fibre line. Examples of fibre applications for wind turbine rotor blades appear in Schroeder [98] and Fattahi [36].

The sensor setup was designed to measure the wave formation in the trailing edge even at low load levels through the variation of longitudinal bending strains along the wave. For this purpose a coarse sensor array with sensors spaced every 0.4 m was used to measure longitudinal strains on the pressure side between 10.0 m and 23.6 m. A refined sensor array with sensors spaced every 0.15 m was applied on the pressure side in the designated failure area between 10.0 m and 16.0 m. Transverse strains were measured on the pressure-side and the suction-side shell at 0.15 m intervals adjacent to the longitudinal sensors in the designated failure area. The sensor scheme of all measurement lines with a total of 160 sensors is shown in Figure B.3 (a), whereas the location of the sensors relative to one another in respect to the trailing edge appears in Figure B.3 (b).

All sensors were connected to two spectrometers (*BraggMeters*) with a laser-wavelength range between λ =1500 nm and λ =1600 nm. Each fibre contained 10 sensors with a measurement wave-length range of $\Delta\lambda = \pm 5$ nm which gave a strain measurement bandwidth of $\Delta\epsilon = 1000\Delta\lambda/1.2$ =4167 μm m^{-1} where the factor 1.2 is a photo-optical constant.

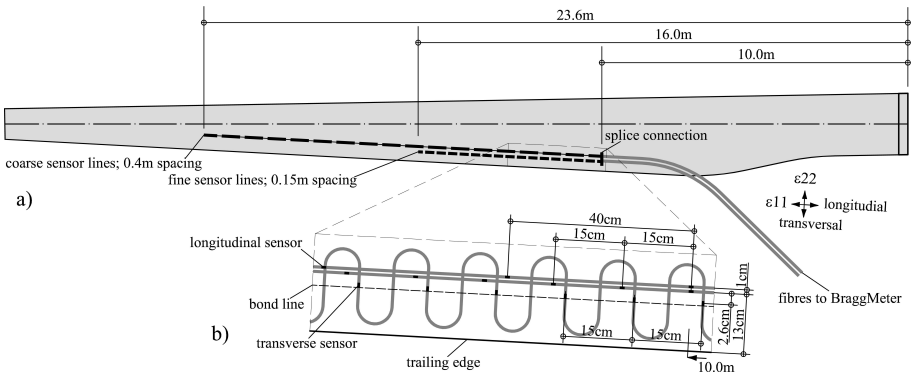

Figure B.3: Position of fibre sensors

B.3.4 Optical displacement measurement

An in-house stereo photogrammetry measurement system was used to measure the 3D displacements of marker points on the trailing edge, as shown in Figures B.4 (c) and (d). The markers were placed at 0.25 m intervals between 12.5 m and 16.0 m with the purpose of tracking the trailing-edge wave deformation. The pattern of the black and white marker points (Figure B.4 (c)) enabled the recognition of the marker point centres by means of the *Automated Image Processing Software* (AIPS). The measurement methodology is based on the pinhole camera principle as described by Atkinson [8]. A description of the AIPS appears in [102]. The stereo photogrammetry principle requires a pair of simultaneously taken images containing both a calibration grid and the measurement object. In the first step of its application, the real-world coordinates and its corresponding image coordinates of the calibration grid are used for camera calibration. In a subsequent step, the camera calibration parameters are used together with the image coordinates of the measurement object to triangulate its real world.

For this purpose two Samsung ST200 cameras were mounted at a rigid elevated position parallel to the trailing edge. Both cameras covered the same measurement area including the calibration grid shown in Figures. B.4(a) and B.4(b). Shown in Figure B.4(d) the calibration grid consisted of two staggered parallel planes with an offset of 5.0×10^{-2} m. Both planes featured a black and white checker-board pattern with a square size of 5.0×10^{-2} m. The calibration grid was placed underneath the trailing edge and aligned with a laser level. A pair of images corresponding to one measurement was simultaneously taken prior to loading, and then at every load step. In order to determine the accuracy of the camera system, the error between the known real world coordinates of the calibration grid and those obtained by triangulation was computed. The error

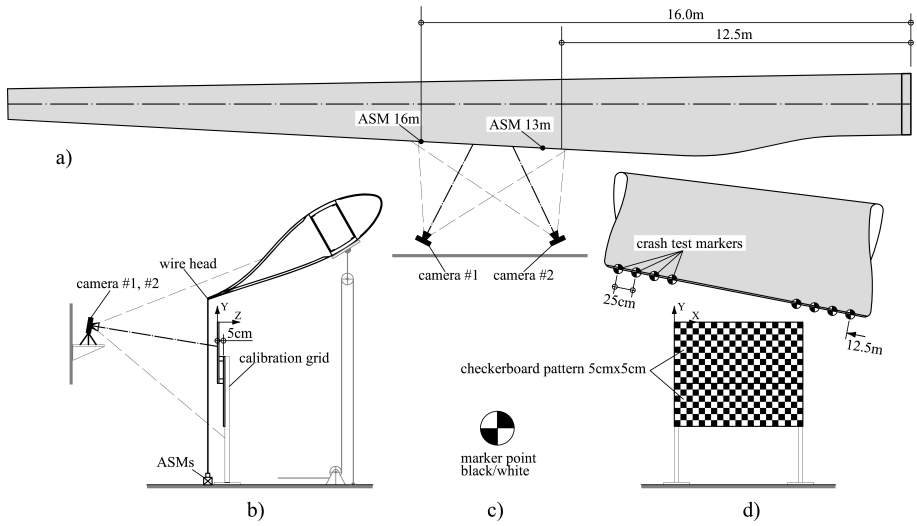

Figure B.4: a) Plane view of the blade with two cameras, b) Cross section of the blade with elevation showing position of cameras and calibration grid, c) Marker point, d) calibration grid and position of marker points from the camera's perspective and measurement coordinate system.

followed normal distribution, where the standard deviations in the x, y and z-directions were δ_x=2 × 10^{-4} m, δ_y=3 × 10^{-4} m and δ_z=7 × 10^{-4} m respectively.

B.3.5 Aeroelastic simulations

DTU's aeroelastic software package *Horizontal Axis Wind turbine Code* HAWC2 11.9 [74, 49] was used to perform aeroelastic simulations in order to predict bending moment distributions along the blade, and to determine forces at the cross sections of the blade for various loads. The aeroelastic bending moments were used to benchmark the applied loads during the blade test. Furthermore, the simulations enabled the computation of SERRs, based on load distributions that the blade would experience during operation.

The airfoil characteristics and cross-section rigidity of the tested 34 m long blade were modelled according to manufacturer specifications for the aeroelastic simulations. However, hub, tower and generator properties were not based on the originally designed platform but instead based on the Neg Micon NM80 turbine platform [118] with a stated rated power of 2.3 MW.

Although the blade being studied is designed for wind turbines with a rated power of 1.5 MW, the turbine used was considered acceptable due to a similar blade length of 38.8 m. The wind turbine was consequently downrated to 1.5 MW and the PI-controller was optimised for the new setup using DTU's aeroservoelastic stability tool *HAWCStab2* [50].

The *Design Load Cases* (DLCs) as directed by IEC-61400-1 [112] were simulated for different levels of turbulence (seeds) and yaw misalignment. The aeroelastic simulations provided the time history of the bending moment vector components $M_x(t)$ and $M_y(t)$ in 17 cross sections along the blade. A three-dimensional bending moment envelope was generated by plotting the maximum bending moment values which occurred during the simulation time in a specific DLC in the cross sections along the blade. Two different bending moment envelopes were generated: The first one – denoted as *CBM* – refers to a *Constant Bending Moment*, corresponding in its magnitude to approximately 57% of the ultimate load of the blade test. The second – denoted as *MDL* – refers to the *Maximum Design Load* in this paper. The *MDL* comprises all DLCs defined in [112]. The bending moments extracted from aeroelastic simulations were multiplied by the corresponding DLC safety factor. An exception was DLC1.1, where the simulations were multiplied by a safety factor of 1.25 according to [112] but the 50-year extrapolation usually required was omitted because the wind turbine site was unknown.

The bending moment magnitudes M_i obtained from the envelope Equation B.1 can be used to calculate the force magnitudes F_i which create a bending moment distribution that emulates those obtained from aeroelastic simulations. These forces were consequently used to load the numerical blade model as discussed in Subsection B.3.6.

$$\begin{pmatrix} F_1 \\ F_2 \\ F_3 \\ F_4 \end{pmatrix} = \begin{bmatrix} \frac{1}{z_1 - z_2} & 0 & 0 & 0 \\ \frac{z_3 - z_1}{(z_2 - z_3)(z_1 - z_2)} & \frac{1}{z_2 - z_3} & 0 & 0 \\ \frac{1}{z_2 - z_3} & \frac{z_4 - z_2}{(z_3 - z_4)(z_2 - z_3)} & \frac{1}{z_3 - z_4} & 0 \\ 0 & \frac{1}{z_3 - z_4} & \frac{-z_3}{(z_3 - z_4) z_4} & \frac{1}{z_4} \end{bmatrix} \cdot \begin{pmatrix} M_2 \\ M_3 \\ M_4 \\ M_5 \end{pmatrix} \tag{B.1}$$

Indices $1 - 4$ represent the locations of the force application points; index 5 represents the root, M_i represents the aeroelastic bending moment magnitude, F_i represents the force magnitudes and z_i denotes the lengthwise position of the individual force application points (Figure B.5(a)).

Figure B.5(b) shows the polar coordinate system defining the bending moment vector and its angular direction α. The associated force vector obtained from Equation B.1 was transformed into the components F_x and F_y of the cross-section coordinate system. A so-called load envelope was generated for *MDL* by plotting the load components at the force application points.

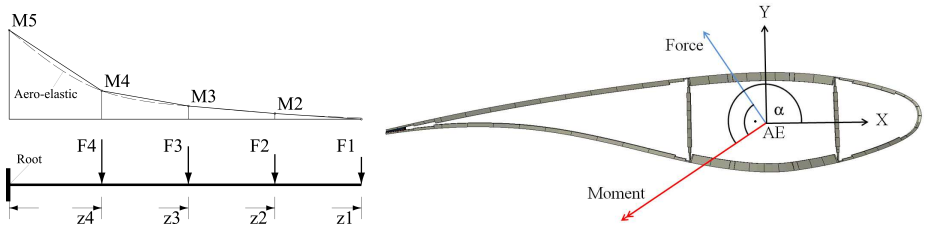

Figure B.5: (a) Schematic bending moment distribution along the blade, (b) Cross section coordinate system and loading directions with bending moment vector and force vector. The angle α represents the direction of the bending moment vector measured counterclockwise from the X-axis.

B.3.6 Finite element analysis

The structural blade design is comprised of a box girder connected to the pressure-side and suction-side panel that form the aerodynamic surface. Panels are themselves connected by a trailing-edge joint and a leading-edge joint. The software package *Abaqus* 6.13 [27] was used for structural analyses of the blade. The panels and box-girder were discretised with 6.7×10^4 8-node doubly curved thick shell elements with reduced integration (Abaqus type S8R). The characteristic element length was 5.0×10^{-2} m. The shell elements were placed at the outer surface of the blade model and had an offset corresponding to half the material thickness. The adhesive of the trailing edge joint was discretised with four layers of 2.75×10^5 8-node linear brick elements with reduced integration and hourglass control (Abaqus type C3D8I). The adhesive with a constant bond length of 8.0×10^{-2} m and a characteristic element size of 5.0×10^{-3} m was felt to provide sufficient accuracy for the *Virtual Crack Closure Technique* (VCCT). Tie constraints were used to connect the brick elements to the shell elements.

The elastic material properties of the trailing-edge laminate layup components – as well as the properties of the isotropic epoxy based adhesive – are listed in Table B.2. Indices 1 and 2 refer to the 0° and 90° material directions respectively, E_{ij} represents the elastic modulus, G_{ij} represents the shear modulus, ν_{ij} denotes Poisson's ratio.

A kinematic (rigid) coupling constraint was applied to the nodes of the root section. All six degrees of freedom of the master node located in the elastic centre of the root section were restrained. The four anchor plates were assumed to be rigid and hence modelled through kinematic coupling constraints tied to the master nodes of each LPs (see Figures B.6 and B.7). For model validation, the

Table B.2: Properties of the composite material in the trailing edge where the abbreviations *Pre*, *HRC* and *UD* denote pre-preg, high resin content and unidirectional laminate respectively.

Properties	*Biaxial Pre*	*Biaxial*	*Triaxial*	*Triaxial HRC*	*UD*	*Adhesive*	Unit
ρ	1890	1894	1864	1683	1931	1180	kg/m^3
E_{11}	11.58	12.75	20.26	16.70	41.26	3.00	GPa
E_{22}	11.58	12.75	10.42	8.59	11.39	3.00	GPa
ν_{12}	0.50	0.50	0.50	0.50	0.33	0.38	-
$G_{12} = G_{13}$	10.66	10.06	7.35	6.61	3.91	1.09	GPa
G_{23}	4.00	4.00	4.00	4.00	3.91	1.09	GPa

load was applied by axial contraction of connector elements. This follower force approach is a realistic representation of the experimental loading conditions. Axial connector elements were also used to model the draw wire transducer (ASM) measurement principle, thereby enabling a direct comparison between measurements and numerical results.

All numerical simulations were performed as quasistatic simulations including geometric non-linearity. For most of the simulations, the Abaqus standard Newton-Raphson solver technique was used. In load cases associated with geometrically non-linear wave formation, equilibrium could not be reached with the standard solver for higher loads. In order to overcome these convergence problems an implicit dynamic solver was chosen instead. The loads were linearly ramped up over a period of 10 s so the kinetic energy was at least two orders of magnitude smaller than the strain energy in each time increment. A viscosity coefficient of 1×10^{-4} was used to stabilise the numerical simulations.

For fracture analysis, the force application scheme described above was modified in order to ease the multidirectional loading procedure. Continuum distributing coupling constraints [27] were assigned to the cross sections at 13.12 m, 18.6 m, 25.04 m and 28.78 m in order to avoid restraining cross-section warping. Loads were applied as concentrated forces at the individual master nodes located in the aeroelastic centres of the cross sections. Figure B.8 shows the distributed coupling constraints at 13.12 m.

The VCCT tool in Abaqus was used to compute the SERRs in a 1.0×10^{-2} m crack introduced in the mid-surface of the adhesive trailing edge joint (Figure B.9).

Hard normal contact conditions and tangential frictionless contact conditions were assigned to the crack surfaces to prevent material interpenetration. For a detailed description of the VCCT, the reader is referred to Krueger [69] and [27]. Equations B.2 and B.3 were used to compute the in-plane (ψ) and out-of-plane (ϕ) mode mixity angles.

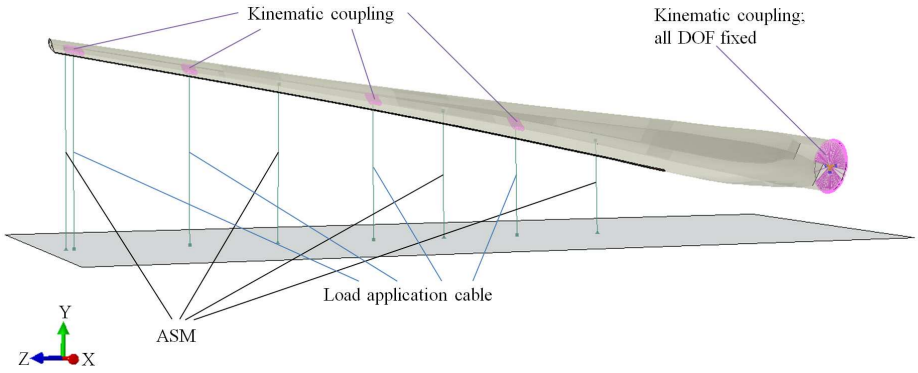

Figure B.6: Wind turbine blade model simulating test conditions for validation. Boundary conditions at the root and both LPs and ASMs modelled with axial connector elements tied to the strong floor.

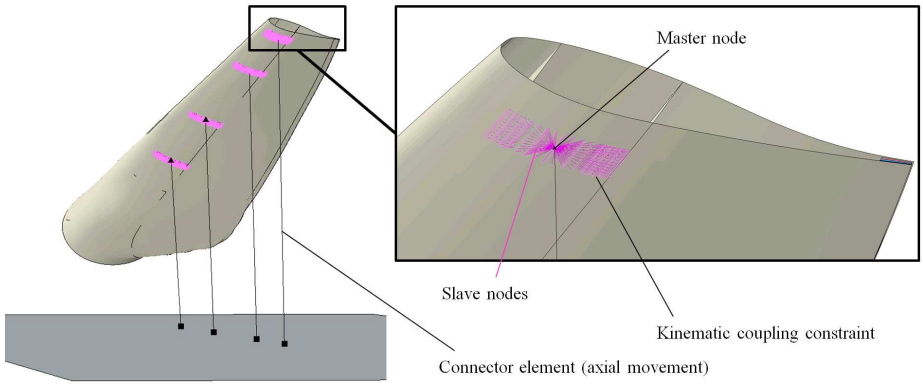

Figure B.7: Detail of kinematic coupling constraint used to model the load, similar to the blade test.

$$\psi = arctan\sqrt{\frac{G_{II}}{G_I}} \tag{B.2}$$

$$\phi = arccos\sqrt{\frac{G_{III}}{G_I + G_{II} + G_{III}}} \tag{B.3}$$

where G_I, G_{II} and G_{III} are the modal SERRs obtained by the VCCT.

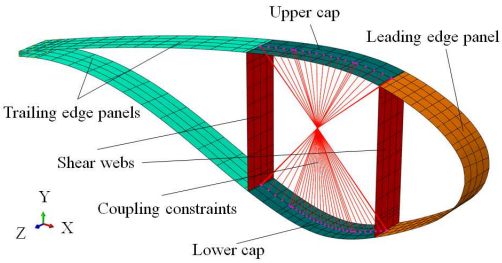

Figure B.8: Blade model cross-section slice with main parts and continuum distributing coupling constraints connected to the shell nodes of the caps with a central master node at the aeroelastic centre.

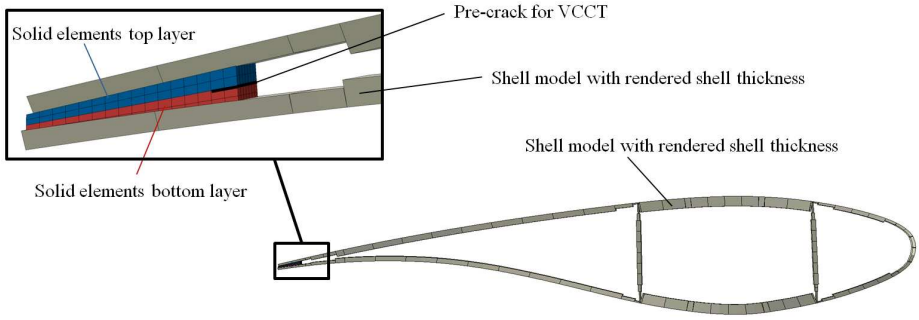

Figure B.9: Cross-section slice with rendered shell elements and detail of solid element discretisation of the adhesive in the trailing edge. A crack of 1.0×10^{-2} m is located between the top and bottom solid element layer of the adhesive bondline. Tie constraints connect the solid elements to the shell elements.

Kenane and Benzeggagh [66] suggest that a crack propagates when G_{tot} given in Equation B.4 exceeds G_{equ} given by Equation B.5. Equation B.5 was used to determine the proximity to crack initiation and to obtain the critical loading directions.

$$G_{tot} = G_I + G_{II} + G_{III} \tag{B.4}$$

$$G_{equ} = G_{Ic} + (G_{IIc} - G_{Ic}) \left(\frac{G_{II} + G_{III}}{G_I + G_{II} + G_{III}} \right)^{\eta} \tag{B.5}$$

where G_{Ic} and G_{IIc} are the experimentally obtained critical Mode-I and Mode-II SERRs. For the sake of simplicity, the initiation fracture energies G_{Ic}=665 J/m^2 and G_{IIc}=1216 J/m^2 of fillet detail *Type-B* in [30, Figure 5 (b) and Table 1] were used. The exponent was set to η=2 for brittle resins.

B.3.7 Wave extraction techniques

In an attempt to separate the local trailing-edge wave from the total global displacements, two different approaches were used.

The first approach is based purely on experimental results where the total global displacements are described by Equation B.6. It was found that a third-order polynomial fits the measured cap deformations given in Table B.3 and was consequently used for the base deformation of the trailing edge. The local wave portion was approximated by a sine function within the measurement interval.

$$u_y(z) = a_0 z + a_1 z^2 + a_2 z^3 + a_3 \sin(f z) \tag{B.6}$$

where z represents the lengthwise position measured from the root, and both $a_{0,1,2,3}$ and f are constants. The constants of Equation B.6 were iteratively obtained by a non-linear least square method using the Matlab curve fitting tool [81].

The second approach is a hybrid method combining numerical results and measurement values which allows more data points to be considered than in the first approach. It was found that the polynomial given by Equation B.7 fits the numerically obtained global trailing edge deformation between 7.0 m and 29.5 m at a low load level where the wave was imperceptible. Equation B.7 was therefore assumed to represent the base deformation of the trailing edge in absence of the wave. The fitting constants were obtained in Matlab [81] by a non-linear least square method. The local wave was obtained by subtracting the base deformation from the measured or numerically predicted total global displacements.

$$u_y(z) = a_0 z^5 + a_1 z^4 + a_2 z^3 + a_3 z^2 + a_4 z + a_5 \tag{B.7}$$

where z represents the lengthwise position measured from the root and $a_{0,1,2,3,4,5}$ are curve-fitting constants.

B.4 Results

B.4.1 Aeroelastic simulation results

Figure B.10(a) shows a normalised contour plot of the root bending moment envelope for MDL. The dashed lines indicate the angular direction of the experimentally applied bending moment at α=210° and the two critical angular directions (α=135° and α=240°) as discussed in Section B.4.3. The highest bending moment magnitude occurred for α=163°.

Figure B.10(b) shows the spanwise bending moment distribution of MDL at an angular direction of α=210° and the maximum applied load during the experiments. The latter is denoted as *Ultimate Load* (UL) and defined as 100 % whereas the MDL corresponds to approximately 90 % of the applied ultimate load. Figure B.10(b) shows that the experimentally applied bending moment distributions closely resemble those obtained from aeroelastic simulations. The MDL functioned as a reference load in order to evaluate the UL under which the blade failed.

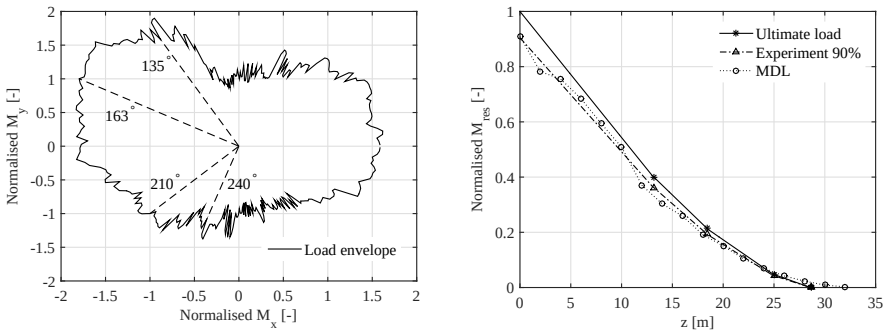

(a) (b)

Figure B.10: (a) Bending moment contour plot for MDL and angular directions for selected load cases, (b) Comparison of maximum applied bending moment during the experiments and extracted bending moment (MDL) from aeroelastic load calculations.

B.4.2 Experimental results and model validation

The numerical blade model was first validated against experimental data for the load case presented in Subsection B.3.1. Table B.3 lists the measured and numerically obtained cap deformations. The maximum relative error was less than 2 % at the blade tip.

Table B.3: Experimentally and numerically obtained global cap deformations at four different measurement points for the 76 % load step.

	z=29.5 m	z=22.0 m	z=16.0 m	z=10.0 m	Unit
ASM	-1.914	-0.7974	-0.307	-0.102	m
Numeric	-1.880	-0.8023	-0.311	-0.102	m
Rel. Error	-1.77	0.62	1.38	0.00	%

Figure B.11(a) shows the trailing edge deformation from the perspective of camera 2 at a load step of 57 % at the onset of the wave. Figure B.11(b) shows the trailing edge at a load step of 76 % with a distinct wave in the centre of the measurement length.

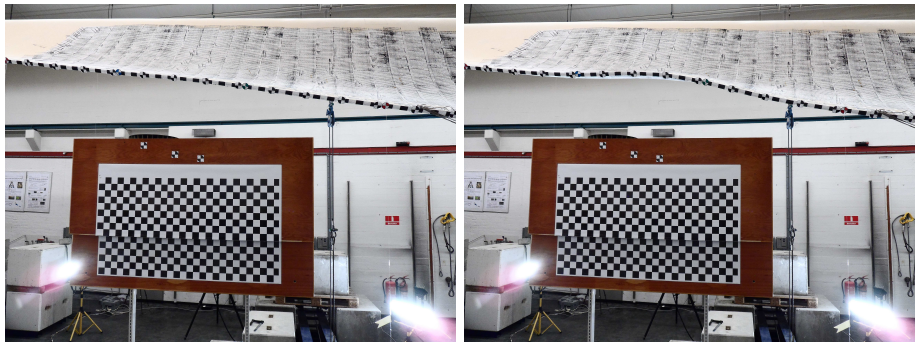

(a) (b)

Figure B.11: (a) Trailing edge deformation at 57 % load level with marker points and calibration grid (below), (b) Trailing edge deformation at 76 % load level with a distinct wave peak.

Table B.4 lists the vertical trailing edge displacements at 13 m and 16 m obtained by ASM measurements and numerical analysis for three subsequent load steps of 57 %, 67 % and 76 %.

Table B.4: Experimentally and numerically obtained global trailing edge deformations for three load steps.

Load step	ASM 13 m	Optic 13 m	Numeric 13 m	ASM 16 m	Optic 16 m	Numeric 16 m
%	m	m	m	m	m	m
57	-0.113	-0.114	-0.113	-0.204	-0.204	-0.206
67	-0.130	-0.132	-0.129	-0.237	-0.236	-0.238
76	-0.149	-0.150	-0.143	-0.271	-0.274	-0.270

The graphs in Figures B.12(a) and B.12(b) represent the first wave extraction approach described in Section B.3.7.

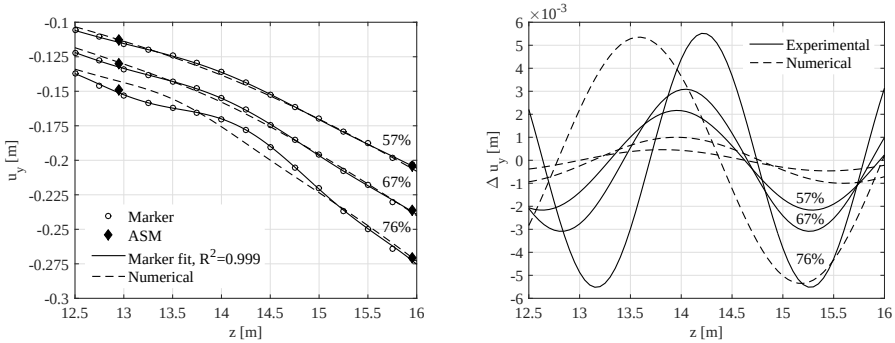

(a) (b)

Figure B.12: (a) Comparison of measured global vertical trailing edge displacements u_y of marker points and ASMs with numerically obtained displacements for three different load levels, (b) Comparisons of local deformation wave given by $\Delta u_y(z) = a_3 \sin(fz)$ extracted from measurements and numerical analysis.

Figure B.12(a) shows that the solid graph given by Equation B.6 fits the optical measurement data (circular markers) well. Figure B.12(b) shows that in the wave given by the last term of Equation B.6, the peak shifted slightly towards the tip with increasing load. The amplitude progressively increased from 2×10^{-3} m to 6×10^{-3} m. The wavelength $\Lambda = 2\pi/f$ decreased from approximately 2.7 m at 57 % to 2.1 m at 76 %. The dashed graphs represent the numerically predicted displacements post-processed using the same procedure. Figure B.12(a) shows

that the numerical model appropriately predicts the measured response for 57 %. The deviation increases with increasing load as the model predicts the wave peak at a different location. Figure B.12(b) shows a likely prediction of the amplitude at 76 %.

The results of the local wave as found by the hybrid wave extraction approach (Section B.3.7) are shown in Figures B.13(a) and B.13(b). The base deformations given by Equation B.7 are represented by dotted graphs. The solid graphs represent the numerically predicted deformations and the circular markers represent measurement results. Figure B.13(b) compares the measured and numerically predicted deflections subtracted from the numerically determined base deformations. It shows that the numerically predicted early wave amplitudes correspond to those obtained from measurements. The numerical model predicted the location of the positive wave peak reasonably well at an offset of 0.7 m (Figure B.13(b)). Whilst the model underestimated the amplitude for higher load levels (76 %) it deviated insignificantly for lower ones. The reason for the deviation for higher loads can be explained by observation during the experiment. The trailing-edge wave caused a kink in the pressure side panel inducing high transverse deformation gradients which caused local panel failure prior to trailing-edge debonding. The model did not account for the local stiffness degradation caused by panel failure. Hence, wave amplitudes were underpredicted for higher load steps due to overprediction of transverse stiffness.

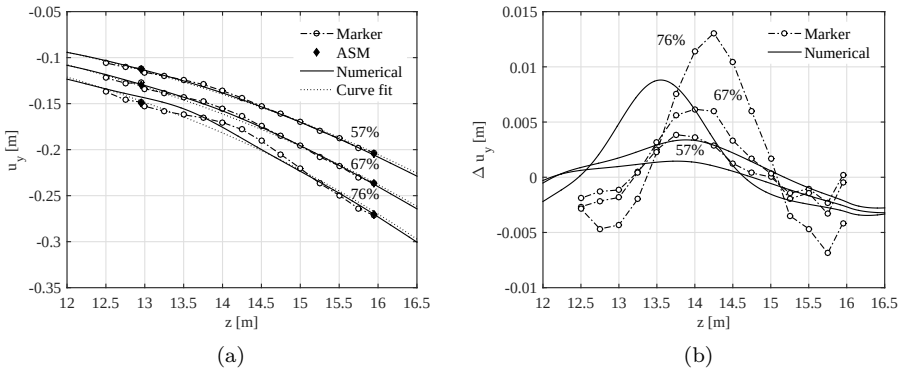

Figure B.13: (a) Comparison of measured global vertical trailing edge displacements u_y of marker points and ASMs with numerically obtained displacements for three different load levels, (b) Comparison of local deformation $\Delta u_y\,(z)$ as offset from a curve fit through the global displacement extracted from the numerical analysis.

The comparison of the experimental trailing-edge response with the numerical prediction in Figures B.14(a) and B.14(b) show that the latter underpredicts the amplitude since stiffness degradation was not taken into account.

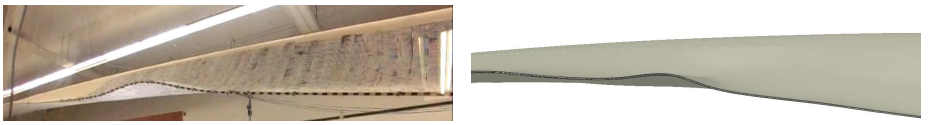

(a) (b)

Figure B.14: (a) Trailing edge deformation during the blade test at the 100 % load step, (b) Numerical result showing the trailing edge deformation at the same load step.

Figures B.15(a) and B.15(b) compare the measured and numerically obtained ϵ_{11} and ϵ_{22} strain distributions at a load level of 57 %. FBG measurements for load steps higher than 57 % are not presented because ϵ_{22} measurements exceeded the measurement range of the sensors.

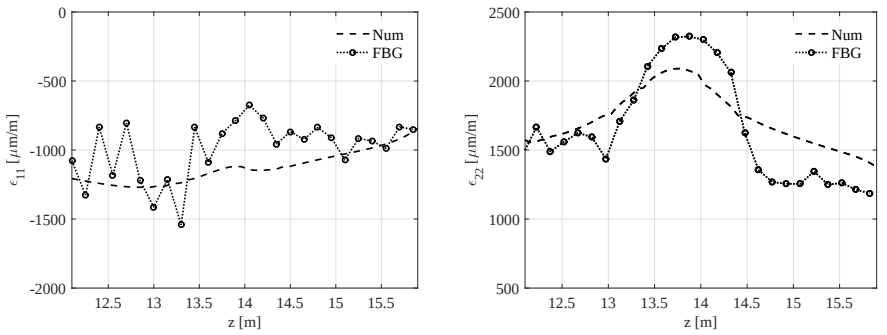

(a) (b)

Figure B.15: Measured (at 0.15 m spacing) and numerically predicted longitudinal strain ϵ_{11} (a) and transverse strain ϵ_{22} (b) along trailing edge at 57 % load steps.

The ϵ_{11} measurements show considerable fluctuations between 10.0 m and 13.5 m whereas the remaining data is more consistent. It was found that the sensors in the noisy area were placed on the sandwich core region of the trailing edge panel, while the remainder was placed on the pure laminate (Figure B.16). The

different placements were inevitably caused by the variation of the sandwich core width along the blade which interfered with the constant offset of the sensors from the trailing edge. It is conjectured that the fluctuations are related to local strain concentrations induced by gaps in the material which are more likely to occur in the sandwich core than in the pure laminate. Figure B.15(a) shows that the model, which does not take micro defects into account, predicts the average of the measured strains which corroborates the conjecture. Furthermore, it can be seen that ϵ_{22} levels at the critical wave are higher than the ϵ_{11} strains which is consistent with the aforementioned excessive transverse deformations. The comparison between the numerical prediction and the experimental measurements results in reasonable good agreement.

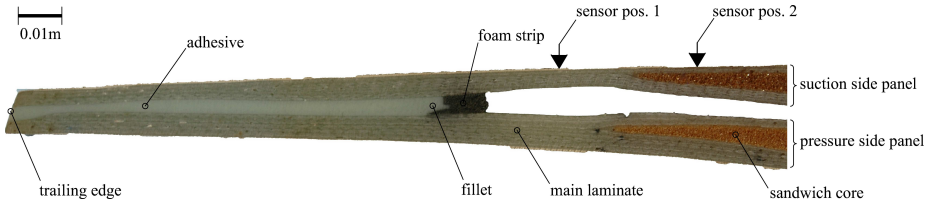

Figure B.16: Trailing-edge slice extracted from the tested wind turbine blade showing adhesive joint between pressure side and suction side shells with sensor location on the pure laminate (sensor pos.1) and above the sandwich core (sensor pos.2).

B.4.3 Fracture analysis results

The model was subsequently used to investigate the structural behaviour of the blade subject to the *CBM* and *MDL* load envelopes for a complete 360° revolution in angular increments of $\Delta\alpha$=15°. Figures B.17(a) through B.18(b) show SERRs extracted at the peak of the critical buckling wave as it appeared in the model at 13.0 m upon ultimate loading. The bending moment magnitude represents 57 % of the ultimate bending moment in the 13.0 m cross section and represents the measurable onset of wave formation. The constant bending moment distribution at 57 % was chosen to investigate the effects of in plane cross-section warping without the influence of the wave, in order to make the results comparable to previous studies. Figures B.17(a) and B.17(b) show two distinct G_I and G_{II} ridges whose maxima occur between α=90° and α=120°. Figure B.18(a) shows three small G_{III} ridges occurring at α=45°, 150° to 165° and 255°. The out-of-plane shear (Mode-III) seemed to occur regularly every 90°. Figure B.18(b) shows a critical angle of α=120° for the constant bending

moment with a low utilisation level of G_{equ} and another small peak at α=255°. The first peak occurring in quadrant *QII* is Mode-I dominated as shown in Figure B.17(a) whereas the second peak is governed by Mode-III SERR as shown in Figure B.18(a).

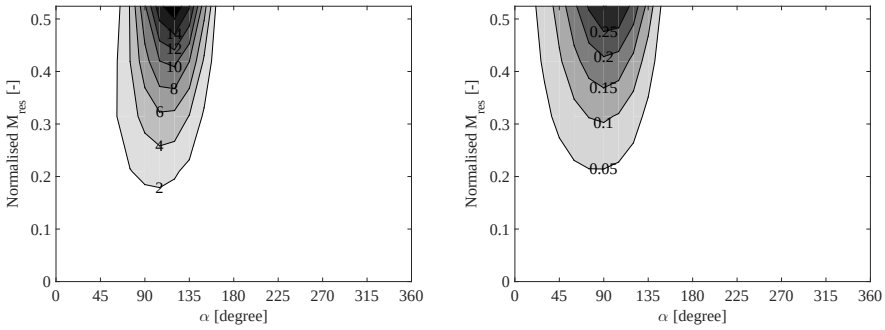

(a) G_I (b) G_{II}

Figure B.17: SERR contour plots in (a) and (b) as function of the CBM under different angular directions with its angle α and its normalised bending moment magnitude.

Figure B.19(a) shows two peaks, the first occurred at α=135° and reaches approximately 20 % of the critical energy level. The second peak occurred at α=240°. The plots show that the second peak exceeds G_{equ}. In Figure B.19(b) the mode-mixities ϕ and ψ were plotted for the MDL envelope evaluated at 13.0 m. For α=135° the in plane mode mixity is Mode-I dominated, whereas between α=225° to α=245° Mode-III prevails.

Figure B.20(a) through B.20(b) show SERRs obtained for MDL along the crack front between 12.25 m and 13.75 m for α=135°. This direction yields the highest Mode-I SERR levels for both CBM and MDL. Under this load direction, G_I is significantly higher than G_{II} and G_{III}.

Figures B.21(a) through B.21(b) show SERRs obtained for MDL along the crack front between 12.25 m and 14.5 m for α=240°. This direction provokes the highest wave amplitudes in the trailing edge thus maximising the impact on the SERRs. Whereas the SERR levels of CBM were negligibly small, they increased significantly for MDL. Figure B.21(a) shows that G_I was negligible but that G_{II} and G_{III} values increased significantly with Mode-III governing the mode mixity. Figure B.21(b) shows that the critical peaks occurred at around 12.75 m and 13.8 m. The critical G-III peaks flanked the trailing-edge wave deformation at 13.29 m. At 13.29 m the G_I and G_{III} were suppressed and G_{II} increased

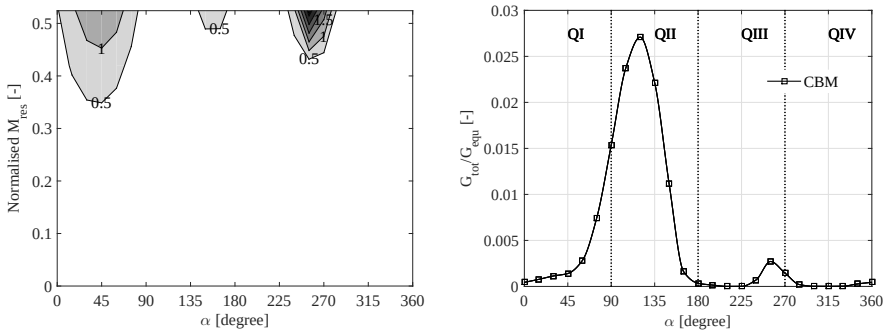

(a) G_{III} (b)

Figure B.18: (a) SERR contour plot as function of the CBM under different angular directions with its angle α and its normalised bending moment magnitude, (b) G_{tot}/G_{equ} as a function of the bending moment vector angle α and its magnitude subdivided into four quadrants indicated by dotted lines for a constant bending moment *CBM*.

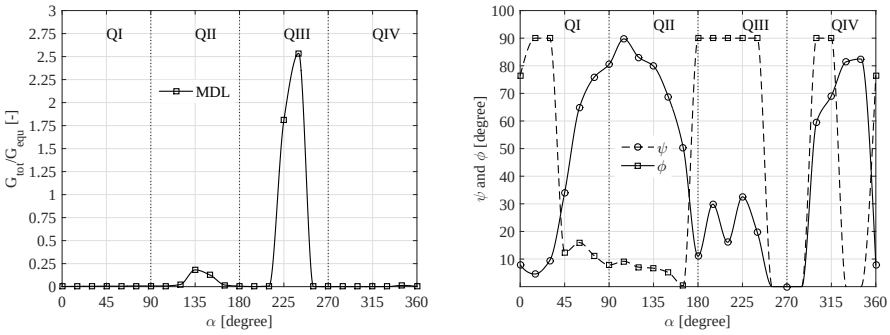

(a) (b)

Figure B.19: (a) G_{tot}/G_{equ} plot of MDL, (b) Mode-mixities as function of the bending moment angle α for MDL.

instead.

Similar behaviour was observed for the experimental load direction of 210° and under the previously described load conditions as shown in Figures B.22(a) and B.22(b). Here, the maximum trailing edge deformation at UL was located at

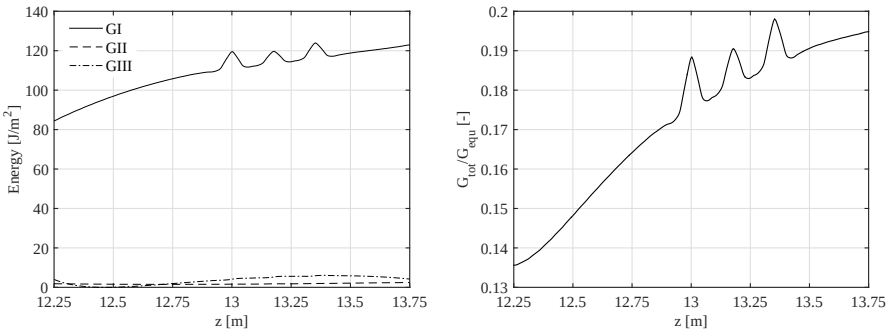

(a) (b)

Figure B.20: (a) Modal SERR distributions for MDL for α=135°,(b) The corresponding G_{tot}/G_{equ} distribution.

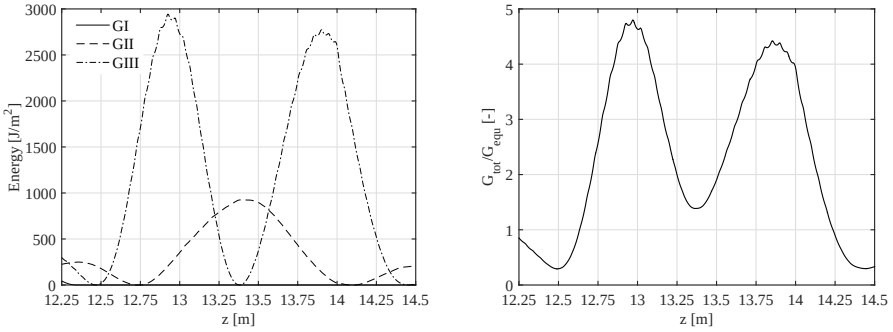

(a) (b)

Figure B.21: (a) SERR distributions for MDL for α=240°, (b) The corresponding G_{tot}/G_{equ} distribution.

13.15 m.

Figures B.23(a) and B.23(b) show in-plane warping deformations of the trailing edge panels under MDL for α=135° and α=240°, with a cutting plane in the most critical locations at 13 m and 13.30 m, respectively. Figure B.23(a) shows a Mode-I opening under α=135° whereas the wave under α=240° suppressed Mode-I by the panel being closed.

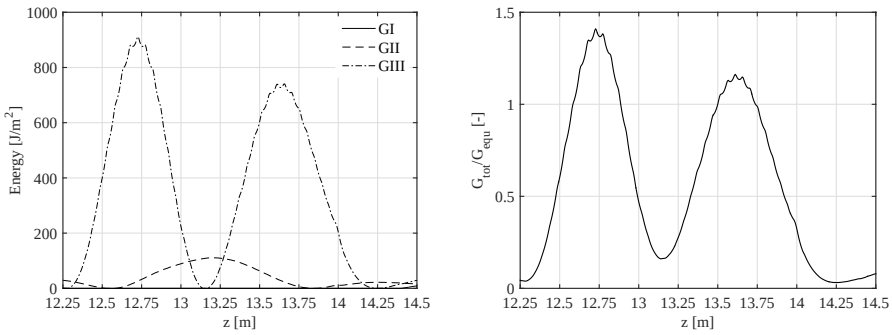

(a) (b)

Figure B.22: SERR distributions for the experimental loading condition with α=210° and the corresponding G_{tot}/G_{equ} plot.

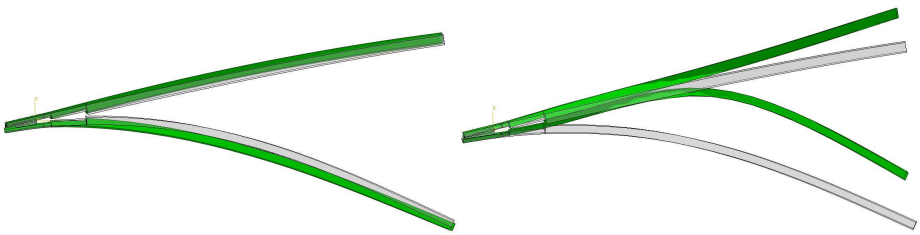

(a) (b)

Figure B.23: Cross section showing the local in plane warping deformation of the trailing edge for MDL. (a) The trailing edge deformation (with scale factor 2) for the blade under a bending moment angle of 135° and a cutting plane at 13 m. (b) The trailing edge deformation for the blade under a bending moment angle of 240° and cutting plane at 13.30 m.

B.5 Discussion

Measurement data of displacements and strains show that a longitudinal wave occurred in the trailing edge at an unexpectedly early loading stage. The numerical model predicted the location of the positive wave peak reasonably well at an offset of 0.7 m (Figure B.13(b)). The reason for the deviation for higher loads can be explained by damage induced by stiffness degradation of the trailing edge panels near the critical wave. Stiffness degradation associated with

progressive failure modelling was omitted in the present analysis. More information regarding the influence of panel damage on local wave formation appears in [45].

The observed trailing-edge wave formation can hardly be characterised as *bifurcation buckling* as defined in [114]. The wave did not pop up at a critical load as would be expected in a classic bifurcation buckling situation as discussed by Kühlmeier [70]. Instead the wave formed gradually from an early loading stage on and prevented the identification of post buckling behaviour. Nor did the observed phenomenon comply with the definition of *limitpoint buckling* stipulated in [114] since the load-deformation relationship did not reach a distinguishable maximum when deformations were increased in an uncontrolled manner. Difficulties of distinguishing buckling phenomena in wind turbines were also described by Cox and Echtermeyer [25] and in greater detail by Lindgaard and Lund [78].

The G_I and G_{II} ridges shown in Figures B.17(a) and B.17(b) can be explained by the Brazier effect as discussed in [31]. It shows that the SERRs in this loading direction are Mode-I dominated when the lengthwise bending stresses in the trailing edge are positive (tension). Fracture analysis indicates a critical bending moment range between α=90° and α=135° as far as the Brazier effect is concerned. Usually a second G_I ridge was expected between 270° and 300° but was suppressed by the wave when the bending stresses in the trailing edge were negative (compression).

The G_{tot} levels for cases dominated by Mode-I remained well below the G_{equ} values for static crack growth. However, it can be seen from Figure B.17(a) for lower load levels (CBM) and in Figure B.20(a) for MDL that G_I reaches levels between 80 J/m^2 and 120 J/m^2. These are well within experimentally obtained fatigue thresholds of adhesively bonded double cantilever beam (DCB) specimens reported by Ishii [60, Figure2] and Azari [9]. Note that the fatigue thresholds were obtained under controlled conditions. The fatigue threshold in wind turbine blades should perhaps be lowered due to flaws induced by manufacturing, and residual stresses caused by curing.

Figures B.21(a) to B.22(b) show that geometrical non-linear wave formation under MDL caused a rapid and progressive increase of the SERRs. In the present case G_I was suppressed between 12 m and 14 m. Instead G_{III} dominated the experimentally tested load case. Figure B.21(b) and B.22(b) show that critical G_{tot}/G_{equ} peaks occurred beside to the peak of the wave which in both cases exceeded G_{equ}. This shows that a geometrical non-linear wave in the trailing edge can lead to crack growth under extreme loading conditions. G_{tot}/G_{equ} peaks occurred for both CBM and MDL at qualitatively similar angular directions, which indicates that these directions should undergo further investigations.

Note that torsional aeroelastic moments were not studied in this analysis which

means that G_{III} SERRs are probably under-estimated in some cases. Some torsion was induced into the blade by bend-twist coupling and by load eccentricities caused by bend-bend coupling. However, torsional aeroelastic loads should be studied in future investigations.

B.6 Conclusion

The findings can be summarised as follows:

i It was shown both experimentally and numerically that a geometric non-linear longitudinal trailing-edge wave can occur in blades which are designed to prevent local buckling. Such a wave can have serious consequences for the integrity of the adhesive trailing-edge joint.

ii Surface strain measurements on laminates with FBGs are influenced by local effects (e.g. material imperfections) leading to strain concentrations, and by the alignment between the fibre reinforcement and the FBG sensor.

iii Two critical bending moment vector directions exist in the investigated case. The first occurred at α=135° and is consistent with the Brazier effect reported in [31]. The second occurred at approx. α=240° and is associated with geometrically non-linear wave formation.

iv The numerically obtained G_I levels exceeded experimentally obtained fatigue thresholds of adhesive joints.

v The trailing edge wave suppressed G_I and amplified G_{II} and G_{III}. Such induced SERR levels can lead to adhesive joint failure under maximum design loading conditions.

vi Pure flap-wise and pure edge-wise loading directions in blade certification tests might not be sufficient when adhesive joint failure is concerned, tests under combined loading directions should be considered.

vii Trailing-edge subcomponent tests should not only examine Mode-I fracture but also mixed mode conditions.

Acknowledgement

The work is supported by the Danish Energy Agency through the 2010 Energy Technology Development and Demonstration Program (EUDP). The title of the supported EUDP-project is "Experimental Blade Research - Phase 2" and has

journal no. 64011-0006. The research paper is furthermore based upon work supported by the new Danish Centre for Composite Structures and Materials for Wind Turbines (DCCSM), grant no. 09-067212 from the Danish Strategic Research Council. The support is gratefully acknowledged.

The authors wish to thank Andreia Pereira and Nuno Costa from *HBM FibreSensing* for providing the measurement equipment and their expertise. At this point the support of Gilmar Ferreira Pereira from DTU KOM is gratefully acknowledged. The authors are grateful for DTU AED to set up the HAWC2 model. Finally, the authors would like to acknowledge the support of Christian Lyngbæk from DTU Nutech.

Paper C

On initiation of trailing edge failure in full-scale wind turbine blade test

Article status: Submitted on the 28^{th} of October 2015. A revised version of the article has been accepted for publication with the title "Initiation of trailing edge failure in full-scale wind turbine blade test".

Article title: *Initiation of trailing edge failure in full-scale wind turbine blade test*

Authors: P.U. Haselbach and K. Branner

Journal title: Engineering Fracture Mechanics

DOI information: 10.1016/j.engfracmech.2016.04.041

C.1 Abstract

Modern wind turbine rotor blades are usually composed of large, complexly shaped parts, forming hollow structures and bound together by adhesive joints. The parts normally consist of composite fibre materials and sandwich structures. The aero-elastic design is often a compromise between highly efficient airfoils – which provide optimal lift – and robust structural design. The design requirements usually lead to tapered and twisted blades and thus, together with the highly anisotropic material behaviour, results in complex objects for strength and stiffness predictions. In the design process of rotor blades, various analytical and numerical tools are used from the first draft to the final design, before full-scale tests are conducted. Full-scale tests are expensive and time consuming. Ideally, an experimental test only validates existing prediction results without any unforeseen findings. Therefore, designers try to predict blade response as accurately and reliably as possible.

This study focused on the evaluation of the reliability and accuracy of a numerical shell model, the predictive capabilities of existing failure criteria, and means of revealing ultimate failure in the testing of a 34 m long blade. The experimentally obtained blade response, based on measurements from linear cable position sensors that identify the global blade displacement – as well as the use of *Digital Image Correlation* (DIC) techniques that evaluate local trailing edge deformations – was compared by numerical simulations. Also investigated was the geometrical non-linear buckling effect of the trailing edge under combined loading, and how it affects the ultimate strength of a blade.

The study details the interaction between trailing edge buckling on damage onset and sandwich panel failure. Furthermore, the investigation clarifies the strength and weakness of plane stress failure criteria. The numerically applied fracture mechanics approaches showed good agreement with the experimental results and helped to understand the relations between trailing edge buckling and blade failure.

C.2 Introduction

Rotor blade issues constitute approximately 2% to 5% of the annual failure rate of wind turbines but cause 8% to 20% of the total downwind time of wind turbines, according to an NREL report [101]. About 2% of wind turbines during their first 10 years of operation require blade replacements. Rotor blades see increased failure rates or reduced reliability as the concept grows from simple designs with small rotor diameters towards more advanced technologies with a bigger rotor span [101].

Inspection reports and technical papers such as Ataya and Ahmed [7] indicate that trailing edge failure is frequently observed in rotor blades. The cause of trailing edge failures is complicated and is often due to a combination of complex loading conditions, anisotropic material behaviour, complex geometries, manufacturing process and blade design. A comprehensive investigation of trailing edge damage in a wind turbine rotor blade and the complex interaction of various causes are described in [46]. Non-linear geometry effects and their impact on the trailing edge have been studied in [7, 31, 32, 46]. The effect of bondline shapes was investigated by Eder and Bitsche [30].

Often, simplified *Finite Element Analyses* (FEA) methods like beam theories, cross-section slice approaches, linear *Beam Cross Section Analysis Software* (BECAS) [18] or similar methods are used to predict the rotor blade strength during the design process. In general, these methods are computationally efficient but have the disadvantage of neglecting details or the comprehensive view. Blade tapering effects and non-linear geometrical effects are often disregarded by these methods.

Rosemeier et al. [97] shows the need of non-linear analyses in blade design and uses the same 34 m blade as in this study. A linear strength analysis did not reveal the critical areas, while a geometrically non-linear analysis revealed the failure mechanism and mode as shown in an ultimate test. In Yang et al. [125], a 40 m blade was tested to failure at 160 % of its design load and compared with geometrically non-linear analysis. The structural collapse was caused by debonding of the aerodynamic shell amplified by local buckling and delamination.

In order to understand the stresses and strains occurring under complex loading and to predict the blade response accurately, detailed structural modelling with *Finite Element Methods* (FEM) of the entire wind turbine blade must be conducted. This approach can be computationally expensive. Shell element models are often used to model blades. But does this method allow accurate predictions of trailing edge failures? Can the study of trailing edge failure be included in the shell model without huge modelling efforts and still represent damage mechanics sufficiently?

This study explains how a simplified trailing edge model can predict the effect of damage in the trailing edge, and how non-linear effects affect the response of the wind turbine blade structure under ultimate loading. Numerical studies were compared with experimental findings for a 34 m blade.

C.3 Methods

C.3.1 Experimental setup

DTU Wind Energy tested three wind turbine rotor blades of the 1.5 MW class with an original length of 34 m. The blade tip was truncated at radial position of 29.5 m in order to a fit into the blade testing facility at DTU Risø Campus. The blade root was bolted to an adapter ring under a pitch angle of 120°, which refers to an bending moment angle of 210° with reference to aeroelastic simulations. The adapter and thus the blade axis had an angle of 8° in order to increase the distance between blade tip and floor. Four curved anchor steel plates measuring 0.4 m x 0.4 m x 0.015 m were glued to the blade on the suction-side cap and acted as *Load Points* (LPs). Pulleys were connected to the adhesively connected anchor plates. The blade was loaded by means of displacement controlled winches pulling steel cables through the pulleys towards the floor (Figure C.1).

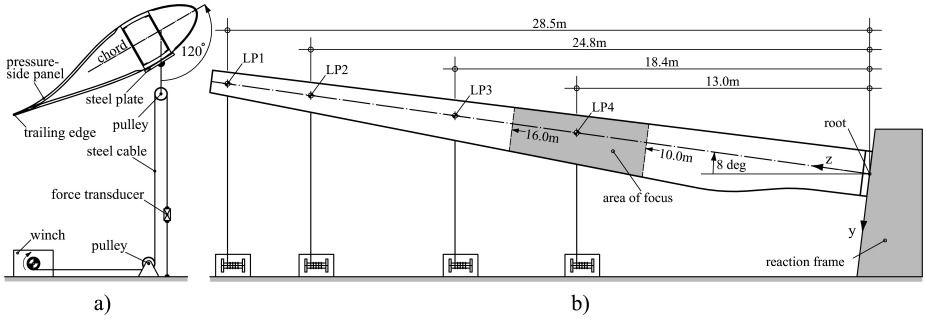

Figure C.1: Sketch of the experiment setup (taken from Haselbach et al. [46]).

The blade was loaded by pulling incrementally at all load points at a low rate of ≤ 0.1m/min, leading to a quasi-static load. The blade deflection was measured by the use of linear cable position sensors of type *ASM Posiwire 6250* (ASM). Four ASMs measuring the global blade displacement between suction side cap and floor along the radial blade position of z=10 m, z=16 m, z=22 m and z=29 m were installed.

The trailing edge displacement between 10 m and 16 m radial position was measured by means of an optical displacement measurement camera system and two additional ASMs attached to the trailing edge at 10 m and 16 m. The optical displacement measurement system is an in-house stereo photogrammetry that tracks the 3D displacement of marker points along the trailing edge and is

described in detail in [46].

C.3.2 Applied loads and aero-elastic simulations

A bending moment distribution and magnitude corresponding to approximately 110 % of the maximum design load extracted from aero-elastic simulation was applied. The load ratio, describing the load distribution between the individual LPs, is given in Table C.1. The highest load was applied to LP1, slightly lower forces at LP2 and similar forces for LP3 and LP4.The loads applied at the LPs leading to the maximum bending moment under which the blade failed are defined as the reference loads. The load ratios are calculated by normalising the loads of the individual LPs to the maximum load applied at LP1.

Table C.1: Locations and target load ratio for the four load points (LPs).

	LP1	LP2	LP3	LP4
Distance	28.50 m	24.80 m	18.40 m	13.00 m
Ratio factor η_i	1.000	0.937	0.775	0.775

Aero-elastic simulations with the DTU software package *HAWC2* version 11.9 (Horizontal Axis Wind turbine simulation Code 2nd generation [68, 75]) were conducted to benchmark the ultimate load of the blade. All relevant *Design Load Cases* (DLCs) according to IEC 61400-1 [112] were computed in order to predict the design load. The blade airfoil geometry and cross-section stiffness properties of the blade were used together with an available Neg Micon NM80 turbine. Originally, the NM80 was designed for a rated power between 1.75 MW and 2.5 MW. The wind turbine model of the NM80 was chosen due to similar blade lengths of 38.8 m. The turbine model was down-rated to 1.5 MW and its controller setup adjusted accordingly. The controller was fitted by means of the aero-elastic-servo-elastic stability tool HAWCStab2 [50]. The extreme loads include the DLCs corresponding safety factors. The bending moments for cross sections along the blade span for a load direction of 210° were evaluated and the highest magnitudes picked. From each individual cross section a bending moment distribution for the blade for the given angle could be determined. The procedure and chosen model were considered to be suitable as a reference for comparison with the experimentally determined *Ultimate Load* (UL).

C.3.3 Numerical model and approaches

For the Finite Element Analysis, Abaqus version 6.14 [27] was used. The blade geometry was discretised with 67,000 8-node double curved thick shell elements with reduced integration (Abaqus type S8R) with a characteristic element length of approximately 0.05m. The second-order Abaqus/Standard thick shell element type was chosen because its characteristics are suitable for the analysis of composite and sandwich shells since it takes transverse shear flexibility by Mindlin shell theory into account. The transverse shear flexibility can be important when sandwich constructions are modelled, where parts of the cross-section are made of a more flexible material such as the sandwich core material in rotor blades [27].

The adhesive bondline at the trailing edge between the upper and lower aerodynamic shell was modelled by the use of 8-node linear brick elements with reduced integration and hourglass control (Abaqus type C3D8I). This modelling approach was used in order to easily apply different fracture mechanics approaches to the trailing edge. The adhesive of the trailing edge starting at a radial position of 8m to the end of the truncated blade at 29.5 m was modelled with a bondline width of 0.08m. Different degrees of discretisation depending on the chosen fracture mechanics model were used in order to balance accurate prediction and computation time. The finest discretisation was based on 275,000 8-node linear brick elements discretising the geometry with four layers of elements through the thickness and a characteristic element length of 0.005 m. The roughest discretisation had 120,000 8-node linear brick elements with only two layers of elements with a characteristic element length of 0.01 m. The solid brick elements were connected by means of tie-constraints to the shell elements as shown in Figure C.2.

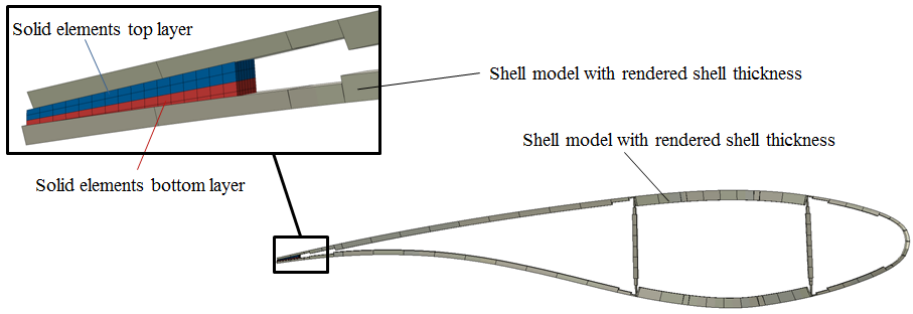

Figure C.2: Wind turbine blade model cross section with shell elements and solid elements in the trailing edge. The solid elements are tied to the shell elements with tie-constraints.

All *degrees of freedom* (DOF) in the central node at the blade root were restrained and transferred via a kinematic (rigid) coupling constraint assigned to the nodes at the blade root circumferences. In addition to gravity loading, the blade was loaded force-controlled by means of four axial connector elements (Figure C.3). Four load introduction points (LPs) acted as master nodes for rigidly connected nodes representing the anchor plates at the cap along the suction side. Axial connector elements connected the master nodes of the four individual LPs on the blade with the reference points on the rigid floor (Figure C.4). The connector elements were chosen due to the advantage that the applied force is axially aligned with the connector elements. Thus, the model more realistically represented the experimentally applied loading conditions in conjunction with the large blade deformation.

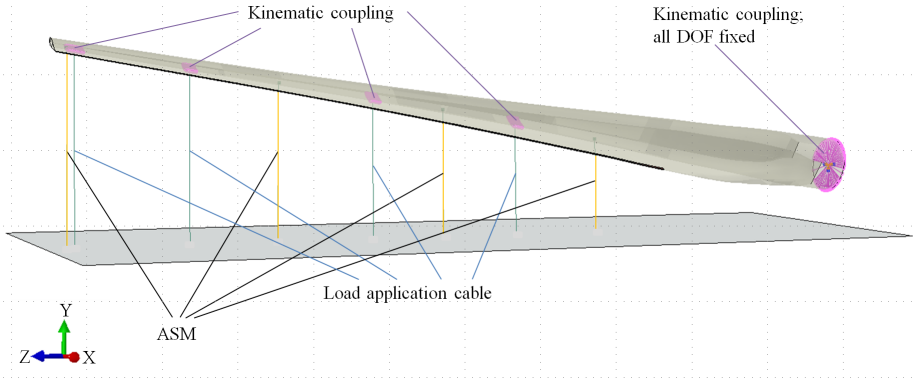

Figure C.3: Boundary conditions of the blade model.

The numerical analysis was performed as a quasi-static geometric non-linear analysis. A dynamic implicit solver was chosen. The loads were slowly ramped up, thus the kinematic energy level could be neglected and a quasi-static performance was reached.

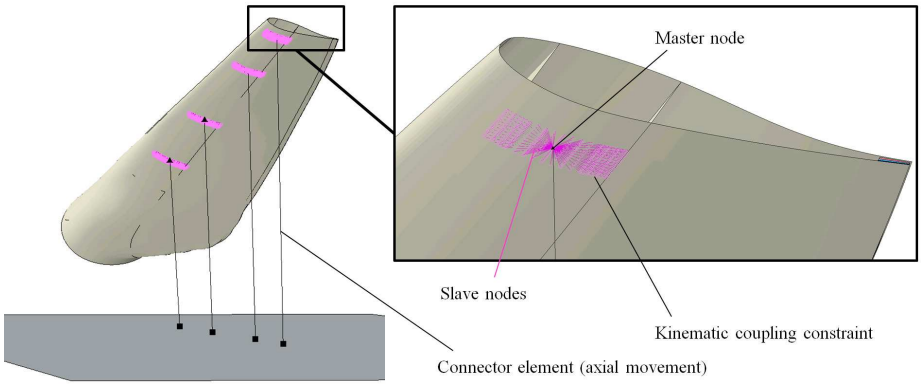

Figure C.4: Kinematic coupling constraints acting as anchor plates and load introduction for the applied transversal forces.

C.3.4 Failure criteria

Different failure criteria and fracture mechanics models were used in order to identify critical strains and stresses and to model progressive damage and failure. Maximum strain, maximum stress, Tsai-Hill, Azzi-Tsai-Hill and Tsai-Wu failure theories were used for the preliminary failure prediction. The Hashin criterion [47, 48, 73, 82] and cohesive element methods [14, 22] were used for more detailed progressive damage and failure simulation. The *Virtual Crack Closure Technique* (VCCT) [27, 69] was used to extract nodal forces and relevant *Strain Energy Release Rates* (SERRs) along the trailing edge.

C.3.4.1 First ply failure criteria

The maximum strain, maximum stress, Tsai-Hill, Azzi-Tsai-Hill and Tsai-Wu failure theories represent strain- and stress-based failure criteria, respectively. These theories post-process stresses or strains from a model and generate an output variable for the individual failure criterion in order to indicate failure (> 1) or no failure (< 1). These failure criteria do not affect the stiffness matrix of the *Finite Element Analysis* (FEA). The maximum strain failure criterion and maximum stress failure criterion are very simple criteria: Failure occurs when any of the strain or stress components in the principal material axes exceed the corresponding critical value. The components are independently judged and the failure envelope is a rectangle. For the maximum strain criteria, an interaction of stresses based on Poisson's effect is given and the failure envelope is a parallelogram.

The Tsai-Hill, Azzi-Tsai-Hill and Tsai-Wu theories are quadratic, orthotropic plane stress failure criteria normally used for fibre-reinforced composite materials. These criteria calculate an equivalent stress and try to consider interactions in a multiaxial stress state. The failure envelopes are ellipses.

C.3.4.2 Progressive damage and failure approaches

The Hashin criterion is a progressive damage and failure theory for unidirectional fibre composite materials with anisotropic behaviour [47, 48]. The progressive failure theory is based on two steps. Firstly, a failure criterion is evaluated for each individual lamina and at each load step. If lamina strain or stress exceeds the critical value, the lamina is considered to have failed, its stiffness is reduced and the entire stiffness matrix has to be recalculated. This progressive damage calculation can be repeated until ultimate failure is reached and the structure fails [73, 82]. In Abaqus the onset of damage is defined by the Hashin and Rotem initiation criteria [47, 48]. Hashin's criterion distinguishes between fibre and matrix failure and whether the stress state is positive or negative. Four different initiation mechanisms are considered: fibre rupture in tension; fibre buckling and kinking in compression; matrix cracking under transverse tension; shearing and matrix crushing under transverse compression and shearing. The initiation criteria are defined as follows:

Fibre tension for $\hat{\sigma}_{11} \geq 0$:

$$F_f^t = \left(\frac{\hat{\sigma}_{11}}{X_t}\right)^2 + \alpha \left(\frac{\hat{\tau}_{12}}{S_l}\right)^2 \tag{C.1}$$

Fibre compression for $\hat{\sigma}_{11} \leq 0$:

$$F_f^c = \left(\frac{\hat{\sigma}_{11}}{X_c}\right)^2 \tag{C.2}$$

Matrix tension for $\hat{\sigma}_{22} \geq 0$:

$$F_m^t = \left(\frac{\hat{\sigma}_{22}}{Y_t}\right)^2 + \left(\frac{\hat{\tau}_{12}}{S_l}\right)^2 \tag{C.3}$$

Matrix compression for $\hat{\sigma}_{22} \leq 0$:

$$F_m^c = \left(\frac{\hat{\sigma}_{22}}{2S_t}\right)^2 + \left[\left(\frac{Y_c}{2S_t}\right)^2 - 1\right] \frac{\hat{\sigma}_{22}}{Y_c} + \left(\frac{\hat{\tau}_{12}}{S_l}\right)^2 \tag{C.4}$$

with longitudinal tensile strength X_t, longitudinal compressive strength X_c, transverse tensile strength Y_t, transverse compressive strength Y_c, longitudinal

shear strength S_l and transverse shear strength S_t. α is a coefficient that determines the contribution of the shear stress to the fibre tensile initiation criterion and $\hat{\sigma}_{11}$, $\hat{\sigma}_{22}$ and $\hat{\tau}_{12}$ are components of the effective stress tensor $\hat{\sigma}$. Depending on the settings, the initiation criteria can be adapted in order to obtain the model proposed in Hashin and Rotem [48] by setting $\alpha = 0.0$ and $S_t = Y_c/2$, or the model proposed in Hashin [47] by setting $\alpha = 1.0$ [27]. In the current study the parameter α was set to 1.0 to account for the contribution of the shear stress to the fibre tensile initiation criterion.

The failure surface is expressed in the effective stress space $\hat{\sigma}$. The effective stress tensor $\hat{\sigma}$ is the product of the true stress (σ) and the damage operator M. The effective stress tensor $\hat{\sigma}$ is intended to represent the stress, which effectively resists the internal forces (see Equation C.5)[27].

$$\hat{\sigma} = M\sigma \tag{C.5}$$

where M is defined as

$$M = \begin{bmatrix} \frac{1}{(1-d_f)} & 0 & 0 \\ 0 & \frac{1}{(1-d_m)} & 0 \\ 0 & 0 & \frac{1}{(1-d_s)} \end{bmatrix} \tag{C.6}$$

with the internal damage variables (d_f, d_m and d_s) characterizing fibre, matrix and in-plane shear damage [27]. The damage variable for a particular mode is given by the following expression and is active after damage initiation, when $\delta_{eq} \geq \delta^0_{eq}$.

$$d = \frac{\delta^f_{eq}\left(\delta_{eq} - \delta^0_{eq}\right)}{\delta_{eq}\left(\delta^f_{eq} - \delta^0_{eq}\right)} \tag{C.7}$$

where δ^0_{eq} is the initial equivalent displacement at which the initiation criterion for that mode was met, and δ^f_{eq} is the displacement at which the material is completely damaged in this failure mode [27].

Up to damage initiation the material behaviour is assumed to be linearly elastic and so is the stiffness matrix of the orthotropic material. After damage initiation the material response is computed from

$$\sigma = C_d\epsilon \tag{C.8}$$

where ϵ is the strain and C_d is the damage elasticity matrix, which has the form

$$C_d = \frac{1}{D}\begin{bmatrix} (1-d_f)\,E_{11} & (1-d_f)\,(1-d_m)\,\nu_{21}E_{11} & 0 \\ (1-d_f)\,(1-d_m)\,\nu_{12}E_{22} & (1-d_f)\,E_{22} & 0 \\ 0 & 0 & (1-d_s)\,G_{12}D \end{bmatrix} \tag{C.9}$$

where $D = 1-(1-d_f)\,(1-d_m)\,\nu_{12}\nu_{21}$, E_{11} is the longitudinal modulus and E_{22} the transverse modulus, ν_{12} reflects Poisson's ratio and G_{12} the shear modulus [27]. For the failure analyses, the material properties given in Table 2 were used. The fracture energies for all laminates were set to $1200\,\mathrm{J\,m^{-2}}$ for Mode I and $4000\,\mathrm{J\,m^{-2}}$ for Modes II and III according to [71].

Surface-based cohesive behaviour was used to model damage initiation and evolution. Surface-based cohesive behaviour allows simulating debonding processes of interfaces. The approach allows crack growth and debonding of the adhesive bondline at the trailing edge. The cohesive behavior is based on a linear elastic traction-separation law as shown in Figure C.5(a). The bondline material properties of the adhesive were assumed as follows: The interfacial strengths τ_{normal} = 7.5MPa, τ_{shear}= 15MPa and the critical energy release rates (G_{ic}) with $G_{Ic} = 700J/m^2$, $G_{IIc} = G_{IIIc} = 1000J/m^2$. The interfacial strength and critical energy release rates are based on results from Eder and Bitsche [30]. Furthermore, Eder and Bitsche [30] showed an ultrasound scan of the bondline for the same blade type with many entrapped air bubbles and badly bonded areas. The ultrasound scan of the adhesive trailing edge joint is reproduced in Figure C.5(b). The dark areas highlight locations with high damping ratios, usually caused by air layers, which indicate poorly bonded or even unbonded regions [30]. The low interfacial strength and SERR compared to results published in [71] were considered in order to take account of expected flaws in the bondline.

C.3.5 Wave extraction technique

In order to separate the local trailing edge wave deformation from the global deformation a polynomial function was used. A polynomial given by Equation C.10 was found to represent the numerically obtained global trailing edge deformation between 7.0 m and 29.5 m.

$$u_y(z) = a_0z^5 + a_1z^4 + a_2z^3 + a_3z^2 + a_4z + a_5 \tag{C.10}$$

where the curve fitting constants are a_i and the lengthwise positions measured from the root are represented by z. The wave extraction methods could also

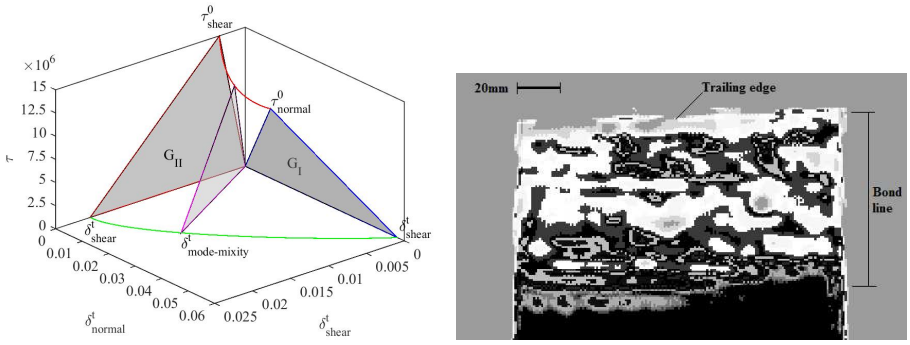

(a) (b)

Figure C.5: (a) Illustration of mixed-mode response of the cohesive surface based on a linear traction-separation law. (b) Inverted dB ultrasound scan image of a trailing edge slice (Figure (b) is taken from Eder and Bitsche [30]).

Table C.2: Material properties as specified by the manufacturer: allowable tensile strain $\epsilon_{tensile}$, allowable compressive strain $\epsilon_{compressive}$, allowable shear strain ϵ_{shear}.

Engineering constants	*U/D glass*	*Triaxial glass*	*Triaxial glass HRC*	*Biaxial glass*	*Biaxial pre-preg*	*Polymer foam*	*Units*
E_{11}	41.26	20.26	16.70	12.75	11.58	0.0485	GPa
E_{22}	11.39	10.42	8.587	12.75	11.58	0.0485	GPa
ν_{12}	0.33	0.50	0.50	0.50	0.50	0.40	-
G_{12}	3.91	7.35	6.605	10.06	10.06	0.0391	GPa
$\epsilon_{tensile}$	0.021	0.023	0.023	0.017	0.011	-	-
$\epsilon_{compressive}$	0.016	0.012	0.016	0.015	0.014	-	-
ϵ_{shear}	0.0037	0.014	0.014	0.014	0.014	-	-
X^T	903.60	472.06	389.04	214.20	123.91	1.4	MPa
X^C	660.16	324.16	267.15	184.88	156.33	1.3	MPa
Y^T	42.14	127.12	104.76	184.88	156.33	1.4	MPa
Y^C	42.14	127.12	104.76	184.88	156.33	1.3	MPa
S^L	58.65	99.25	89.17	143.91	143.91	1.1	MPa
S^T	58.65	99.25	89.17	143.91	143.91	1.1	MPa
ρ	1931	1864	1683	1894	1890	80	kg/m^3

have been based on other curve-fitting methods, e.g. a simple power fit curve or lower order polynomial functions and would not affect the outcome significantly.

At low load levels the trailing edge wave was imperceptible, and the fifth order

polynomial equation represented the base deformation of the trailing edge in absence of the wave. Also for higher loads this approach was assumed to be applicable since the numerical model provided many data points along the entire trailing edge and only a relatively small section of the trailing edge was underlay significant local wave formation amplitudes. Thus, the data point in the area of the local wave will not significantly affect the global trend of the fifth order polynomial used for the wave extraction approach. The fitting constants were obtained in Matlab [81] by a least squares method. The local wave deformation was obtained by subtracting the curve fit of the trailing edge deformation represented by Equation C.10 from the measured or numerically predicted trailing edge displacements.

C.4 Results

C.4.1 Aero-elastic loads and ultimate load

The *Maximum Design Load* (MDL) is based on conducted aero-elastic simulations and represents the maximum load for a specific angular direction including the corresponding safety factor. The design load is applied as shown in Figure C.1. Its bending moment distribution and magnitude correspond to approximately 90% of the experimentally found *Ultimate Load* (UL), defined as the load under which the blade during experiment failed. Figure C.6(a) shows the corresponding load levels normalised to 1.

Before conducting an ultimate blade test, the blade was loaded up to approximately 75 % of the UL. The test results were used to validate the accuracy of the numerical blade model. The global blade response, measured by means of the ASM installed at radial positions of z=10 m, z=16 m, z=22 m and z=29 m, was compared to numerical results. The comparison showed an excellent agreement between the numerical and experimental results as shown in Figure C.6(b) and Table C.3. The maximum deviation for the global displacement was less than 2% at the blade tip.

Table C.3: Experimental (ASMs) and numerically obtained global deformation at 76% of the UL.

	z=29.5	z=22.0 m	z=16.0 m	z=10.0 m	Unit
ASM	-1.914	-0.7974	-0.307	-0.102	m
Numeric	-1.880	-0.8023	-0.311	-0.102	m
Rel. Error	-1.77	0.62	1.38	0.00	%

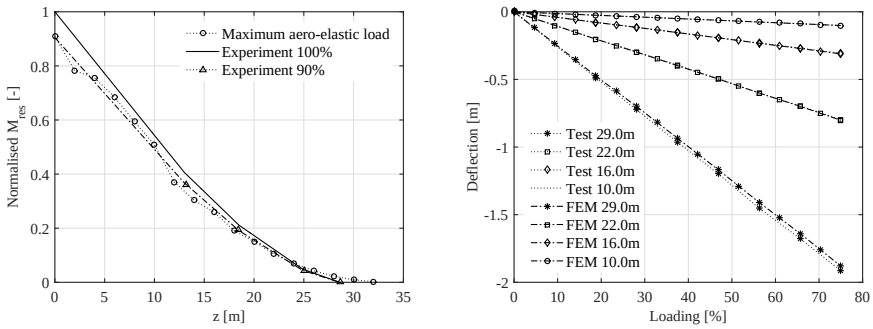

(a) (b)

Figure C.6: (a) Comparison between experimentally applied bending moments and the designated maximum design load determined by aero-elastic load analyses. (b) Comparison between experimentally measured displacements by means of ASM and numerical results.

The experimental data of the global blade response is compared to numerical data with and without progressive damage mechanics modelled (Figures C.7(a) and C.7(b)). The comparisons showed good agreement. For the non-linear numerical model without progressive damage mechanics, the results for the global displacements measured at $z = 29.0\,\mathrm{m}$ and $z = 22.0\,\mathrm{m}$ deviated more from the experimental results than the model including progressive damage mechanics as shown in Table C.4. The numerical model including progressive damage mechanics modelling shows bigger relative error towards the root for measurements taken at $z = 16.0\,\mathrm{m}$ and $z = 10.0\,\mathrm{m}$. These results are sound, since the progressive damage mechanics modelling weakens the structural stiffness in the failure region. Thus a weaker structural response towards the blade tip occurs and less load is transferred towards the blade root. Consequently, the displacement at these locations is less than for the model without progressive damage mechanics. Furthermore, the relative error for the numerical model with progressive damage mechanics modelling towards the root is higher than for the model without progressive damage mechanics modelling. However, the measured absolute displacements at $z = 16.0\,\mathrm{m}$ and $z = 10.0\,\mathrm{m}$ is very small, hence little absolute deviation leads to higher relative error compared to measurements taken closer towards the blade tip.

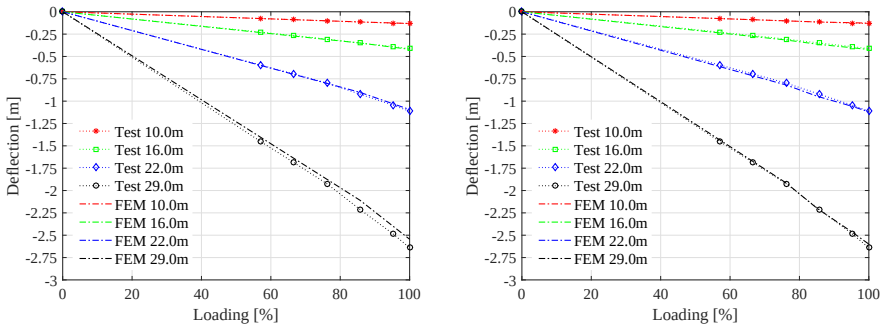

Figure C.7: (a) Global displacement test data compared with numerical results for simulations without progressive damage mechanics modelling and (b) including progressive damage mechanics modelling.

Table C.4: Experimental (ASMs) and numerically obtained global deformation at 100% of the UL just before failure. The numerical models with Hashin and without Hashin progressive damage mechanics modelling are compared to the experimental results.

	z=29.5	z=22.0 m	z=16.0 m	z=10.0 m	Unit
ASM	-2.641	-1.113	-0.412	-0.132	m
Numeric without Hashin	-2.545	-1.094	-0.420	-0.131	m
Rel. Error	-3.63	1.70	1.94	0.76	%
Numeric with Hashin	-2.600	-1.119	-0.422	-0.127	m
Rel. Error	-1.55	0.53	2.43	3.48	%

C.4.2 Simulation results without progressive damage mechanics

In Figure C.8(a) the global displacement of the trailing edge measured with the optical displacement measurement camera system between the radial position of 12 m to 16 m is plotted in comparison to numerically predicted displacements. The onset of non-linear geometric deformation of the trailing edge can clearly be seen when the load level reaches 76 % of the ultimate load. In order to visualize the buckling onset, a 5th order polynomial curve fit following the global displacement of the entire trailing edge is plotted as a dashed line for the numerical results. Subtracting the global displacement from the course of the 5th order polynomial curve fit led to the Δu_y shown in Figure C.8(b). The local

trailing edge deformation showed a distinct increase in magnitude when the load was raised from 67 % to 76 %. Here, the numerical prediction differed from the experimentally gained data. The numerical model underestimated the magnitude of the buckling wave significantly. The prediction of the local trailing edge deformation differed also from the measured displacement depending on the load level. For the experimentally obtained displacement, the buckling wave was moving slightly towards the blade tip with increasing load level. The opposite occurred for the numerical prediction, where the local wave moved towards the root. This means that even though the position of the buckling wave agrees well at low load level, this was not the case at higher load level where they move further apart.

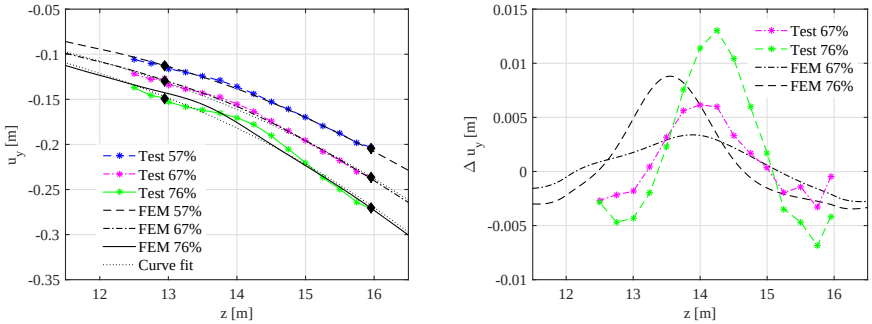

Figure C.8: (a) Comparison at different load levels of measured trailing edge displacement Δu_y of marker points and numerical displacement results. (b) Comparison of local deformation as offset from a curve fit through the global displacement.

With increasing load level the buckling wave formation became more distinct as shown in Figures C.9(a) and C.9(b). For higher loads the position of the local buckling wave moved very little in both cases towards the root. In general, the numerical simulation differed from the experimental results in buckling peak location and buckle wave magnitude. The formation of buckling waves started at lower a load level in the tests than in the numerical analyses and the magnitude of the buckling waves also became more pronounced at lower a load level in the test. The magnitudes of the numerical model were less marked compared to the measured local deformation. Moreover, the position where the local deformation peaked was offset by approximately 1 m in radial position at UL.

The reason for the differences in magnitude was due to damage onset near the

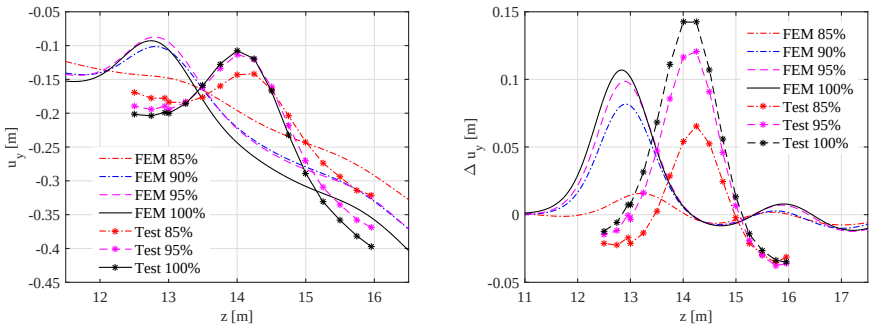

(a) (b)

Figure C.9: (a) Comparison of measured trailing edge displacement u_y of marker points and numerical displacement results. (b) Comparison of local deformation as offset from a curve fit through the global displacement.

trailing edge that occurred during the experimental testing. The trailing edge buckling caused failure in the sandwich panel on the pressure side of the blade between the load-carrying girder and the trailing edge. In the numerical model without progressive damage and failure implementation, the damage was predicted but had no stiffness degradation effects on the structure. The experiments showed a distinct kink in the trailing edge panel on the pressure side whereas the model showed high stresses but no kink in the trailing edge panel. With increased load the kink became more distinct as shown in Figure C.10.

Figure C.10: Trailing edge deformation just before reaching the ultimate load. Note the distinct kink at the upper surface (pressure side).

C.4.3 Failure criteria

The non-linear simulations without progressive damage mechanics predicted ply failure for load levels between 90 % and 100 % of the UL, while the sandwich core started to fail at a load level of 89 %. Shear failure where the shear stress τ_{23} exceeded S^T was predicted in the sandwich structure forming the trailing edge panel in the vicinity of the buckled trailing edge. Depending on the applied failure criterion, the failure was predicted for different load levels as given in Table C.5. The stress-based failure theories were more conservative than the Maximum strain criterion. The Maximum strain criterion predicted failure of the sandwich panel at a load level of 100%. At this load stage the sandwich construction near the trailing edge of the experimentally tested blade had already failed. Thus, the strain failure criteria seems not to reveal the failure mode early enough. The reason for the inaccurate failure prediction could be based on inappropriate critical strain values, since no strain data based on coupon test results were available. Therefore, no further investigation of the inaccuracy of the maximum strain failure criterion is performed.

Table C.5: Failure criteria and referring load level.

Failure criterion [-]	Tsai-Wu	Tsai-Hill	Azzi-Tsai-Hill	Max stress	Max strain
Load level [%]	90	95	95	95	100

The area where failure occurred was locally exposed to compressive stresses ($\sigma_{11} < 0$ and $\sigma_{22} < 0$). It is thus excepted that the Azzi-Tsai-Hill and Tsai-Hill failure criteria predict exactly the same results because both failure theories vary only in the definition of the interaction terms ($\sigma_{11} \cdot \sigma_{22}$), which leads to differences in the second and fourth quadrants of the failure envelopes (Equations C.11 and C.12). This means that differences between both criteria appear only when σ_{11} and σ_{22} have opposite signs.

$$I_{F\ Hill} = \frac{\sigma_{11}^2}{X^2} - \frac{\sigma_{11} \cdot \sigma_{22}}{X^2} + \frac{\sigma_{22}^2}{Y^2} + \frac{\sigma_{12}^2}{S^2} < 1.0 \tag{C.11}$$

$$I_{F\ Azzi} = \frac{\sigma_{11}^2}{X^2} - \frac{|\sigma_{11} \cdot \sigma_{22}|}{X^2} + \frac{\sigma_{22}^2}{Y^2} + \frac{\sigma_{12}^2}{S^2} < 1.0 \tag{C.12}$$

where if $\sigma_{11} >= 0$, the structure is exposed to tensile stress in longitudinal direction and the longitudinal tensile strength will be used as reference strength($X = X_t$); otherwise the longitudinal compressive strength is $X = X_c$. The same principle applies for the transverse stress if $\sigma_{22} >= 0, Y = Y_t$ other-

wise $Y = Y_c$.

The Max stress, Tsai-Hill and Azzi Tsai-Hill criteria predicted ply failure in the outermost ply consisting of triax glass fabric around a load level of 95%. Even though the failure criteria were developed for unidirectional fibre composites, they can be applied to triax materials as long as the strength data measured directly for a triax mat laminate is used as investigated by Laustens et al. in [76].

The Tsai-Wu failure criterion was the only one to predict ply failure in the second layer (biaxial glass pre-preg material) of the sandwich panel. According to the Tsai-Wu criterion, the stress state in the second layer exceeds the failure index locally at a load level of approximately 90% . Thus the Tsai-Wu criterion was the most conservative one and can be explained by looking at the failure envelopes for the different criteria (Figures C.11(a) and C.11(b)). The failure surfaces of the Tsai-Wu theory (Equation C.13) are in both figures ellipsoidal. The extreme points of the ellipsoids intersect the principal axes. This means that no coupling of the interaction terms (given in Equation C.19) was considered and the ellipsoids were not turned around the τ_{12}-axis. Without considering the interaction term the ply stress states for the biax and triax layers exceed the critical stresses and lie outside the Tsai-Wu failure surface but inside the Tsai-Hill failure surface, as shown in Figures C.11(a) and C.11(b)). Figure C.11(a) shows the significant differences in failure assumption for the various failure criteria for the biaxial pre-preg. Figure C.11(b) shows that the differences between the criteria are less distinct for the triaxial glass fabric.

$$I_{F\ Wu} = F_1\sigma_{11} + F_2\sigma_{22} + F_{11}\sigma_{11}^2 + F_{22}\sigma_{22}^2 + F_{66}\sigma_{12}^2 + 2F_{12}\sigma_{11}\sigma_{22} < 1.0 \tag{C.13}$$

with the Tsai-Wu coefficients defined as follows:

$$F_1 = \frac{1}{X_t} + \frac{1}{X_c} \tag{C.14}$$

$$F_2 = \frac{1}{Y_t} + \frac{1}{Y_c} \tag{C.15}$$

$$F_{11} = -\frac{1}{X_t X_c} \tag{C.16}$$

$$F_{22} = -\frac{1}{Y_t Y_c} \tag{C.17}$$

$$F_{66} = \frac{1}{S^2} \tag{C.18}$$

$$F_{12} = f^* \sqrt{F_{11} F_{22}} \tag{C.19}$$

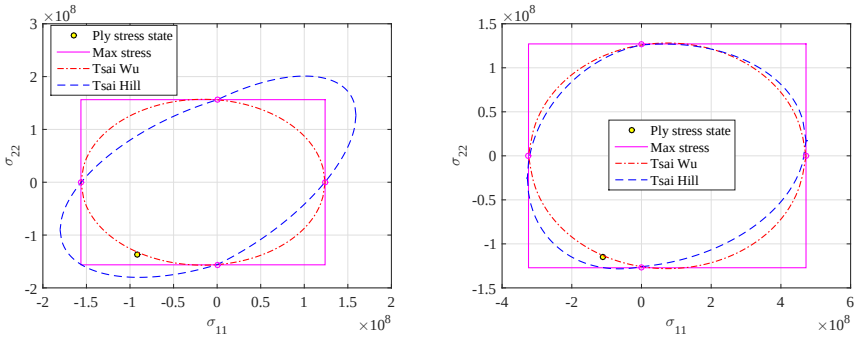

Figure C.11: Failure criteria and ply stress state in the area of highest stress concentration in the sandwich panel at a load level of 90 %. (a) Failure envelopes for the biaxial pre-preg ply. (b) Failure envelopes for a ply of the triaxial glass fabric, where σ_{11} describe the longitudinal direction of the material.

where f^* is a scalar within the range $-1.0 \leq f^* \leq 1.0$. Since no other material data for the lamina than that given in Table C.2 were available, $f^* = 0$ was used for the simulations. Setting $f^* = 0$ eliminates any stress interaction in Equation C.13. The scalar f^* affects the failure envelop significantly and becomes an essential variable for the curve-fitting strength criterion. For biaxial stress states or multiaxial stresses, the failure envelope in 2D and 3D can be modified. For example by setting the scalar to $f^* = -0.45$, the ellipsoid rotates around the τ_{12}-axes (Figure C.12) and a failure envelope similar to those of the quadratic Tsai-Hill can be generated (see Figures C.13(a) and C.13(b)). In those cases, none of the stress-based failure theories would have predicted failure at this load stage since the state of stress would have been within the failure surface and thus the failure index $I_F < 1.0$. This analysis made clear that F_{12} is a very sensitive and critical quantity in the Tsai-Wu criteria and must be handled with great care by users as described by Tsai and Wu [119].

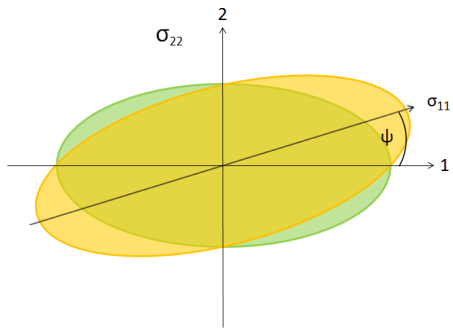

Figure C.12: Projection of the ellipsoid on the σ_{11} - σ_{22} plain with a rotation (rotation angle = ψ) around the τ_{12}-axis.

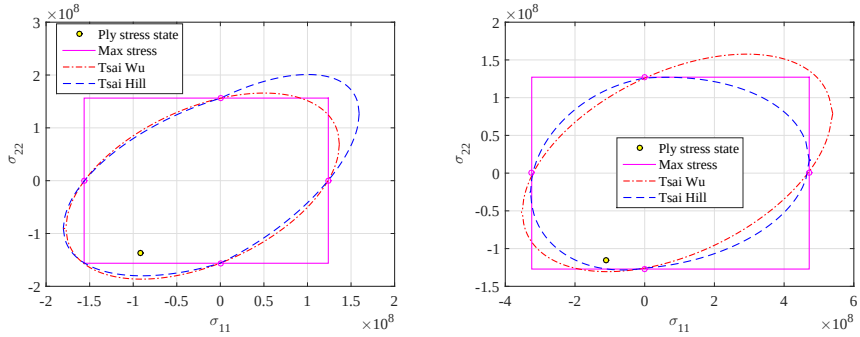

Figure C.13: Failure criteria and ply stress state in the area of highest stress concentration in the sandwich panel at a load level of 90 %. (a) Failure envelopes for the biaxial pre-preg ply with $f^* = -0.45$. (b) Failure envelopes for a ply of triaxial glass fabric with $f^* = -0.45$.

C.4.4 Core shear failure

The numerical analysis showed that the trailing edge buckle caused damage in the sandwich composite panel on the pressure side. The sandwich panel forming the pressure side shell was bent and exposed to compression when the sandwich panel started to kink. The load configuration in the region of the kinked sandwich composite panel showed high shear stresses. The occurring

shear stress exceeded the critical shear stress level of the sandwich panels, which in consequence led to a failure mode called core shear failure, as shown in Figure C.14. Originally all ply failure criteria predicted failure in the outermost plies and did not consider the failure origination in the core material. The von Mises equivalent stress criterion likewise did not reveal the core shear failure, since τ_{23} was the driving shear stress, and not considered in the implemented von Mises stress criterion for plane stress.

Although classical shell theory does not allow the calculation of out-of-plane stresses, the uses of Abaqus' 8-node double curved thick shell elements with reduced integration (S8R) based on Mindlin-Reissner theory enables the estimation of the transverse shear stresses at section integration points as output variables. The shear stresses τ_{13} and τ_{23} are estimated by matching the elastic strain energy associated with shear deformation of the shell section with that one based on piecewise quadratic variation of the transverse shear stress across the section, while bending around one axis [27]. To account for parabolic shear stress distribution, a shear correction factor is applied. At a load level of approximately 89 %, τ_{23} exceeded the critical shear stress S_T. This finding shows the importance checking out-of-plane shear stress distributions for sandwich composite materials, because none of the applied failure criteria have revealed the shear failure.

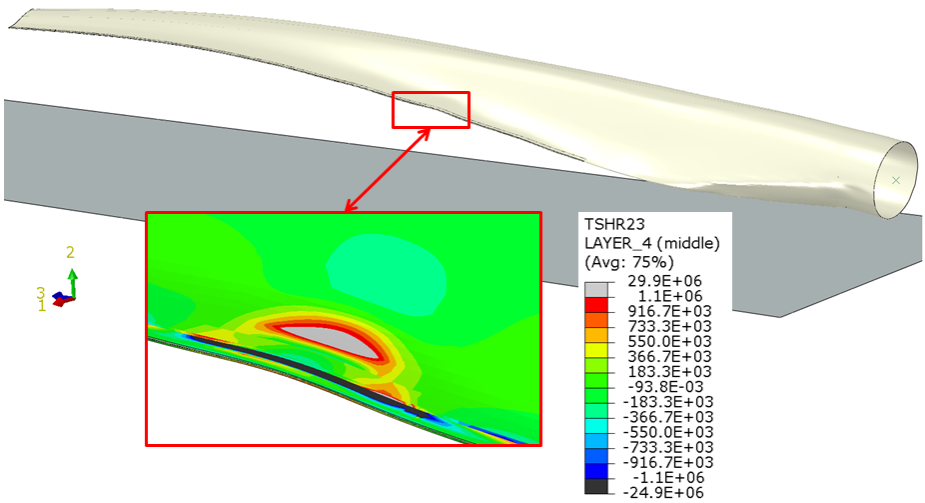

Figure C.14: Core shear failure under out-of-plane shear at a load level of 89%. The color bar indicates the maximum shear stress levels of $\pm$ 1.1 MPa for the core material. The grey area indicates core shear failure by exceeding the value.

C.4.5 Simulation results including progressive damage mechanics

In order to consider the sandwich panel damage and its impact on the blade stiffness, Hashin's progressive damage and failure theory was applied to the blade structure. Hashin's theory predicted at a load level of approximately 85% the initiation of shear and compressive damage and damage propagation in the outer skin layers of the composite material forming the suction side panel as shown in Figure C.15, as well as core material failure initiation and damage propagation under shear and compressive stress. In theory, Abaqus uses the damage variable DAMAGEMC to reveal damage of the matrix under compression for uniaxial composite materials. Damage initiation according to Hashin's failure criterion for matrix compression with $\hat{\sigma}_{22} \leq 0$ is defined as follows:

$$F_m^c = \left(\frac{\hat{\sigma}_{22}}{2S_t}\right)^2 + \left[\left(\frac{Y_c}{2S_t}\right)^2 - 1\right]\frac{\hat{\sigma}_{22}}{Y_c} + \left(\frac{\hat{\tau}_{12}}{S_l}\right)^2 \tag{C.20}$$

where the transverse compressive strength Y_c, the longitudinal shear strength S_l and the transverse shear strength S_t. $\hat{\sigma}_{22}$ and $\hat{\tau}_{12}$ are components of the effective stress tensor $\hat{\sigma}$. In this study, layer 1 is triaxial glass fibre fabric and thus DAMAGEMC indicates failure in transversal direction (orthogonal to the radial blade direction) for the triaxial material instead of matrix failure. Shortly after the first ply failure initiation of the composite skin layer, the core material collapsed under a combination of in-plane shear and compression failure. Although the Hashin failure criterion does not consider out-of-plane shear in its formulation, it captures the weakening effect of the composite structure well.

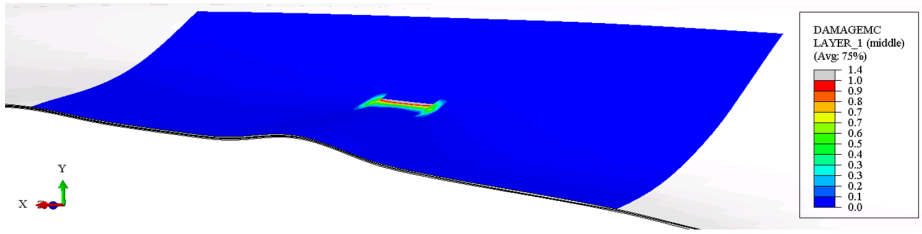

Figure C.15: Hashin's compressive matrix damage critierion. The gray marked area indicates ply failure in the most outer skin layer of the suction side at a load level of 85%.

The applied progressive damage and failure theory affected the response of the

numerical model. The trailing edge deformation became more pronounced in magnitude (Figure C.16(a)). The numerical results now show very good agreement with the magnitude of the measured trailing edge displacement u_y (Figure C.16(a)) and Δu_y as shown in Figure C.16(b).

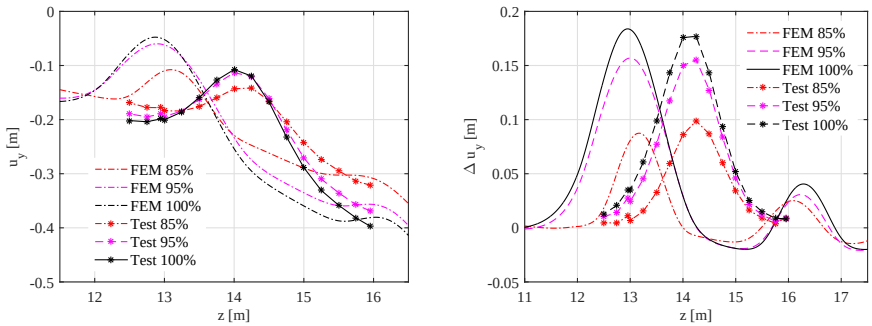

(a) (b)

Figure C.16: (a) Comparison of measured trailing edge displacement u_y of marker points and numerical displacement results. (b) Comparison of local deformation as offset from a curve fit through the global displacement.

The higher the loads, the more prone was the trailing edge buckling and the progressive damage in the sandwich panel grew. According to the numerical simulation, the compressive stress increased and the failure grew in a span-wise direction. The buckling wave significantly affected the local stresses and strains, acting at the bondline and changing this with increase buckling wave magnitude. The stress concentration in the trailing edge increased with increasing load and so did the *Strain Energy Release Rates* (SERRs) as calculated with the following Equations C.21 and C.22:

$$G_{tot} = G_I + G_{II} + G_{III} \tag{C.21}$$

$$G_{equ} = G_{Ic} + (G_{IIc} - G_{Ic}) \cdot \left(\frac{G_{II} + G_{III}}{G_{tot}} \right)^{\lambda} \tag{C.22}$$

where G_{tot} is the total energy, G_I, G_{II} and G_{III} are the strain energy release rates for Modes I, II and III, respectively. G_{ic} determines the critical energy release rates and G_{equ} is the equivalent energy release rate calculated according to the Benzenggagh-Kenane law [14]. The exponent λ describes the interaction

between the mode-mixity and depends on the resin type (λ= 2 for brittle resins and λ= 3 for ductile resins) [30]. In this study the exponent was set to λ=2.284.

In order to determine the SERRs at the bondline, a small crack in the middle of the adhesive glue was simulated and the SERRs calculated as described in Section C.3.3. The SERRs increased significantly between the load level of approximately 80% to 90%, when sandwich failure occurred near trailing edge. Figures C.17(a), C.17(b) and C.17(c) show the increase for the individual Mode SERR, and Figure C.17(d) shows the total SERR (G_{tot}) in relation to the equivalent SERR (G_{equ}). G_{III} dominated the mode-mixity. The buckled trailing edge had its maximum at a radial position of around 13.29 m. The buckling wave forced the upper and lower trailing edge panels to close and shear stress dominated as described in [44]. The trailing edge buckling suppressed the opening Mode I completely. Mode III flanked the trailing edge buckle peak whereas Mode II peaked around 13.29 m. The highest critical energies (G_{tot}) occurred at 12.75 m and 13.70 m, located approximately 0.5 m on each side of the main wave peak.

In the numerical prediction, according to VCCT the critical energy release rate at the crack tip was already exceeded at a load level of 90%. However, VCCT was only used to extract the SERRs but not to model crack propagation. A cohesive surface approach was used to model the crack propagation. Here, crack growth of the adhesive joint started with crack growth on the inner side and grew steadily, proportional to the load increase. In the numerical prediction the critical damage initiation stress is met at a load level of 85% of the experimentally determined ultimate load, and damage initiation started in the trailing edge bondline. At that load stage, the total energy level was not high enough – as shown in Figure C.17(d) – and the crack did not grow. Only a small initial crack measuring a few millimetres appeared, and did not separate the bondline. With increasing load, at load level 94% the energy level was high enough for crack evolution (Figure C.18(a)). At load level 95% the crack propagated and the energy in the trailing edge G_{equ} exceeded the critical energy level G_c, which led to trailing edge failure (Figures C.18(c) and C.18(d)). In the simulation, stable crack growth occurred, which means that it needed additional external energy in order to grow. In contrast, the experiments showed clearly unstable crack growth, where the bondline along the trailing edge was suddenly opened by the released energy for a length of several meters.

The highest critical SERRs according to Figure C.17(d) were those that flanked the buckling peak, and adhesive failure was expected to initially occur there. The numerically predicted bondline failure agrees with the location predicted by VCCT of the highest SERRs, and showed crack growth initiation around 12.75 m. Later on in the crack propagation process, the two crack fronts combine around 12.75 m and 13.50 m as shown in Figures C.18(a) to C.18(d).

Blade failure and trailing edge separation were recorded with a high speed camera during the test. Figures C.19(a) to C.19(d) show the crack propagation in

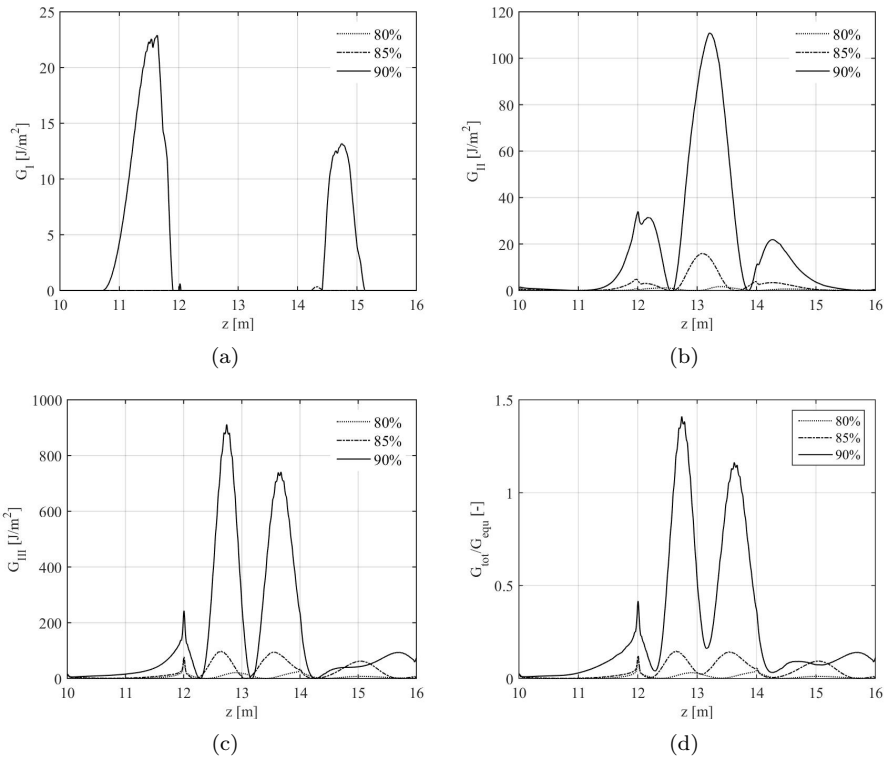

Figure C.17: (a) SERR distributions for Mode I under the experimental loading condition. (b) SERR distributions for Mode II under the experimental loading condition. (c) SERR distributions for Mode III under the experimental loading condition and (d) the corresponding G_{tot}/G_{equ} plot.

sequences of less than a second. The crack started around a radial position of z=14 m and grew along the blade span. The sequences show that the bondline failure started near the trailing edge buckle as numerically predicted. Divergent from the numerical simulation was the location of the experimentally observed origin of trailing edge failure. In the test the failure originated on the left-hand side of the buckle and propagated towards the blade tip. Furthermore, Figures C.19(a) to C.19(d) show that the trailing edge face sheets separated from the adhesive bondline instead of having a crack running through its middle, as numerically modelled.

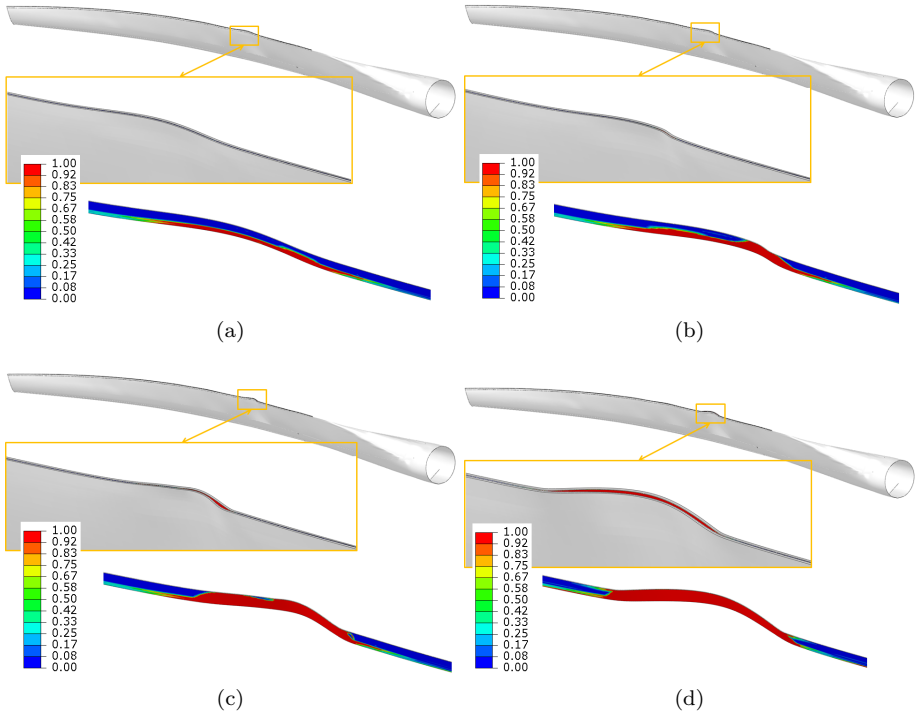

Figure C.18: Sequences of the modelled trailing edge failure damage onset for load levels of (a)=93 % and (b)=94 % before trailing edge separation occurs (c)=97 % and at (d)=100 %. The colour bar indicates the damage variable d as defined in Equation C.7. The bondline elements are shown separately in order to visualise the crack initiation and propagation of the bondline simulated with cohesive elements.

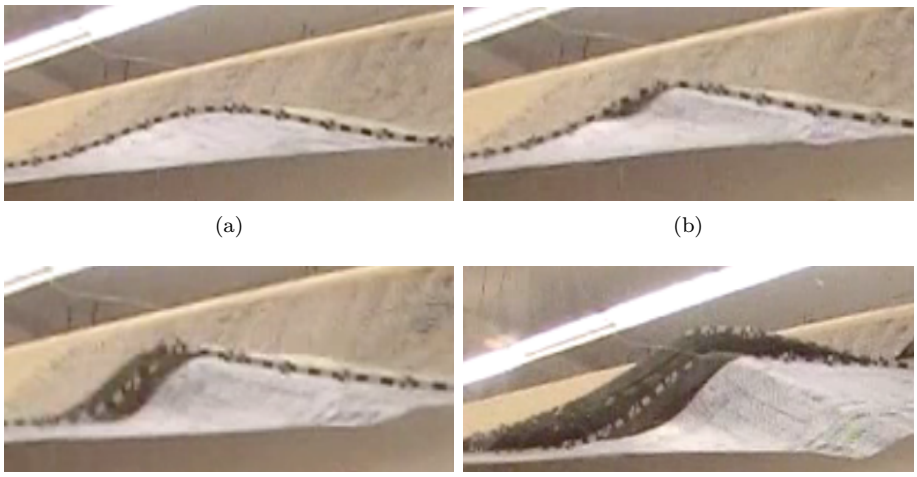

(a) (b)

(c) (d)

Figure C.19: (a) Sequence of the trailing edge failure just before trailing edge separation, (b) in the beginning of the trailing edge separation, (c) at the opening sequence of the trailing edge failure and (d) subsequently sequence with increased separation.

C.5 Discussion and conclusion

The study showed how the interaction between trailing edge buckling and sandwich panel failure led to blade failure. The investigation showed clearly that the trailing edge for the tested load direction was prone to buckle. According to the numerical simulations, the trailing edge deformation led to core shear failure near the trailing edge. The trailing edge failure again greatly decreased the structural stability until ultimate failure, due to the sudden debonding of the trailing edge bondline which caused significant stiffness loss.

The simulations without progressive damage mechanics modelling accurately predicted the blade response prior to failure. The global blade response was in good agreement with the results obtained experimentally. The modelling approach enabled to identify the core shear failure in the sandwich panel but deviated in the prediction of trailing edge deformation magnitude compared to the experimental data, because it did not account for shear core failure onset. The reason for the deviation in the numerical prediction is obvious, since no stiffness degradation was modelled. The use of Hashin's progressive damage and failure theory improved the numerically predicted results compared to the experimental obtained trailing edge deformation measurements, although the plane stress method is not able to identify sandwich out-of-plane shear failure. Hashin's failure criteria predicted a combination between in-plane shear and compressive stress failure, whereas out-of-plane shear probably caused the core failure. However, the chosen numerical modelling approach – including progressive damage mechanics modelling – accurately predicted trailing edge deformation by revealing the weakening effect of the failed composite sandwich structure due to a decrease in blade stiffness.

The use of Hashin's degradation progressive damage and failure theory was computationally expensive and was applied only to clarify the entire fracture process that occurred during testing. This computationally costly method was not needed to predict failure in this case, since the sandwich panel damage was a successive failure caused by prone trailing edge buckling with subsequent shear core failure. However, it is interesting to see that the trailing edge buckling initiated sandwich failure at a distance of approximately 0.58 m from the trailing edge, which then again increased trailing edge buckling and led to failure. For other designs it can be imagined that failure would be predicted only if progressive damage was included in the analysis.

In any event, trailing edge buckling as a local stability problem should be considered as the primary failure mechanism. However, the failure sequence and series of events clearly demonstrates the importance of geometrically non-linear, comprehensive simulations. The occurrence of trailing edge deformation led to sandwich core failure at a load level below the design load and thus showed the

importance of running geometrical non-linear, 3D simulation in order to identify these phenomena. Linear elastic simulations and simplified FEA – as mentioned in Section C.2 – will not reveal the series of events and its consequences.

The work demonstrated how the combined load led to trailing edge buckling at early load levels. At a load level of approximately 75%, the first buckling-like behaviour became visible. Strongly connected to the buckling wave was the significant increase of the energy release rate in the trailing edge joint, as shown for higher load levels.

Apart from the good agreement between the Hashin failure prediction in comparison to the experimental data, the study clearly demonstrated the limitation of in-plane, first-ply-failure criteria with regard to pure laminated composite materials in its inability to reveal core shear failure in the sandwich structure. Furthermore, the study showed the importance of shear stress analysis for sandwich construction.

The used model was subjected to some restrictions, which may have influenced the final blade failure prediction. Firstly, progressive damage growth was implemented only for elements on the pressure side and not applied to the blade suction side. This limitation was made in order to save computational time and because no damage was observed in the test to failure on the suction side prior to final failure. Secondly, crack growth in the trailing edge was limited to the middle of the bondline. An investigation of the stress concentrations and thus crack initiation starting at the interface between adhesive bondline and composite shells would have been relevant to study and might have led to other results. However, the simplified modelling approach was chosen in order to concentrate on the ultimate failure prediction ability of shell and solid elements in the trailing edge. A higher geometric fidelity of the modelled trailing edge based purely on solid elements might lead to more realistic crack propagations, but would require detailed modelling and would not be aligned with the aim of the study. Moreover, in the experimentally conducted ultimate test, cracks along the trailing edge were observed to occur on both sides of the adhesive bond as interfacial/adhesive fracture (Figure C.20(a)) but also propagated through the middle of the bondline as cohesive fracture (Figure C.20(b)).

Another simplification was made regarding the connection between the trailing edge panels modelled with shell elements and the adhesive bondline discretised with solid brick elements. Here, tie constraints were used to couple the shell elements with its six *degrees of freedom* (DOF) and brick elements with only three DOF (no rotational DOF). This modelling strategy does not mathematically fully agree with the theory of shell and solid elements but had no significant impact on the numerical results, as pre-test of different trailing edge simulations showed. It seems as the automatically applied moment to the shell elements accounting for the offset of the MPC leads to a correct body rotation.

As shown in the result section, there is a mismatch between the numerical and experimental locations of the local trailing edge wave. This deviation could have been caused by small imperfections in the trailing edge, to which this part of the blade is highly sensitive to as sensitivity studies have shown. No scan of the real blade shape and especially the trailing edge were conducted and consequently no imperfections were applied to the numerical model. However, sensitivity studies of the impact of trailing edge imperfection on the buckling wave have shown that small imperfections of only 1 mm are sufficient to move the buckling wave along the trailing edge and to match the numerical result with the experimental result. The high sensitivity to imperfections described in this work as well as the series of events leading to failure, should stimulate blade manufacturer to improve their blade design and manufacturing accuracy. It could therefore be beneficial to consider designing blades that are less sensitive to manufacturing imperfections and to ensure manufacturing quality in critical areas.

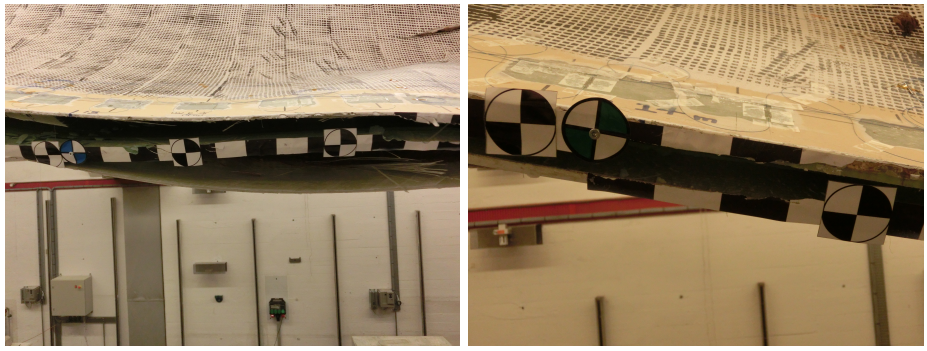

(a) (b)

Figure C.20: Trailing edge opening after blade failure. (a) Trailing edge separation from the bondline and (b) cracked bondline.

Acknowledgement

The work is supported by the new Danish Centre for Composite Structures and Materials for Wind Turbines (DCCSM), grant no. 09-067212 from the Danish Strategic Research Council. The support is gratefully acknowledged. The work is furthermore partly supported by the Danish Energy Agency through the Energy Technology Development and Demonstration Program (EUDP 2010), grant no. 64011-0006. The supported project is named "Experimental Blade Research Phase 2", and the financial support was greatly appreciated.

The authors wish to especially thank Martin A. Eder and Federico Belloni for conducting the experimental blade test and kindly providing the experimental data. Moreover, the authors are grateful for help from the Aeroelastic Design group at DTU Wind Energy for their support of the aero-elastic calculations.

Paper D

The effect of multiaxial loading on a wind turbine rotor blade

---

Article status: Preliminary draft - to be submitted.

Article title: *The effect of multiaxial loading on a wind turbine rotor blade*

Authors: P.U. Haselbach, P. Berring and T. Kim

Journal title: Wind Energy

D.1 Abstract

In this study the effect of multiaxial loading on a 34 m wind turbine rotor blade was investigated. For this purpose, a method to evaluate wind turbine blade failure based on a 3D load envelope was introduced with the purpose to reduce the amount of aeroelastic simulations necessary to run during the iterative design process.

From the preliminary results, it can be concluded that for similar torsional moments the ultimate strength predictions seems to be similar. In cases where the torsional moment significantly deviates from each other, distinct difference in the ultimate strength assessment can occur. Furthermore, the study demonstrates the importance of simulation tools taking geometrical non-linear deformations into account in order to determine ultimate strength failure based on buckling effects.

D.2 Introduction

Failures in the rotor blade usually lead to a long downtime and are costly to repair. Whereas most of the aggregated downtime per turbine subsystem between 2003 to 2012 could be decreased, rotor blades stayed the same with a little variation in sequence [101]. Annually, 1 % to 3 % of the wind turbines require blade replacements with spikes in the first year and after 5 years [72] which increase the CoE, especially when repair and maintenance has to be done on offshore sites, where blade replacement is approximately six times more costly than for onshore sites [1]. Blade replacements in the first two years of operation are usually the result of manufacturing defects or damages occurring during transport and construction [101]. Inspection reports and technical papers indicate that other kind of failures, like e.g. delaminations, adhesive joint failures, shear web/spar cap failures and trailing edge failures, occur widespread over the operation time [7].

The occurring failures in wind turbine rotor blades show that their root causes have not been understood well enough to sufficiently prevent them. The reason is that the failure types are complex in their origin and result, in part, as an interplay of complex loading conditions, anisotropic material behaviour, complex geometries, faults during the manufacturing process and damages during transportation and/or installation. While improved quality management can ensure reliable manufacturing processes, efforts towards more realistic and improved ultimate strength assessments can rise the quality and reliability of strain and stress predictions.

The load carrying capacity of composite materials in general, and wind tur-

bine structures in particular, are highly dependant on the load direction. To determine the ultimate capacity of wind turbine rotor blades under multiaxial loading, it is important to assume correct loads. According to international standards [112] and guidelines [114], a large number of aeroelastic simulations for different *Design Load Cases* (DLC) is required to compute blade loads. Numerical simulation tools based on the *Blade Element Momentum* (BEM) theory, such as *HAWC2* [49], *Bladed* [17], *FAST* [35] etc., are usually used to perform the load calculations. Usually the minimum and maximum of each load component, three force components (F_x, F_y and F_z) and three moments (M_x, M_y and M_z), and the resultants (F_R and M_R) shall be extracted from the DLC. Following the IEC 61400-1 standard [112], an extreme loading matrix as shown in Figure D.1 shall be used to describe the extreme loading situations. This approach is intended to cover the full range of values for that particular load component [112].

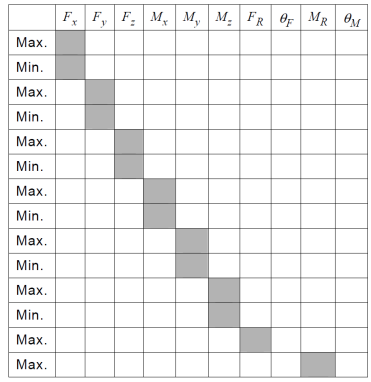

Figure D.1: Extreme loading matrix with three force components (F_x, F_y and F_z) and three moments (M_x, M_y and M_z) and the resultant force vector F_R and its angle θ_F as well as the resultant moment M_R and its angle θ_M (taken from IEC-61400-1 [112]).

The IEC 61400-1 standard requires to conduct detailed strain and stress analyses of the wind turbine structure, exposed to the minimum and maximum of the extreme loads and its contemporaneous values [112].

Blade design is an iterative process, where usually several iterations loops are needed to define an optimal compromise between aerofoil geometry, structural design and aeroelastic response. To safe computational time during the design process, often computational efficient beam analysis codes or linear shell element models are used to predict the strain and stress state. Beam cross sec-

tional analysis codes, e.g. BECAS [18], predict the strain and stress state of single cross sections along the blade span. The advantage, despite of the computational efficiency, of such linear cross sectional analyses is that they define an interface plane which allows the superposition of the acting forces (F_x, F_y, F_z) and moments (M_x, M_y and M_z). Thus, detailed strain and stress states can be predicted for each cross section based on the load components defining the boundary conditions. However, linear analysis neither account for geometrically non-linear deformations, such as cross-section ovalisation [26, 23, 62], nor stability problems (e.g. buckling).

Wind turbine blade structures are hollow and to some extend thin walled shell structures with a highly complex geometry [46]. To reveal realistic failure mechanism and failure modes of the highly non-linear response of rotor blades geometrically non-linear analyses are important [97]. Moreover, buckling analyses are an essential part of the ultimate strength assessment of wind turbine blades, since buckling can be a failure mode [61, 62]. The critical buckling load is very depended on local cross-sectional deformation, which is a highly non-linear phenomenon and varies depending on the load configurations [46, 61, 62, 31, 32]. Cross-section deformations are often provoked by combined load situations, where e.g. bending moments and torsional moments act simultaneously. A drawback of non-linear *Finite Element Analysis* (FEA) is that applying the cutting forces and moments from the extreme loading matrix as boundary conditions is not possible, since non-linear effects do not allow superposition.

In the following, an ultimate strength analysis of a 34 m blade is conducted to show the importance of comprehensive blade modelling and to reveal a method to improve FEA of rotor blades. Aeroelastic simulations, following the IEC 61400-1 standard [112], were conducted. Based on the time series values of all DLC searched for the bending moment components M_x and M_y, resulting bending moments (M_R) and bending moment angles (θ_M) for all load directions were computed. The maximum M_R values and its contemporaneous load components for each cross section were summarised in a 3D load envelope. Distributed bending moments for different load directions were applied to both, geometrically linear and non-linear structural blade models simulated in Abaqus.

D.3 Methods

D.3.1 Aeroelastic simulations

In this study a 34 m long wind turbine blade designed for a three bladed wind turbine with a rated power capacity of 1.5 MW and a variable speed with a maximum rotor speed of 18 min^{-1} was used.

The aeroelastic load simulations were performed with *DTU's* aeroelastic software package *Horizontal Axis Wind turbine Code* HAWC2 11.9, a multibody formulation code intended to calculate the dynamic response of wind turbines in the time domain [74, 49]. For this purpose, the turbine structure was subdivided into a number of bodies. The structure of each body consists of an assembly of linear Timoshenko beam elements, connected via coupling constraints, taken non-linear effects of the body motion (rotations and deformations) into account [49]. The aerodynamic load calculation in HAWC2 is based on an extended version of the principle blade element momentum theory, accounting for the effect from large blade deflections, tip losses etc. as described in Reference [49].

The airfoil characteristics and cross-section rigidity of the blade were modelled according to manufacturer specifications. The wind turbine blade was discretised with 17 linear Timoshenko beams providing a proper subdivision of the blade, representing properly non-linear effects of large rotation and deflection. Since no other detailed information of hub, tower and generator properties were available, these parts were based on the Neg Micon NM80 turbine platform [118] with a rated power of 2.3 MW. The use of the Micon NM80 turbine platform was considered to be acceptable due to a similar blade length of 38.8 m. The PI-controller of the pitch-controlled wind turbine system from the NM80 was downrated to 1.5 MW and adapted to the structural changes. The controller adjustment was accomplished by using DTU's aeroservoelastic stability tool *HAWCStab2* [50].

Design Load Cases (DLCs), as directed by the ICE 61400-1 standard [112], were simulated for different levels of wind conditions, yaw misalignment, turbulence and gust conditions (seeds). In total, 1688 load simulations were computed due to different seeds, wind speeds and yaw angles. All considered DLCs are presented in Table D.1. The wind turbine response in time domain for the individual DLC provides, among others, information regarding the occurring forces, bending moments and torsion in the 17 cross sections along the blades. The loads, as a function of the time, were multiplied with the corresponding *Partial Safety Factors* (PSF). The entire loads represent the design load spectrum, which the wind turbine blades might be challenged to withstand during lifetime.

D.3.2 Three dimensional load envelope

According to the IEC 61400-1 standard [113], only the maximum and minimum values for the load components and resultants of each dynamic load case have to be considered for the ultimate loads. The most extreme loading from the different load cases is then used to define an overall load envelope. However, the load carrying capacity of wind turbine blades is highly dependant on the load direction. Therefore, a *three-dimensional* (3D) load envelope approach is presented, where the extreme loads in each load direction are extracted from

Table D.1: Design load cases with the corresponding PSF and wind turbulence and gust conditions for the extreme load calculation [43].

Name	PSF	Seeds	Description	Wind turbulence and gust conditions
DLC 1.1	1.25	18	Normal production	Normal turbulence model
DLC 1.3	1.35	6	Normal production	Extreme turbulence model
DLC 1.4	1.35	1	Normal production	Extreme coherent gust with direction change
DLC 1.5	1.35	4	Normal production	Extreme wind shear
DLC 2.1	1.35	12	Grid loss	Normal turbulence model
DLC 2.2b	1.10	12	One blade stucks at min. angle	Normal turbulence model
DLC 2.3	1.10	3	Grid loss	Extreme operation gust
DLC 2.4	1.00	6	Production in large yaw error	Normal turbulence model
DLC 3.1	1.00	1	Start-up	Normal wind profile model
DLC 3.2	1.35	4	Start-up at four different times	Extreme operation gust
DLC 3.3	1.35	4	Start-up	Extreme direction change
DLC 4.1	1.00	1	Shut-down	Normal wind profile model
DLC 4.2	1.35	6	Shut-down at six different times	Extreme operation gust
DLC 5.1	1.35	12	Emergency shut-down	Normal turbulence model
DLC 6.1	1.35	6	Parked in extreme wind	Extreme wind speed model
DLC 6.3	1.35	1	Parked with large yaw error	Extreme wind speed model
DLC 6.4	1.00	14	Parked	Normal turbulence model
DLC 8.1	1.50	12	Maintenance	Normal turbulence model

the aeroelastic simulations for different DLCs. The maximum load resultants for 360° around each cross section were extracted and divided into bins of 1° angles along the span. Based on the three dimensional load envelope the bending moment distribution along the span for each load direction of 1° can be computed and used to perform detailed structural simulations to determine resulting stress and strain values in the particular load direction.

To create the 3D load envelope, for each time signal (t) the acting direction and the resulting bending moment were computed based on the bending moment vector components $M_x\,(t)$ and $M_y\,(t)$. From the bending moments and load directions (divided into bins) for each simulation and cross section, the maximum resultant for each DLC was used to define the extreme load for the particular load direction (Figure D.2(a)). The maximum bending moment resultant of all considered DLCs as a function of the loading direction was defined as the ultimate design load for the particular angle and cross section (Figure D.2(b)).

By connecting the maximum bending moments of the individual cross sections along the blade under a specific angle, the ultimate bending moment distribution along the blade can be generated (Figure D.3(a)). Moreover, the corresponding forces, bending moments, torsion, time and DLC had been stored in a load matrix to provide additional information to the visualised load envelope shown in Figure D.3(a).

The load matrix contains all relevant information extracted from HAWC2, to be able to load a blade physically or numerically corresponding to the ultimate design load. However, in experiments, blades are usually loaded by applying forces, and since HAWC2 only provides internal forces, the transverse force tensors have to be calculated. The bending moment magnitudes (M_i), obtained from the envelope, can be used to calculate the force magnitudes (F_i) which

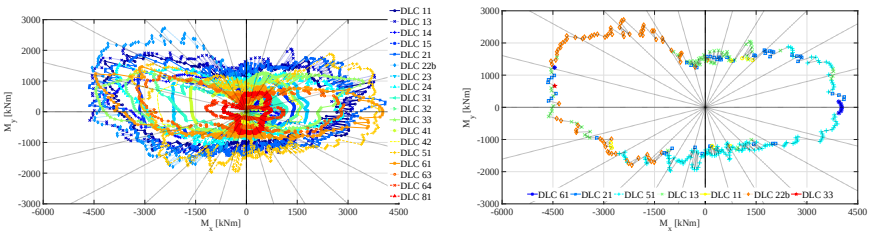

(a) (b)

Figure D.2: (a) Bending moment distribution for the root section showing all DLCs. (b) Bending moment distribution for the root section showing only the ultimate design load extracted from the maximum bending moments of all DLCs and the relevant DLCs for the ultimate design load envelope.

create a bending moment distribution that emulates those obtained from aeroelastic simulations (Figure D.3(b)). In Equation D.1, an example is given on how to calculate a linear bending moment distribution based on four *load points* (LP).

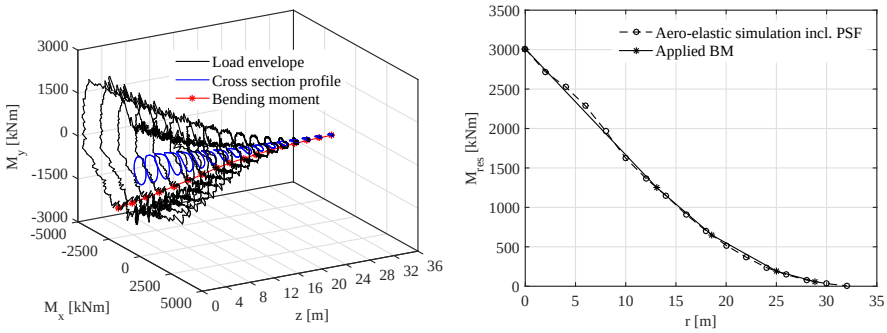

(a) (b)

Figure D.3: (a) Three-dimensional load envelope along the blade length (z) with schematically shown blade cross sections and an exemplary shown bending moment distribution under a load direction of 225°. (b) Aeroelastic predicted bending moment distribution along the blade in comparison to a linearly, force controlled bending moment for a load direction angle of 225°.

$$\begin{pmatrix} F_1 \\ F_2 \\ F_3 \\ F_4 \end{pmatrix} = \begin{bmatrix} \frac{1}{z_1 - z_2} & 0 & 0 & 0 \\ \frac{z_3 - z_1}{(z_2 - z_3)(z_1 - z_2)} & \frac{1}{z_2 - z_3} & 0 & 0 \\ \frac{1}{z_2 - z_3} & \frac{z_4 - z_2}{(z_3 - z_4)(z_2 - z_3)} & \frac{1}{z_3 - z_4} & 0 \\ 0 & \frac{1}{z_3 - z_4} & \frac{-z_3}{(z_3 - z_4)z_4} & \frac{1}{z_4} \end{bmatrix} \cdot \begin{pmatrix} M_2 \\ M_3 \\ M_4 \\ M_5 \end{pmatrix} \tag{D.1}$$

F_i represents the force magnitudes and z_i denotes the lengthwise position of the individual force application points; the indices $1 - 4$ represent the locations of force application points for a linearly applied bending moment distributed via 4 load applications points, where index 1 represents the outermost one and index 4 the one closest to the root section; M_i represents the aeroelastic bending moment magnitude; index 5 represents the root bending moment. Four LP had been chosen in the study to apply a linear bending moment distribution in order to have an adequate replication of the non-linear aeroelastic bending moment distribution without affecting the local stress and strain distribution of the blade by having too many LP.

In this study a numerical analysis of the 34 m blade was conducted, where the blade was loaded by applying the extreme loads from the load envelope of 24 different load directions. The aeroelastic predicted bending moment distribution along the blade (each 15°) was applied to the blade. Figure D.4 shows the aeroelastic load envelope in comparison to the applied bending moment distribution. Furthermore, the theoretical certification loads in flapwise and edgewise direction as a result of the maximum and minimum loads on the abscissa and ordinate of the bending moment distribution are shown. It can clearly be seen that some resultant bending moment magnitudes ($M_R = \sqrt{M_x^2 + M_y^2}$) are significantly bigger than the required flapwise and edgewise certification bending moments.

Figure D.5 shows the polar coordinate system defining the bending moment vector and its angular direction α. The associated force vector, obtained from Equation D.1 was transformed into the components F_x and F_y of the cross-section coordinate system. Figure D.5 depicts the correlation between the resulting bending moment angle and its acting load direction with $-90°$ offset angle.

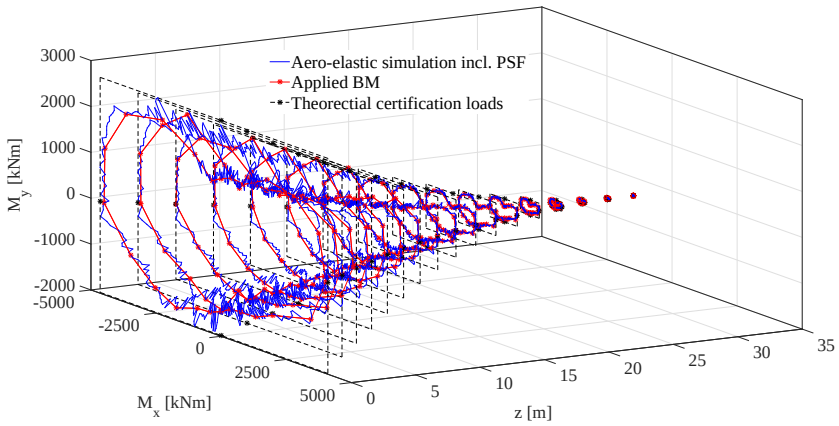

Figure D.4: Aeroelastic load envelope in comparison to the applied bending moment distribution and the four theoretical certification loads in flapwise and edgewise direction as a result of the maximum and minimum loads on the abscissa and ordinate of the bending moment distribution.

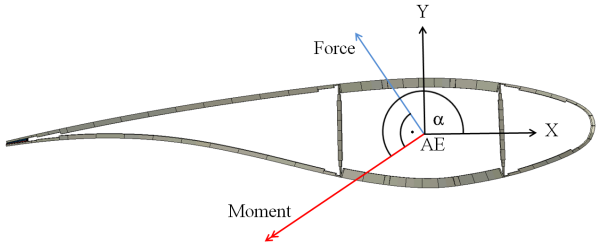

Figure D.5: Cross section coordinate system and loading directions with bending moment vector and force vector. The angle α represents the direction of the bending moment vector measured counterclockwise from the X-axis.

D.3.3 Structural simulations

The investigated 34 m wind turbine blade consists of a box girder as the main load carrying structure surrounded by adhesively connected upper and lower panels forming the aerodynamic surface. The panels, forming the pressure-side and suction-side, are themselves connected by a trailing-edge joint and a

leading-edge joint.

For the structural analysis of the blade a numerical model created in Abaqus 6.14 was used. The initial geometry of the blade was mainly discretised by $9.4x10^4$ 4-node general-purpose layered shell elements (Abaqus type S4) with a characteristic element length of 0.05 m. The aerodynamic blade profile was chosen as reference surface with an offset from the shell's midsurface corresponding to half the material thickness to account for continuously varying thickness of the layup. The advantage of using the aerodynamic surface as the reference surface is that it represents the physical geometry more accurately [16]. No offset was chosen for the shear webs, where the geometrical middle of the shear webs was taken as reference surface.

Previous studies [44, 46] have shown that shell elements do not accurately represent the trailing edge behaviour of the wind turbine blade. Consequently, the adhesive of the trailing edge joint with a constant bond length of 0.08 m was modelled with $3.5x10^4$ 8-node linear brick elements with reduced integration and hourglass control (Abaqus type C3D8I). A convergence study has proven that a characteristic element length of 0.01 m for the 8-node linear brick elements is suitable. The C3D8I elements were connected via tie constraints to the shell elements (Figure D.6).

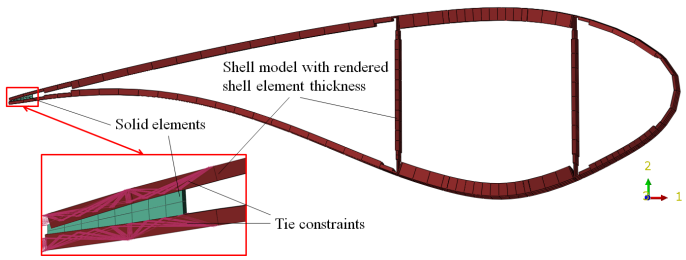

Figure D.6: Cross section of the blade showing the connection between the rendered shell elements and the solid brick elements discretising the trailing edge.

Laminate layup and material properties were assigned to the layered shell elements. Three shell integration points for each layer were used (Figure D.7). The elastic material properties of the laminate layup components as well as the properties of the epoxy based adhesive are listed in Table D.2. The indices 1 and 2 refer to the 0° and 90° direction respectively; E_{ij} represents the elastic modulus, G_{ij} represents the shear modulus, ν_{ij} denotes the Poisson's ratio, *Triaxial* is a triaxial glass fibre and *Triaxial 2* is a triaxial glass fibre with high resin content. *UD* represents unidirectional glass fibre cloths, *Biaxial Pre* represents a biaxial

glass fibre pre-preg cloths, whereas *Biaxial* is a sprint biaxial glass fibre cloth and *Adhesive* represents the epoxy-based bonding paste used for the joints.

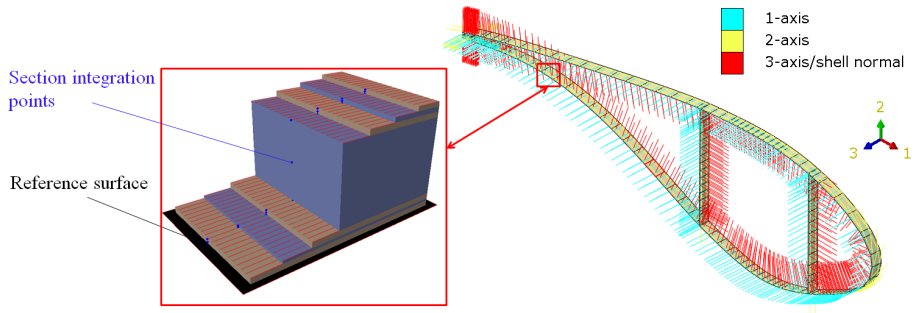

Figure D.7: Material orientation of the blade model and an example of a section layup for the sandwich panel. The layup consists of a face sheet with three top layers and a core material. For each individual layer three section integration points are used for the *Finite Element Analysis* (FEA).

Table D.2: Material properties as specified by the manufacturer.

Engineering constants	*U/D glass*	*Triaxial glass*	*Triaxial glass HRC*	*Biaxial glass*	*Biaxial pre-preg*	*Polymer foam*	*Units*
E_{11}	41.26	20.26	16.70	12.75	11.58	0.0485	GPa
E_{22}	11.39	10.42	8.587	12.75	11.58	0.0485	GPa
ν_{12}	0.33	0.50	0.50	0.50	0.50	0.40	-
G_{12}	3.91	7.35	6.605	10.06	10.06	0.0391	GPa
$\epsilon_{tensile}$	0.021	0.023	0.023	0.017	0.011	-	-
$\epsilon_{compressive}$	0.016	0.012	0.016	0.015	0.014	-	-
ϵ_{shear}	0.0037	0.014	0.014	0.014	0.014	-	-
X^T	903.60	472.06	389.04	214.20	123.91	1.4	MPa
X^C	660.16	324.16	267.15	184.88	156.33	1.3	MPa
Y^T	42.14	127.12	104.76	184.88	156.33	1.4	MPa
Y^C	42.14	127.12	104.76	184.88	156.33	1.3	MPa
S^L	58.65	99.25	89.17	143.91	143.91	1.1	MPa
S^T	58.65	99.25	89.17	143.91	143.91	1.1	MPa
ρ	1931	1864	1683	1894	1890	80	kg/m^3

According to Bitsche [16], it is best to apply loads via a small number of concentrated forces and moments to the blade in order not to constrain and affect the

blade response. In this study, the loads were applied through surface-based distribution coupling constraints (Figure D.8). This means that a group of nodes located on the surface, discretising the spar caps, were constrained to a reference node. Four continuum distributing coupling constraints were assigned to the cross sections at 13.20 m, 18.60 m, 25.04 m and 28.78 m. The loads are applied to the corresponding reference nodes, which are located in the aeroelastic centres of the cross sections. Figure D.8 depicts a cross-section slice of the blade model with continuum distribution coupling constraints. The shell nodes of the caps are connected to a reference node, which is located at the aeroelastic centre at a radial position of 13.20 m.

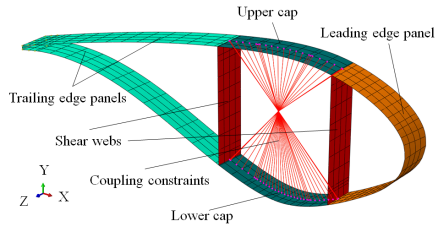

Figure D.8: Cross-section slice of the blade model and continuum distribution coupling constraints connected to the shell nodes of the caps and the reference node. The reference node is located at the aeroelastic centre of the cross section. The figure show a cross-section slice at a radial position of 13.20 m.

For the structural FEA, the force components F_x and F_y were applied to replicate the bending moment distribution for the specific load direction. Radial forces (F_z) were not applied, since the stresses caused by the radial forces are usually low [112]. Generally, torsional loads can be significant in the structural design and therefore should be included [115]. To investigate the impact of torsional moments, three different scenarios were investigated - a linear analysis without applying a torsional moment, a linear FEA including a torsional moment and a non-linear analysis without applying a torsional moment. The torsional moment applied to the linear analysis corresponds to the torsional moment from the root section of the blade. The torsional moment at the root section of the blade was generated by distributing the torsional moment equally to the four reference nodes acting as *Loading Points* (LP). This means that the total torsional moment was divided by four and increased by one quarter at each coupling constraint. Moreover, for the linear FEA the torsional moment reached its maximum already at a radial position of 13.20 m, whereas in reality the torsional moment would be biggest at the root section.

For the non-linear simulations no torsional moment (M_z) was applied. The reason is that torsion is assumed to be a function of the distance between the aeroelastic centre (AC) and centre of gravity (CG) to the elastic centre (EC) of the airfoil (Figure D.9(a)) and the non-linear deformation of the blade structure. Thus, by applying the force components F_x and F_y to the reference points in the aeroelastic centre of the cross sections, a torsional moment should be created by using non-linear simulation methods (D.9(b)), since the applied forces acting on the deflecting structure cause a torsional moment in point A_0.

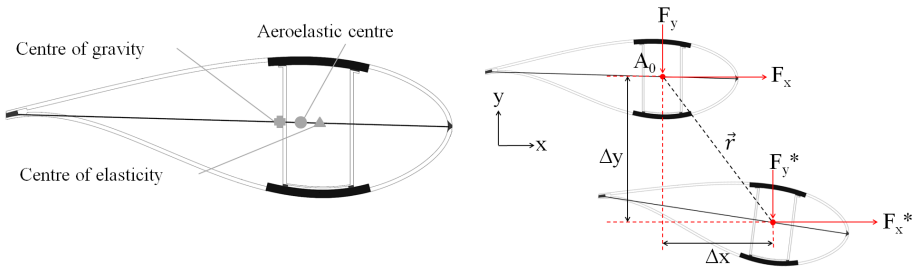

(a) (b)

Figure D.9: (a) Blade section - characteristic position of the blade dynamics. The elastic centre defines the position of the shear centre for each cross section. The centre of gravity is defined as the point of action of forces resulting from inertia and weight. The aeroelastic centre represents the point of attack of the lift and drag forces [40]. (b) During the non-linear analysis, the applied forces acting on the deflecting structure cause a torsional moment ($M_z(A_0) = F_x^* \Delta y + F_y^* \Delta x$).

The applied loads were assumed to be quasi-static. Abaqus's standard Newton-Raphson solver technique was used allowing for both, geometric linear and non-linearity simulations.

D.3.4 Failure evaluation

The blade response was evaluated based on stress and strain based failure criteria as well as on a non-linear buckling analysis to account for material and geometric failure within the ultimate strength assessment. The maximum strain, maximum stress, Azzi-Tsai-Hill, Tsai-Wu and Tsai-Hill criterion were used for the ultimate strength analysis. As material parameters the longitudinal tensile strength X_t, longitudinal compressive strength X_c, transverse tensile strength

Y_t, transverse compressive strength Y_c, longitudinal shear strength S_l and transverse shear strength S_t as well as the allowable tensile strain $\epsilon_{tensile}$, allowable compressive strain $\epsilon_{compressive}$, allowable shear strain ϵ_{shear} given in Table D.2 are used. For the Tsai-Wu failure criterion, the load interaction curve-fit parameter $f*$ was set to 0 since no other material data for the lamina than the given in Table D.2 were available. More information regarding the used failure criteria related to this study can be found in Haselbach [46].

D.4 Results

D.4.1 Aeroelastic results

Blade design is an iterative process where usually several iterations loops are needed to define an optimal compromise between aerofoil geometry, structural design and aeroelastic response. Knowing the primary design-driving load cases helps to reduce the amount of DLC, which have to be computed and analysed during the iterative blade design with changing blade designs. Figure D.2(b) shows that basically five extreme load cases were the design-driving load cases, namely DLC 1.3, 2.1, 2.2b, 5.1 and 6.1. Reducing the aeroelastic analysis during the preliminary design phase to the most critical DLCs can speed up the design and finally the ready-to-market time for new wind turbine blades. However, for the final strength assessment a comprehensive analysis of all DLC is required.

D.4.2 Structural analyses

The ultimate strength assessment of the blade was investigated based on different failure criteria for both, geometrical linear and non-linear analyses. The entire blade, from the blade root to the tip, was analysed. The maximum failure indication values for the blade exposed to the extreme load for different load directions (bending moment angle) were extracted and plotted in a polar failure envelope (Figure D.10). Failure theoretically occurs when the failure criterion prediction indicates failure values bigger than one. For each bending moment angle (each 15°) the maximum failure value through all plies of the entire blade was evaluated. Neither specific locations nor cross sections were analysed. However, most of the failure values were located at the transition region and the airfoil region of the blade (blade shoulder). In Figure D.10, the failure envelopes for different failure criteria and solver methods are plotted. The blade profile cross section depicted in Figure D.10 is only plotted to visualise the blade orientation with respect to the bending moment angle.

The failure envelope plots (Figure D.10) represent the *Failure Index* (I_F) of

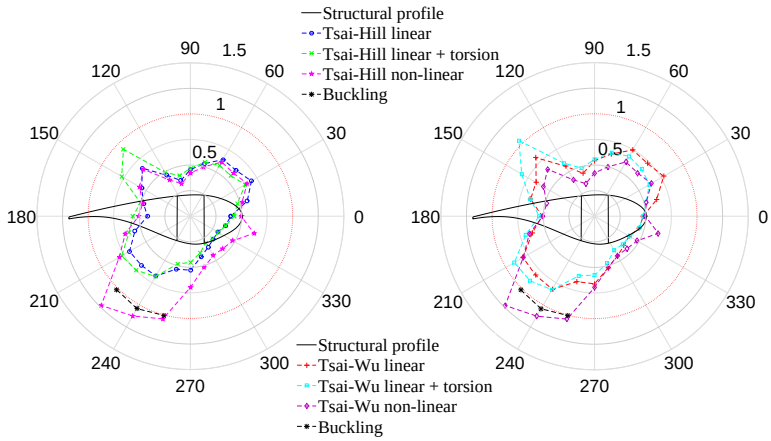

Figure D.10: Failure envelope for the blade exposed to the extreme load for different load directions (bending moment angle). Failure theoretically occurs when the failure criterion prediction indicates failure values bigger than one.

the Tsai-Hill and Tsai-Wu failure criteria as well as they indicate buckling in cases, where the blade geometry buckled. The results of the maximum strain, maximum stress, Azzi-Tsai-Hill failure envelopes were not plotted because the results of those criteria were quite similar to the results of the Tsai-Hill failure criterion.

The plots in Figure D.10 show that the Tsai-Wu criterion is more conservative than the Tsai-Hill criterion. The reason for the more conservative failure prediction of the Tsai-Wu failure criterion is attributed to the load interaction curve-fit parameter $f*$ as described in detail in Haselbach [46]. The *first-ply failure* (FPF) criteria predicted partly significantly different I_F dependent on the FEA type and absence or presence of torsion.

The Tsai-Hill criterion applied to the linear FEA including torsion predicted the highest I_F for bending moment angle 135° and 155°. The Tsai-Hill criterion applied to the non-linear simulation also indicated a slightly higher I_F for 135° but less critical than the linear FEA including torsion. The non-linear failure analysis predicted material failure for load directions of 225° to 255°. The high I_F can directly be associated with trailing edge buckling for load directions, where the trailing edge was exposed to high compressive stress. The trailing edge buckling led to a significant increase of the stress, and thus to stresses exceeding the ultimate strength of the material. For the linear FEA without torsion, the Tsai-Hill criterion did not indicated any critical IF.

The Tsai-Wu criterion predicted higher I_F compared to the other failure criteria. The linear FEA without torsion indicated high I_F for bending moment directions of 135° and 225° to 255° but does not reach critical ranges. The linear FEA including torsion also indicated high I_F for bending moment directions of 135° and 225° to 255°. For these directions, the I_F were higher than for the linear FEA without torsion. In particular for a bending moment angle of 135° material failure was indicated for the linear FEA including torsion. The Tsai-Wu criterion applied to the non-linear simulation results showed in general lower I_F compared with the linear simulations. However, for load directions between 225° to 255° failure was indicated. Here, the high I_F can directly be linked to trailing edge buckling as described above and shown in Figure D.11.

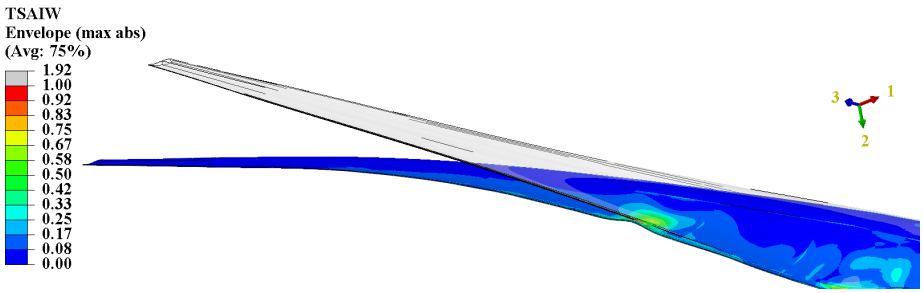

Figure D.11: Blade exposed to ultimate load for the bending moment angle 255°. The Tsai-Wu failure criterion indicates material failure, among others, in the trailing edge and spar cap/shear web region due to buckling onset in the trailing edge. A scaling factor of 2.5 is used to amplify to buckling effect for better visualisation purpose.

The non-linear geometrical buckling analysis predicted buckling only for three extreme load directions. For bending moment angles 225°, 240° and 255° buckling in the trailing edge of the blade was predicted to start at load levels close to the ultimate load (98 %, 96 % and 99 %). Associated with trailing edge buckling onset a significant increase of the I_F was predicted for the different failure criteria. Since only the non-linear FEA account for the buckling phenomenon, they indicated failure for those bending moment directions, whereas the linear FEA did not. Thus, buckling can explain the significant deviations of the I_F between both, geometrically linear and non-linear FEA for bending moment angles 225°, 240° and 255°.

To understand the differences between both methods for other load directions, the torsional moment has to be focused on. Figure D.12(a) shows the torsional

moment at the blade root section. The torsional moment as predicted from the aeroelastic code HAWC2 (contemporaneous to the bending moment of 3D load envelope) and the torsional moment acting on the blade root for the geometrically non-linear FEA (Abaqus) are plotted. The torsional moment, which had been applied to the geometrical linear simulation including torsion is equivalent to those of the aeroelastic simulations. The torsional moment, obtained at the root section of the structural analysis (Abaqus), is a result of the applied bending moment distribution and the complex blade geometry extracted from the geometrical non-linear FEA. The comparison of both torsional moments shows qualitatively good agreement (Figure D.12(a)). However, the torsional moment absolute magnitudes from the aeroelastic analyses differ partly significantly from the torsional moment obtained at the root section of the structural analysis. Especially for the bending moment directions 135° and 150° the bending moment obtained from the structural FEA is less distinct than the torsional moment resulting from the aeroelastic simulations. The reason for the difference can be explained with the origin of both values. The torsional moment from the structural analysis is a results of the bending moment distribution along the blade and the resulting blade deformation. The aeroelastic torsional moment is an individual value, contemporaneous to the bending moment a the blade cross section for this time increment but decoupled from the bending moment distribution along the blade. The consequence of the significant difference of both torsional moments leads to a critical I_F predicted for the geometrically linear simulations, whereas the non-linear did not predict such high I_F. The high I_F for the geometrically linear analysis was predicted in the shoulder region of the blade and can be affected by the way it was introduced into the blade model. Figure D.12(b) shows the torsional moment distribution along the blade span in the geometrically linear analysis.

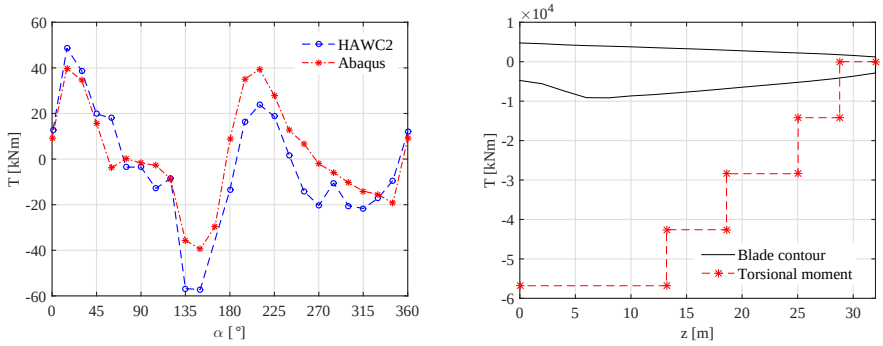

(a) (b)

Figure D.12: (a) Torsional moment (T) in kNm over bending moment angle (α) in ° extracted at the blade root and compared for the aeroelastic simulation and Abaqus. (b) Torsional moment (T) in kNm along the blade span (z) as applied to the geometrically linear FEA including torsion for a bending moment angle of 135°.

D.5 Conclusion

In this paper a method to evaluate wind turbine blade failure based on a 3D load envelope was introduced with the purpose to reduce the amount of aeroelastic simulations necessary to run during the iterative design process. Based on the bending moment distribution of the 3D load envelope, a preliminary study on the different results of the ultimate strength assessment of linear and non-linear FEA was performed.

From the preliminary results, it can be concluded that for similar torsional moments the ultimate strength predictions seem to be similar. In cases where the torsional moment significantly deviates from each other, distinct difference in the ultimate strength assessment can occur. The analysis showed, although the torsional moments are relatively low in comparison to the applied bending moments, that torsional moments can have a significant effect on the structural response. Furthermore, the study demonstrates the importance of simulation tools taking geometrical non-linear deformations into account in order to determine ultimate strength failure based on instability effects.

To evaluate the use of the purposed 3D load envelope, further investigations are necessary. The strain and stress distribution for different cross sections along the blade span, based on geometrically linear simulations including the superposition of all six load components, for different bending moment angles will

be compared to the results of the geometrically non-linear FEA analysed in one shoot as purposed. This investigation approach should lead to a clear evaluation of the possible benefit of the purposed 3D load approach and demonstrate the strength and weakness of both methods.

Acknowledgement

The research paper is based upon work supported by the new Danish Centre for Composite Structures and Materials for Wind Turbines (DCCSM), grant no. 09-067212 from the Danish Strategic Research Council. The support is gratefully acknowledged.

The authors wish to thank Morten Hartvig Hansen, David Robert Verelst and Georg Pirrung from the DTU Wind Energy's Aeroelasiticity group to tune the HAWC2 model and controller and do run the DLCs. The authors are very grateful for this support.

Bibliography

[1] Conversation with power supplier.

[2] S. Abrate. Impact on Laminated Composite Materials. *Applied Mechanical Review*, 44(44):155–190, 1991.

[3] Danish Energy Agengy. Energy statistics 2013. http://www.ens.dk/en. Accessed: 2015-10-16.

[4] G. Alfano. On the influence of the shape of the interface law on the application of cohesive-zone models. *Composites Science and Technology*, 66(6):723–730, 2006.

[5] T. L. Anderson. *Fracture Mechanics: Fundamentals and Applications*. Taylor & Francis, 2005.

[6] Danish Wind Industry Association. The Power of the Wind: Cube of Wind Speed. http://xn–drmstrre-64ad.dk/wp-content/wind/miller/windpower2015. Accessed: 2015-09-10.

[7] S. Ataya and M. M. Z. Ahmed. Damages of Wind Turbine Blade Trailing Edge: Forms, Location, and Root Causes. *Journal of Engineering Failure Analysis*, 35:480–488, 2013.

[8] K. B. Atkinson. *Close Range Photogrammetry and Machine Vision*. Whittles Publishing, 1996.

[9] S. Azari, M. Papini, J. A. Schroeder, and J. K. Spelt. Fatigue threshold behaviour of adhesive joints. *International Journal of Adhesion and Adhesives*, 30:145–159, 2010.

[10] C. Bak, R. D. Bitsche, A. Yde, T. Kim, H. Morten, F. Zahle, M. Gaunaa, J. P. A. Blasques, M. Døssing, H. Wedel, J. Jens, and T. Behrens. The 10-MW reference wind turbine. *Proceedings of EWEA 2012 - European Wind Energy Conference & Exhibition. EWEA - The European Wind Energy Association*, 2012.

[11] G. I. Barenblatt. The Mathematical Theory of Equilibrium Cracks in Brittle Fracture. *In Advances in Applied Mechanics, Vol. 7, pp. 55-129*, 1962.

[12] C. S. Bartlett, K. Joyce-Bassett, and R. Botello. Quarterly Bulletin of the World Wind Energy Association. *WWEA Bulletin*, 1(1), 2015.

[13] Z. P. Bažant and L. Cedolin. *Stability of Structures - Elastic, Inelastic, Fracture and Damage Theories*. World Scientific, 2010.

[14] M. L. Benzeggagh and M. Kenane. Measurement of Mixed-Mode Delamination Fracutre Toughness of Unidirectional Glass/Epoxy Composites with Mixed-Mode Apparatus. *Composites Science and Technology*, 56:439–449, 1996.

[15] C. Berggreen. *Damage Tolerance of Debonded Sandwich Structures*. PhD thesis, Technical University of Denmark, September 2004.

[16] R. D. Bitsche. Modelling of wind turbine blades with abaqus, 2015. Composites Seminar, Roskilde, Denmark, 12/03/2015.

[17] Bladed. Bladed - bladed wind turbine simulation tool. https://www.dnvgl.com/services/bladed-3775. Accessed: 2015-11-26.

[18] J. P. Blasques. User's manual for BECAS - a cross section analysis tool for anisotropic and inhomogeneous beam sections of arbitrary geometry. Technical Report Risø-R-1785(EN), Risø DTU, National Laboratory for Sustainable Energy, 2011.

[19] K. Branner and P. Berring. Compressive Strength of Thick Composite Panels. *Risø International Symposium on Material Science*, 2011.

[20] L. G. Brazier. On the Flexure of Thin Cylindrical Shells and other 'Thin' Sections. *Proc. R. Soc. Lond.*, Ser. A, 116:104–114, 1927.

[21] P. P. Camanho, C. G. Davila, and M. F. Moura. Numerical Simulation of Mixed-Mode Progressive Delamination in Composite Materials. *SAGE - Journal of Composite Materials*, 37, 2003.

[22] P.P. Camanho and C. G. Davila. Mixed-Mode Decohesion Finite Elements for the Simulation of Delamination in Composite Materials. Technical Report NASA/TM-2002-211737, NASA, 2002.

[23] L. S. Cecchini and P. M. Weaver. Brazier Effect in Multibay Airfoil Sections. *AIAA Journal*, 43(10):2252–2258, 2005.

[24] Global Wind Energy Council. Global Wind Report Annual Market Update 2014. *Global Wind Energy Council*, 2015.

[25] K. Cox and A. Echtermeyer. Effects of composite fiber orientation on wind turbine blade buckling resistance. *Wind Energy*, 17:1925–1943, 2014.

[26] L. Damkilde and B. Lund. A Simplified Analysis of the Brazier Effect in Composite Beams. *Civil-Comp Press*, 207:1–11, 2009.

[27] Dassault Systèmes. *Abaqus Analysis User's Manual, Vol. 6.14*, 2015.

[28] DNV/Risø. *Guidelines for Design of Wind Turbines*. DNV/Risø, 2009.

[29] D.S. Dugdale. Yielding of steel sheets containing slits. *Journal of the Mechanics and Physics of Solids*, 8(2):100–104, 1960.

[30] M. A. Eder and R. D. Bitsche. Fracture analysis of adhesive joints in wind turbine blades. *Wind Energy*, page 16, 2014.

[31] M. A. Eder and R. D. Bitsche. A qualitative analytical investigation of geometrically nonlinear effects in wind turbine blade cross sections. *Thin-Walled Structures*, 93:1–9, 2015.

[32] M. A. Eder, R. D. Bitsche, and F. Belloni. Effects of geometric nonlinearity on energy release rates in a realistic wind turbine blade cross-section. *Composite Structures*, 2015.

[33] M. A. Eder, R. D. Bitsche, M. Nielsen, and K. Branner. A Practical Approach to Fracture Analysis at the Trailing Edge of Wind Turbine Rotor Blades. *Wind Energy*, 16(6):1007–1022, 2015.

[34] A. A. D. Escárpita, D. Cárdenas, H. Elizalde, R. Ramirez, and O. Probst. Biaxial Tensile Strength Characterization of Textile Composite Materials. *Composites and Their Properties*, 2012.

[35] FAST. FAST - an aeroelastic computer-aided engineering (cae) tool for horizontal axis wind turbines. https://nwtc.nrel.gov/FAST. Accessed: 2015-11-26.

[36] S. J. Fattahi, A. Zabihollah, and S. Zareie. Vibration Monitoring of Wind Turbine Blade using Fiber Bragg Grating. *Wind Engineering*, 34(6):721–731, 2010.

[37] L. Fingersh, M. Hand, and A. Laxson. Wind Turbine Design Cost and Scaling Model Wind Turbine Design Cost and Scaling Model. *Contract*, 29(December):1–43, 2006.

[38] M. Fiolka. *Theorie und Numerik volumetrischer Schalenelemente zur Delaminationsanalyse von Faserverbundlaminaten.* Kassel University Press, 2008.

[39] M. Gaotti, M. C. Rizzo, K. Branner, and P. Berring. An high order Mixed Interpolation Tensorial Compenents (MITC) shell element approach for modeling the buckling behavior of delaminated composites. *Composite Structures*, 108:657–666, 2014.

[40] R. Gasch and J. Twele. *Wind Power Plants - Fundamentals, Design, Construction and Operation.* Springer, 2012.

[41] The Danish Government. Energy strategy 2050 - from coal, oil and gas to green energy. *Energy Strategy 2050*, 2011.

[42] A. A. Griffith. The Phenomena of Rupture and Flow in Solids, 1921.

[43] M. H. Hansen, K. Thomsen, and A. Natarajan. Design Load Basis for onshore turbines; Revision 00; Tech.Report DTU Wind Energy-E-0074(EN). Technical report, Department of Wind Energy, DTU Risø Campus, Frederiksborgvej 399, DK 4000 Roskilde, Denmark, 2015.

[44] P. U. Haselbach. Nonlinear Finite Element Analysis of Delamination Growth in Composite Wind Turbine Blades. *Diplomarbeit written at the Universität Bremen, Germany*, 2012.

[45] P. U. Haselbach and K. Branner. Effect of Trailing Edge Damage on Full-Scale Wind Turbine Blade Failure. *20th International Conference on Composite Materials, Copenhagen*, 2015.

[46] Philipp Ulrich Haselbach, Martin Alexander Eder, and Federico Belloni. A comprehensive investigation of trailing edge damage in a wind turbine rotor blade. *Wind Energy*, 19:1871–1888, 2016. we.1956.

[47] Z. Hashin. Failure Criteria for Unidirectional Fiber Composites. *Journal of Applied Mechanics*, 47:329–334, 1980.

[48] Z. Hashin and A. Rotem. A Fatigue Failure Criterion for Fiber Reinforced Materials. *Journal of Composite Materials*, 7:448–464, 1973.

[49] HAWC2. HAWC2 - horizontal axis wind turbine simulation code 2nd generation. http://www.hawc2.dk. Accessed: 2015-04-24.

[50] HAWCStab2. HAWCStab2 - Aero-servo-elastic stability tool for wind turbines. http://www.hawcstab2.vindenergi.dtu.dk. Accessed: 2015-04-24.

[51] X. He. A review of finite element analysis of adhesively bonded joints. *International Journal of Adhesion & Adhesives*, 31:248–264, 2011.

[52] A. Herrmann. *Skriptum zur Vorlesung Mechanink der Faserverbundstrukturen I.* University of Bremen, 2008.

[53] K. O. Hill and G. Meltz. Fiber Bragg grating technology fundamentals and overview. *Journal of Lightwave Technology*, 15(8):1263–1276, 1997.

[54] A. Hillerborg, M. Modéer, and P.-E. Petersson. Analysis of crack formation and crack growth in concrete by means of fracture mechanics and finite elements. *Cement and Concrete Research*, 6(6):773–781, 1976.

[55] M.J. Hinton, A.S. Kaddour, and P.D. Soden. Failure Criteria in Fibre Reinforeced Polymer Composites: The World-Wide Failure Exercise. *Elsevier*, page 13, 2001.

[56] David Hoeppner. Holistic structural integrity process. http://www.holsip.com. Accessed: 2015-09-24.

[57] M. Hörmann. *Nichtlineare Versagensanalyse von Faserverbundstrukturen.* PhD thesis, Institut für Baustatik der Universität Stuttgart, December 2002.

[58] C. E. Inglis. Stresses in a Plate Due to The Presence of Cracks and Sharp Corners, 1913.

[59] G.R Irwin. Onset of Fast Crack Propagation in High Strength Steel and Aluminum Alloys. *Sagamore Research Conference Proceedings*, pages 289–305, 1956.

[60] K. Ishi, M. Imanaka, and H. Nakayama. Fatigue crack propagation behavior of adhesively bonded CFRP/CFRP and CFRP/Aluminium joints. In *16th International Conference on Composite Materials*, pages 1–8, 2007.

[61] F. M. Jensen, A. S. Puri, J. P. Dear, K. Branner, and A. Morris. Investigating the impact of non-linear geometrical effects on wind turbine blades – Part 1: Current status of design and test methods and future challenges in design optimization. *Wind Energy*, 14(14):239–254, 2011.

[62] F. M. Jensen, P. M. Weaver, L. S. Cecchini, H. Stang, and R. F. Nielsen. The Brazier effect in wind turbine blades and its influence on design. *Wind Energy*, 15:319–33, 2012.

[63] W. S. Johnson. *Delamination and Debonding of Materials.* American Society for Testing and Materials, 1985.

[64] R. M. Jones. *Mechanics of Composite Materials.* Taylor and Francis Inc, 1975.

[65] R. Kashyap. *Fiber Bragg Gratings.* Academic Press, 1999.

[66] M. Kenane and M. L. Benzeggagh. Mixed-mode delamination fracture toughness of unidirectional glass/epoxy composites under fatigue loading. *Composites Science and Technology*, 57:597–605, 1997.

[67] A. D. Kersey. A Review of Recent Developments in Fiber Optic Sensor Technology. *Optical Fiber Technology*, 2:291–317, 1996.

[68] T. Kim, A. M. Hansen, and K. Branner. Development of an anisotropic beam finite element for composite wind turbine blades in multibody system. *Renewable Energy*, 2013.

[69] R. Krueger. Virtual crack closure technique: History, approach, and applications. *Applied Mechanics Reviews*, 57(2):109, 2004.

[70] L. Kühlmeier. *Buckling of wind turbine rotor blades.* PhD thesis, Aalborg University, 2007.

[71] F. Lahuerta, R. P. L. Nijssen, F. P. van der Meer, and L. J. Sluys. Effect of laminate thickness on the static and fatique properties of wind turbine composites. In *EAWE - European Academy of Wind Energy, 10th PhD Seminar on Wind Energy in Europe*, pages 1–5, Orléans, France, October 2014. EAWE.

[72] E. Lantz. Operations Ependitures: Historical Trends And Continuing Challenges. In *AWEA Wind Power Conference, Chicago, Illinois.* NREL/PR-6A20-58606, May 2013.

[73] I. Lapczyk and J. A. Hurtado. Failure Criteria for Unidirectional Fiber Composites. *Composites Part A*, 7:2333–2341, 2007.

[74] T. J. Larsen and A. M. Hansen. Influence of blade pitch loads by large blade deflections and pitch actuator dynamics using the new aeroelastic code HAWC2. *Proceedings of the European Wind Energy Conference*, 2006.

[75] T. J. Larsen and A. M. Hansen. How 2 hawc2, the user's manual. Technical Report Risø-R-1576(ver.4-5)(EN), Risø DTU, National Laboratory for Sustainable Energy, 2011.

[76] S. Laustsen, E. Lund, L. Kühlmeier, and O. T. Thomsen. Interfibre Failure Characterisation of Unidirectional and Triax Glass Fibre Non-Crimp Fabric Reinforced Epoxy Laminates. *Applied Composite Materials*, 22(1):51–79, 2014.

[77] M. LeGault. Wind blades: Progress and challenges. *Composite Technology - Composite World*, pages 1–5, 2013.

[78] E. Lindgaard and E. Lund. A unified approach to nonlinear buckling optimization of composite structures. *Computers and Structures*, 89:357–370, 2011.

[79] E. Machefaux. Multiple turbine wakes. *PhD thesis - DTU Wind Energy, Technical University of Denmark*, 2015.

[80] G. J. Marshall and I. H. Turvey. Buckling and Postbuckling of Composite Plates. *London - UK, Chapman and Hall*, 1995.

[81] The MathWorks, Inc., Natick, Massachusetts, United States. *MATLAB and Statistics Toolbox Release 2015a*, 2014.

[82] A. Matzenmiller, J. Lubliner, and R. L. Taylor. A Constitutive Model for Ansiotropic Damage in Fiber-Composites. *Mechanics of Materials*, 20:125–152, 1995.

[83] W. Morey, G. Meltz, and H. Glenn. Fiber optic Bragg grating sensors. In *OE/FIBERS'89*, 1989.

[84] M. Mukhopadhyay. *Mechanics of Composite Materials and Structures*. University Press Engineering, 2004.

[85] Office of Energy Efficiency & Renewable Energy. A New Era for Wind Power in the United States. *Wind Vision*, page 384, 2014.

[86] Danish Master Data Register of Wind Turbines. Danish Master Data Register of Wind Turbines. http://www.ens.dk/en/supply/renewable-energy/wind-power/facts-about-wind-power/facts-numbers, 2015. Accessed: 2015-09-10.

[87] A. C. Orifici, R. S. Thomson, R. Degenhardt, C. Bisagni, and J. Bayandor. Development of a Finite-Element Analysis Methodology for the Propagation of Delaminations in Composite Structures. *Mechanics of Composite Materials*, 43(1):9–28, 2007.

[88] L. C. T. Overgaard and E. Lund. Structural collapse of a wind turbine blade. Part A: Static test and equivalent single layered models. *Composites Part A: Applied Science and Manufacturing*, 41(2):257–270, 2010.

[89] L. C. T. Overgaard and E. Lund. Structural collapse of a wind turbine blade. Part B: Progressive interlaminar failure models. *Composites Part A: Applied Science and Manufacturing*, 41(2):271–283, 2010.

[90] J. K. Paik, K. Branner, Y. S. Choo, J. Czujko, Y. S. Fujikubo, J. M. Gordo, G. Parmentier, R. Iaccarino, S. O'Neil, I. Pasqualino, D. Wang, X. Wang, and S. Zhang. ISSC Committee III-1 Ultimate Strength. In *EAWE - European Academy of Wind Energy, 10th PhD Seminar on Wind*

Energy in Europe , pages 1–5, Seoul, Korea, August 2009. ISSC Committee III-1 Ultimate Strength, 17th International Ship and Offshore Structures Congress.

[91] D. M. Parks. A stiffness derivative finite element technique for determination of crack tip stress intensity factors. *International Journal of Fracture*, 10(4):487–502, 1974.

[92] M.J. Pavier and M.P. Clarke. Experimental techniques for the investigation of the effects of impact damage on carbon-fibre composites. *Composites Science and Technology*, 55(2):157–169, 1995.

[93] A. Puck. *Festigkeitsanalyse von Faser-Matrix-Lmaniaten, Modelle für die Praxis*. Carl Hanser Verlag München Wien, 1996.

[94] C. Red. Offshore wind: How big will blades get? *Composite Technology - Composite World*, pages 1–5, 2009.

[95] A. Riccio. *Damage Growth in Aerospace Composites*. Technology, Springer Aerospace, 2015.

[96] A. Roczek-Sieradzan, R. Bitsche, Z. Andrlová, C. Bak, B. Kallesø, M. Lagerbon, V. J. Wedel-Heinen, and V. Roudnitski. *Full Scale Test SSP 34m blade , Combined load . Data report*, volume 1749. Technical University of Denmark, 2010.

[97] M. Rosemeier, P. Berring, and K. Branner. Non-linear Ultimate Strength and Stability Limit State Analysis of a Wind Turbine Blade. *Wind Energy*, online available, 2015.

[98] K. Schroeder, W. Ecke, J. Apitz, E. Lembke, and G. Lenschow. A fibre Bragg grating sensor system monitors operational load in a wind turbine rotor blade. *Measurement Science and Technology*, 17(5):1167–1172, May 2006.

[99] R. Schultz. *Nichtlineare Struktur- und Versagensanalyse von Faserverbundsystemen mit Mehrschichten-Schalenelementen*. PhD thesis, Institut für konstruktiven Ingenieurbau, Ruhr-Universität Bochum, 1996.

[100] H. Schürmann. *Konstruieren mit Faser-Kunststoff-Verbunden*. Springer Verlag, 2007.

[101] S. Sheng. Report on Wind Turbine Subsystem Reliability - A survey of Various Databases. Technical report, NREL/PR-5000-59111, 2013.

[102] J. Shmueli, M. A. Eder, and A. Tesauro. A versatile stereo photogrammetry based technique for measuring fracture mode displacements in structures. *Precision Engineering*, 39:38–46, 2015.

[103] G. J. Short, F. J. Guild, and M. J. Pavier. The effect of delamination geometry on the compressive failure of composite laminates. *Composites Science and Technology*, 61(14):2075–2086, 2001.

[104] G. J. Short, F. J. Guild, and M. J. Pavier. Delaminations in flat and curved composite laminaites subjectedt to compressive load. *Composite Structures*, 58(14):249–258, 2002.

[105] D. Skibicki. *Phenomena and Computational Models of Non-Proportional Fatigue of Materials*. Springer, 2014.

[106] P. D. Soden, M. J. Hinton, and A. S. Kaddour. Lamina properties, lay-up configurations and loading conditions for a range of fibre reinforced composite laminates. *Failure Criteria in Fibre Reinforeced Polymer Composites: The World-Wide Failure Exercise - Elsevier*, pages 30–51, 2004.

[107] B. F. Sørensen. Materials and Structures for Wind Turbine Rotor Blades - an Overview. In *ICCM-17 - 17th International Conference on Composite Materials*, pages 1–10, Edinburgh, United Kingdom, July 2009. Materials Research Division, Risø National Laboratory for Sustainable Energy, Technical University of Denmark.

[108] B. F. Sørensen, K. Branner, H. Stang, H. M. Jensen, E. Lund, T. K. Jacobsen, and Halling K. M. Improved design of large wind turbine blades of fibre composites (phase 2) - summary report. *Roskilde - Denmark; Risø National Laboratory for sustainable Energy Risø-R-1526 (EN)*, 2005.

[109] B. F. Sørensen, S. Goutianos, and T. K. Jacobsen. Strength scaling of adhesive joints in polymer-matrix composites. *International Journal of Solids and Structures*, 46(3-4):741–761, 2009.

[110] B. F. Sørensen, K. Jørgensen, T. K. Jacobsen, and R. C. Østergaard. DCB-specimen loaded with uneven bending moments. *International Journal of Fracture*, 141:163–176, 2006.

[111] B.F. Sørensen. *Cohesive laws for assessment of materials failure: Theory, experimental methods and application*. DTU Wind Energy, 2010.

[112] Standard. IEC 61400-1: Wind Turbines - Part 1: Design Requirements. Technical report, IEC, 2005.

[113] Standard. IEC 61400-1: Wind turbines - part 1: Design requirements amend 1, 2005. Standard.

[114] Standard. DNV-DS-J102: Design and Manufacture of Wind Turbine Blades, Offshore and Onshore Wind Turbines. Technical report, Det Norske Veritas, 2010.

[115] Standard. IEC 61400-23: Wind turbines - Part 23: Full-scale structural testing rotor blades. Technical report, IEC, 2015.

[116] ASTM Standard. D3039M-08 (2008) Standard test method for tensile properties of polymer matrix composite materials. *Annual Book of ASTM Standards*, pages 1–13, 2013.

[117] H. S. Toft, K. Branner, P. Berring, and J.D. Sørensen. Defect distribution and reliability assessment of wind turbine blades. *Engineering Structures*, 33:171–180, 2011.

[118] N. Troldborg, C. Bak, H. A. Madsen, and W. Skrzypinski. The DAN-AERO MW Experiments: Final report. Tech. Rep. Risø-R-1726(EN). Technical report, Risø-DTU, Roskilde, Denmark, 2010.

[119] S. W. Tsai and E. M. Wu. A General Theory of Strength for Anisotropic Materials. *Journal of Composite Materials*, 5(1):58–80, 1971.

[120] A. Turon. *Simulation of delamination in composites under quasi-static and fatigue loading using cohesive zone models.* Universitat de Girona, 2007.

[121] A. Turon, C. G. Dávila, P. P. Camanho, and J. Costa. An Engineering Solution for using Coarse Meshes in the Simulation of Delamination With Cohesive Zone Models. *Nasa/Tm-2005-213547*, March:1–26, 2005.

[122] Wikipedia. Continuum mechanics - Wikipedia. https://en.wikipedia.org/wiki/Continuum_mechanics. Accessed: 2015-10-06.

[123] Wikipedia. Fracture toughness - Wikipedia. https://en.wikipedia.org/wiki/Fracture_toughness. Accessed: 2015-10-06.

[124] S. Wittrup. Dong og Siemens giver Horns Rev 2 storstilet vinge-makeover, 2015.

[125] J. Yang, J. Peng, J. Xiao, S. Xing, J. Jin, and H. Deng. Structural investigation of composite wind turbine blade considering structural collapse in full-scale static tests. *Composite Structures*, 97:15–29, 2013.

[126] D. Zenkert, M. Battley, Technical University of Denmark. Department of Mechanical Engineering, and DTU Mekanik. *Foundations of Fibre Composites: Notes for the Course: Composite Lightweight Structures.* DTU, 2006.

[127] W. Zhang and Y. Cai. *Continuum Damage Mechanics and Numerical Applications.* Zhejang University Press, 2014.